**This document is downloaded from DR-NTU (https://dr.ntu.edu.sg)
Nanyang Technological University, Singapore.**

Smart energy management system for microgrid planning and operation

Chen, Shuaixun

2012

Chen, S. (2012). Smart energy management system for microgrid planning and operation. Doctoral thesis, Nanyang Technological University, Singapore.

https://hdl.handle.net/10356/50788

https://doi.org/10.32657/10356/50788

Downloaded on 30 Apr 2025 11:46:06 SGT

NANYANG TECHNOLOGICAL UNIVERSITY

Smart Energy Management System for Microgrid Planning and Operation

by

Chen Shuaixun

A thesis submitted in partial fulfillment for the degree of Doctor of Philosophy

Supervised by Associate Professor Gooi Hoay Beng

Division of Power Engineering
School of Electrical and Electronic Engineering

October 2012

Declaration of Authorship

I, CHEN SHUAIXUN, declare that this thesis titled, 'Smart Energy Management System for Microgrid Planning and Operation' and the work presented in it are my own. I confirm that:

- This work was done wholly or mainly while in candidature for a research student qualification at this University.
- Where any part of this report has previously been submitted for any other qualification at this University or any other institution, this has been clearly stated.
- Where I have consulted the published work of others, this is always clearly attributed.
- Where I have quoted from the work of others, the source is always given. With the exception of such quotations, this report is entirely my own work.
- I have acknowledged all main sources of help.
- Where the report is based on work done by myself jointly with others, I have made clear exactly what was done by others and what I have contributed myself.

Signed: _____

Date: _____

"Live to learn and learn to live."

Abstract

A Smart grid refers to an electricity transmission and distribution system that incorporates elements of traditional and cutting-edge power engineering, information technology, and communications, which can provide better grid performance and to support a wide array of additional custom services to consumers. A smart grid would facilitate the full use of sustainable energy technologies like solar power, wind power and fuel cells with the help of distributed energy storage systems (ESS).

To understand the behavior of a smart grid, the author develops models suitable for overall analysis and design. The final goal is to lay the groundwork which would allow efficient management of the smart grid by solving all kinds of optimization problems, i.e., minimizing the operating costs, enhancing efficiency and reducing emission level while meeting the load demand. Smart Energy Management System (SEMS) is a core part for a smart grid system, which can make this system more intelligent. The optimal placement of the capacitors with the renewable energy is also discussed in this thesis.

To handle the multi-objective optimization in the smart grid, a Jump and Shift method is proposed in this thesis. It aims to solve a large scale linear/nonlinear programming problem where the constraints are related to another large scale linear/nonlinear programming. A 14-bus and 112-bus power systems are tested to verify the multi-objective optimization algorithm based on the Jump and Shift method.

ESS plays an important role in the smart grid. It is desirable to shave the peak demand and store the surplus electrical/renewable energy. A new method based on the cost-benefit analysis for the optimal sizing of an ESS in a microgrid (MG) is proposed. The Unit Commitment problem with the required spinning reserve capacity for the MG is considered in this method.

To deal with the optimal control of ESS, the author presents an online management energy system for the lithium-ion (Li-ion) battery based on the proposed mathematical battery model and the adaptive Extended Kalman Filter (EKF) method. The proposed technique can be used to predict the state of charge (SOC) of the Li-ion battery via the online measured voltage and current.

Acknowledgements

I feel extremely honored to conduct my PhD studies under the guidance of Associate Professor Gooi Hoay Beng. With his deepest insight into the problems, he has inspired and supported me in many different ways in my research work. I thank him for this opportunity.

I would like to thank the technical staff of the Laboratory for Clean Energy Research for the support and service rendered especially to Ms. Grace Ong and Mr. Thomas Foo for their technical support in the equipment usage and software installation. I would like to thank Mr. Wang Mingqiang, Mr. Cheah Peng Huat and Ms. Xia Nan for their valuable discussion and assistance throughout the simulation and analysis of my research studies. This research work is supported in part by the Agency for Science, Technology and Research (A*STAR) under the Microgrid Energy Management System project of Intelligent Energy Distribution Systems (IEDS).

A special thank goes to all my friends and members of the Clean Energy Research group. They have made the laboratory a wonderful, friendly and intellectual stimulating place. I also would like to acknowledge gratefully to Nanyang Technological University, Singapore for awarding me the Research Scholarship.

As always, I am grateful to my parents, little brother, and wife for their encouragements and unconditional support to my study. Their unwavering love is always my source of strength.

Finally I would like to thank all the people who have provided help and support throughout the conduct of my research project.

Contents

List of Figures

List of Tables

Abbreviations

AOTC	**A**nnualized **O**ne-time **E**SS **C**ost
AMPL	**A** **M**odeling **P**rogramming **L**anguage
BOEU	**B**enefit **O**f the **E**lectric **U**tility
BESS	**B**attery **E**nergy **S**torage **S**ystem
DG	**D**istributed **G**generation
DER	**D**istributed **E**nergy **R**esources
ESS	**E**nergy **S**torage **S**ystem
EKF	**E**xtended **K**alman **F**ilter
EPRI	**E**lectric **P**ower **R**esearch **I**nstitute
FACTS	**F**lexible **AC** **T**ransmission **S**ystem
FNN	**F**eed-forward **N**eural **N**etwork
FC	**F**uel **C**ell
GE	**G**eneral **E**lectric
GW	**G**igawatts
GENCO	**G**enerating **C**ompany
LP	**L**inear **P**rogramming
MAPE	**M**ean **A**bsolute **P**ercentage **E**rror
MT	**M**icroturbine
MB	**M**arket **B**enefit
MLIP	**M**ixed **L**inear **I**nteger **P**rogramming
MG	**M**icrogrid

NLP	**N**onlinear **P**rogramming
OCV	**O**pen **C**ircuit **V**oltage
OLTC	**O**n-Load **T**ap **C**hanger
OPF	**O**ptimal **P**ower **F**low
PV	**P**hotovoltaics
PCC	**P**oint of **C**ommon **C**oupling
RMSE	**R**oot **M**ean **S**quare **E**rror
SEMS	**S**mart **E**nergy **M**anagement **S**ystem
SOD	**S**tate **o**f **D**ischarge
SOC	**S**tate **o**f **C**harge
SMES	**S**uperconducting **M**agnetic **E**nergy **S**torage
SVC	**S**tatic **V**ar **C**ompensator
TCPD	**T**he **C**ost **P**er **D**ay
TCAC	**T**otal **C**ost of **A**ll **C**apacitor
TCPH	**T**he **C**ost **P**er **H**our
TCUL	**T**ap **C**hanging **U**nder **L**oad
TOU	**T**ime **O**f**U**se
TB	**T**otal **B**enefit
TC	**T**otal **C**ost
TUCC	**T**otal **UC C**ost
UC	**U**nit **C**ommitment
VHDL	**V**ery **H**igh Speed Integrated Circuit Hardware **D**escription **L**anguage
WEG	**W**ind **E**nergy **G**enerator
WT	**W**ind **T**urbine

Symbols

a	No-load cost of generator	$\$/h$
b	Cost coefficients	$\$/kW$
c	Cost coefficients	$\$/kW^2$
p_r	the rated electrical power	kW
v_c	the cut-in wind speed	m/s
v_r	the rated wind speed	m/s
v_f	the cut-out wind speed	m/s
I	Solar radiation	kW/m^2
t	Time index	
i	Bus index	
$C(t)$	Energy stored in the ESS at time t	kWh
$P_t^{E,c}$	Power charged by the grid to ESS	kW
Δt	Duration time of each interval	hr
$P_t^{E,d}$	Power discharged by ESS	kW
$P_t^{E,c}$	Power charged by the grid to ESS	kW
I_f	Current from the $from$ end to the to end	A
I_t	Current from the to end to the $from$ end	A
V_f	Voltage at the $from$ end	V
V_t	Voltage at the to end	V
QC_i	Size of capacitor	$MVar$
P_{Loss}^t	Minimum power grid loss	kW

CG	Set of conventional generator	
WG	Set of wind power generator	
PG	Set of solar power generator	
$P10$	Capacity of the 10-min quick start unit	kW
$G10$	Set of 10-min quick start up unit	
SR_t	Hourly required reserve capacity	kW
R_{tn}	Online spinning reserve	kW
r_n	Reserve cost	$\$/kW$
d_n	Start up cost	$\$/kW$
c_w	Wind energy cost	$\$/kWh$
c_{pv}	PV energy cost	$\$/kWh$
P_{tn}	Output power of a generator	kW
PD_{ti}	Power demand at the ith bus	kW
$R10_n$	10-min spinning reserve capacity	kW
R_{int}	Equivalent internal resistance	ohm
$E(t, T(t), i(t))$	General expression for potential	V
R_1	Internal resistance of Li-ion battery	V
R_2	Resistance due to change of ambient temperature	V
Q	Covariance parameters of processing noise	
R	Covariance parameters of observation error	
α	Factor of hourly online reserve to be maintained online	
η_d	Discharge efficiency	
η_c	Charge efficiency	
β_w	Cost coefficient of wind generator w	$\$/MWh$
β_s	Cost coefficient of PV s	$\$/MWh$
$\Re^n$	n dimensions space	

χ	Shift factor

Dedicated to my little girl

Chapter 1

Introduction

1.1 Introduction

The restructuring of the electricity supply industry all over the world has gradually introduced a competitive electricity market where generators sell their electricity and consumers buy their electricity. However active participation from demand side remains low. The electric power grid is demoded, fragile, and inefficient. A serious accident of a power system could cripple business districts for days or weeks, which will cause huge economic loss [1]. Reinforcing the grid with advanced computer controls would allow power to be distributed more efficiently, safely, and robustly and would help to distribute renewable energy.

With the rising standard of living, developing countries like China will push up the demand for energy of the world. A higher standard of living, especially a higher level of education is the main driver which will set new demands on the production of electricity. Since the OPEC embargo of 1973, the problem of oil dependence has been the most important energy challenge [2]. Furthermore, oil is priced worldwide, no matter where the oil comes from. Oil is like any other commodity - the last unit sold determines its price. Hence, the price of oil will be more expensive as the supply dwindles. The only answer is to reduce demand and diversify energy supply away from oil.

The potential benefits of a smarter power delivery system are substantial. An upgraded grid could boost the economy, reduce the impact of energy production and consumption

on the environment, and enhance the security of the network. The Electric Power Research Institute (EPRI) in the U.S. suggests that transformation of the power grid over the next 20 years could result in a substantial increase in productivity and a reduction in carbon emission [1].

A Smart grid refers to an electricity transmission and distribution system that incorporates elements of traditional and cutting-edge power engineering, information technology, and communications, which can provide better grid performance and to support a wide array of additional custom services to consumers [1]. A smart grid would facilitate the full use of sustainable energy technologies like solar power, wind power and fuel cells with the help of distributed energy storage systems (ESS).

A smart grid would be self healing and more secure from physical accidents. The electricity transmission and distribution system is a critical element of the infrastructure. Surging demand for high quality, and digital-grade electricity put a lot of stress on the electrical infrastructure. In the U.S., EPRI estimates that power outages and power quality disturbances cost businesses at least $50 billion per year [1]. There is a paramount need to upgrade the grid. The new technology in the areas of transmission monitoring systems, information systems, and power flow controls would enable the grid to be self healing by permitting grid controllers to anticipate and instantly respond to system problems in order to avoid or mitigate power outages, power quality problems, and system contingencies. This would benefit high-tech consumers and others who require a stable and reliable power supply.

A smart grid would facilitate the use of new energy technologies like solar power, wind power and fuel cells. Distributed energy resources, fuel cells, microturbines, and renewable generation, are new choices for homes, offices and factories. However, the grid does not accommodate them easily and the price for the distributed resources is much higher presently for certain technologies. Enabling such use of distributed generation and how to improve the reliability and power quality of the intermittent renewable energy will be the major issues that need to be resolved.

A smart grid would give consumers greater control of their electricity use in their homes and businesses by rearranging their home work schedule following the real time electricity price. Effective interfaces between the grid and the energy management systems of buildings and other loads will also enable residential, commercial, and

industrial consumers to manage electricity use in a manner that improves efficiency and reduces consumer costs. A smart grid would increase efficiency and reduce energy costs with the use of the intelligent energy management system. It can reschedule power transmission through the power grid and by optimizing power flows will reduce waste and maximize the use of the lowest-cost generation resources.

By optimizing the use of sustainable and varied energy sources as part of the smart grid [3], the smart grid may be able to make a significant contribution towards a reliable power supply system. For instance, in a sunny day, the photovoltaic (PV) array may provide more power. In a windy day the wind turbine will generate more power. If the day is neither sunny nor windy or if more power is needed, the fuel cell, micro-turbine or main conventional supply can be used. The key is to orchestrate the power sources in an optimal manner. The inclusion of batteries in a smart grid system allows excess power produced to be stored, or alternatively, the excess power could be put into good use in the smart grid [4], [5], [6], [7]. In this way it is expected that the smart grid could reduce pollution and deliver reliable energy in a variety of weather and load situations.

1.2 Sustainable Resources

Sustainable energy is the provision of energy that meets the needs of the present without compromising the ability of future generation to meet its needs. Sustainable energy sources include all renewable energy sources, such as hydroelectricity, solar energy, wind energy, fuel cell, and tidal power. It usually also includes technologies designed to improve energy efficiency.

Energy efficiency and renewable energy are said to be the twin pillars of sustainable energy. Sustainable energy has been defined as the provision of energy such that it meets the needs of the future without compromising the ability of future generation to meet its own needs. Sustainable Energy has two key components: renewable energy and energy efficiency [8]. Any energy generation, efficiency and conservation source where resources are available to enable massive scaling, becomes a significant portion of energy generation for the long term, preferably 100 years [9]. The energy used is replenishable within a human lifetime and causes no long-term damage to the environment [10].

This sets sustainable energy apart from other renewable energy terminology such as alternative energy and green energy, by focusing on the ability of an energy source to continue providing energy. Sustainable energy can produce some pollution of the environment, as long as it is not sufficient to prohibit heavy use of the source for an indefinite amount of time. Sustainable energy is also distinct from low-carbon energy, which is sustainable only in the sense that it does not add to the CO_2 in the atmosphere.

1.2.1 Solar Energy

The Earth receives 174 petawatts (PW) of incoming solar radiation (insolation) at the upper atmosphere [11]. Approximately 30% is reflected back to space while the rest is absorbed by clouds, oceans and land masses. The spectrum of solar light at the Earth's surface is mostly spread across the visible and near-infrared ranges with a small part in the near-ultraviolet.

The Earth's land surface, oceans and atmosphere absorb solar radiation, and this raises their temperature. Warm air containing evaporated water from the oceans rises, causing atmospheric circulation or convection. When the air reaches a high altitude, where the temperature is low, water vapor condenses into clouds, which rain onto the Earth's surface, completing the water cycle. Sunlight absorbed by the oceans and land masses keeps the surface at an average temperature of $14°C$ [12]. By photosynthesis green plants convert solar energy into chemical energy, which produces food, wood and the biomass from which fossil fuels are derived [13].

The total solar energy absorbed by the Earth's atmosphere, oceans and land masses is approximately 3,850,000 exajoules (EJ) per year [11]. In 2002, this was more energy in one hour than the world used in one year [14]. The amount of solar energy reaching the surface of the planet is so vast that in one year it is about twice as much as what will ever be obtained from all of the Earth's non-renewable resources of coal, oil, natural gas, and mined uranium combined [15]. Solar energy can be harnessed in different levels around the world. Depending on a geographical location the closer to the equator the more "potential" solar energy is available [16].

1.2.2 Wind Energy

Wind power is the conversion of wind energy into a useful form of energy, such as using wind turbines to make electricity, windmills for mechanical power, windpumps for water pumping or drainage, or sails to propel ships. The total amount of economically extractable power available from the wind is considerably more than the present power use from all sources by human [17]. Wind power, as an alternative to fossil fuels, is plentiful, renewable, widely distributed, clean, and produces no greenhouse gas emissions during operation. Its cost per unit of energy produced is similar to the cost for new coal and natural gas installations [18].

Wind power has been used as long as humans have put sails into the wind. For more than two millennia wind-powered machines have ground grain and pumped water. Wind power was widely available and not confined to the banks of fast-flowing streams, or later, as a source of energy. Wind-powered pumps drained the polders of the Netherlands, and in arid regions such as the American mid-west or the Australian outback, wind pumps provided water for live stock and steam engines.

With the development of electric power, wind power found new applications in lighting buildings remote from centrally-generated power. Throughout the 20th century distributed small wind plants suitable for farms or residences, and larger utility-scale wind generators that could be connected to electricity grids for remote use of power were developed. Today wind powered generators operate in every size which ranges between tiny plants for battery charging at isolated residences, and up to near-gigawatt sized offshore wind farms that provide electricity to national electrical networks.

At the end of 2010, worldwide nameplate capacity of wind-powered generators was 197 gigawatts (GW) [19]. Wind power now has the capacity to generate 430 TWh annually, which is about 2.5% of worldwide electricity usage [20]. Over the past five years the average annual growth in new installations has been 27.6 percent. Wind power market penetration is expected to reach 3.35 percent by 2013 and 8 percent by 2018 [21]. Several countries have already achieved relatively high levels of wind power penetration, such as 21% of stationary electricity production in Denmark, 18% in Portugal, 16% in Spain, 14% in Ireland and 9% in Germany in 2010 [19, 22]. As of 2011, 83 countries around the world are using wind power on a commercial basis.

1.2.3 Fuel Cells

The principle of the fuel cell was discovered by German scientist Christian Friedrich Schonbein in 1838 [23]. Based on this work, the first fuel cell was demonstrated by the Welsh scientist and barrister Sir William Robert Grove in the February 1839 edition of the Philosophical Magazine and Journal of Science [24] and was later sketched, in 1842, in the same journal [25]. The fuel cell he made used similar materials in today's fuel cell.

A fuel fell is an electrochemical device similar to a battery, but differs from the latter in that it is designed for continuous replenishment of the reactants consumed, i.e. it produces electricity from an external fuel supply. It is more of an energy conversion system than an energy storage system. A block diagram is shown in Figure 1.1 [26]. Typical reactants used in a fuel cell are hydrogen on the anode side and oxygen on the cathode side. The fuel that is used in the fuel cells can either be renewable (alcohol or methane from waste digestion or hydrogen from wind or solar conversion of water) or non-renewable (hydrogen or methane from oil and gas production or alcohol from industrial processes) [27]. Hydrogen is the most common fuel, but hydrocarbons such as natural gas and alcohols like methanol are sometimes used. Fuel cells are different from batteries in that they require a constant source of fuel and oxygen to run, but they can produce electricity continually for as long as these inputs are supplied. In contrast, conventional batteries consume solid reactants and once these reactants are depleted, they must be discarded or recharged with electricity by running the chemical reaction backwards, or, at least in theory, have their electrodes replaced. Typically in fuel cells, reactants flow in whereas reaction products flow out, and continuous long-term operation is virtually feasible as long as these flows are maintained. Fuel cells are attractive in some applications because of their high efficiency and low level of pollution.

Welsh Physicist William Grove developed the first crude fuel cells in 1839. The first commercial use of fuel cells was in NASA space programs to generate power for probes, satellites and space capsules. Since then, fuel cells have been used in many other applications. Fuel cells are used for primary and backup power for commercial, industrial and residential buildings and in remote or inaccessible areas. They are used to power fuel cell vehicles, including automobiles, buses, forklifts, airplanes, boats, motorcycles and submarines.

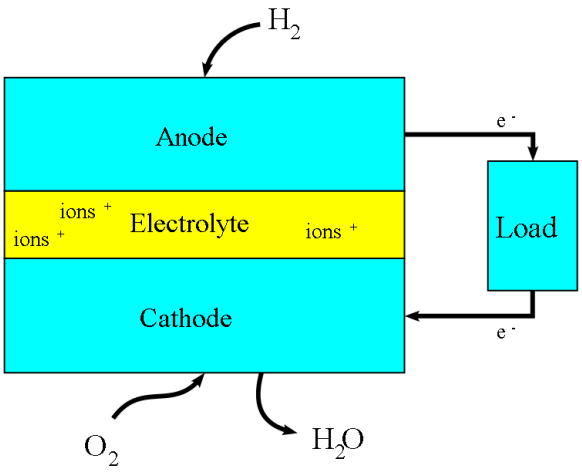

FIGURE 1.1: A block diagram of a fuel cell

There are many types of fuel cells, but they all consist of an anode, a cathode and an electrolyte that allows charges to move between the two sides of the fuel cell. Electrons are drawn from the anode to the cathode through an external circuit, producing direct current electricity. As the main difference among fuel cell types is the electrolyte, fuel cells are classified by the type of electrolyte they use. Fuel cells come in a variety of sizes. Individual fuel cells produce very small amounts of electricity, about 0.7 volt, so the cells are "stacked", or placed in series or parallel circuits, to increase the voltage and current output to meet the power generation requirements [27]. In addition to electricity, fuel cells produce water, heat and, depending on the fuel source, very small amounts of nitrogen dioxide and other emissions. The energy efficiency of a fuel cell is generally between 40-60%, or up to 85% efficient if waste heat is captured for use.

1.3 Energy Storage Systems

Energy storage systems are becoming more and more important for the power system integrated with sizable renewable energy sources. It can help balance the renewable power due to their intermittency and unpredictability. Several energy storage approaches are studied intensely in recent years. These include electrochemical batteries, super-capacitors, compressed air energy storage, superconducting magnetic energy storage and flywheel energy storage [28].

Supercapacitors or ultracapacitors offer a unique combination of high power and high energy, compared to conventional capacitors that have enormous power but store only a tiny amount of energy. Supercapacitors are capable of very fast charges and discharges, and are able to go through a large number of cycles without degradation [29]. When a supercapacitor is charged, there is no chemical reaction. Instead, the energy is stored as a charge or concentration of electrons on the surface of a material. The energy can be released in a microsecond, much faster than the energy from a chemical reaction. The schematic diagram of a supercapacitor is shown in Figure 1.2.

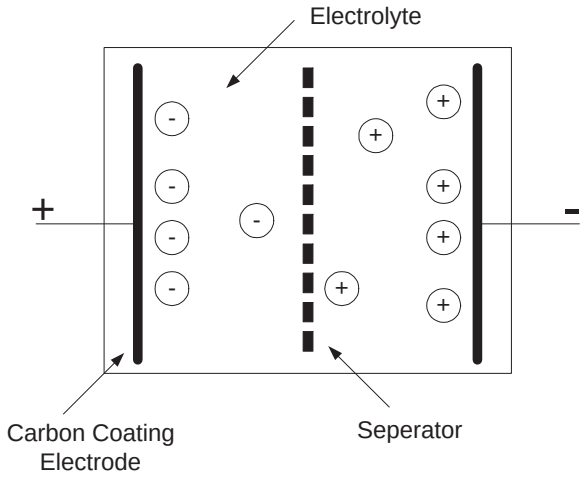

FIGURE 1.2: Structure of a supercapacitor

A supercapacitor can be viewed as two non-reactive porous plates, or electrodes, immersed in an electrolyte, with a voltage potential applied across the collectors. In an individual supercapacitor cell, the applied potential on the positive electrode attracts the negative ions in the electrolyte, while the potential on the negative electrode attracts the positive ions. A porous dielectric separator between the two electrodes prevents the charge from moving between the two electrodes. The plates hold opposite charges which generates an electric field. Supercapacitors store energy via electrostatic charges on opposite surfaces of the electric double layer, which is formed between each of the electrodes and the electrolyte ions. Because supercapacitors move electrical charges between solid-state materials rather than through a chemical reaction, they can be cycled tens of thousands of times, more rapidly, and are not affected by deep discharges

of chemical batteries. Discharge times range from fractions of seconds to tens of seconds and in some cases several minutes.

Superconducting magnetic energy storage (SMES) systems store energy in the field of a large magnetic coil with direct current flowing inside. The direct current can be converted back to AC electric current as needed. The basic structure of SMES system is shown in Figure 1.3. Low temperature SMES cooled by liquid helium is commercially available [30]. When cooled to cryogenic temperatures, superconducting wires exhibit zero resistance, which means that a current circulating in such a coil can persist for a very long time without any loss. High temperature SMES cooled by liquid nitrogen is still in the development stage and may become a viable commercial energy storage system in the future [31].

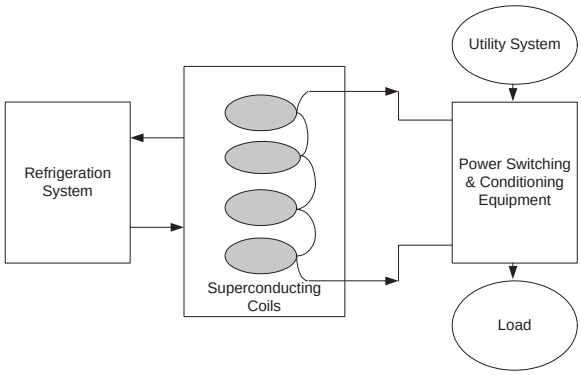

FIGURE 1.3: Basic structure of SMES system

An electrochemical battery is a device that stores potential energy through the chemical reaction of its components. The reaction creates free electrons that, when connected to a circuit, will move through the circuit and drive a load. This reaction will continue until the chemical reactants are depleted [32]. A cell has five major components as shown in Figure 1.4. The negative electrode supplies electrons to the external load during discharge.

The electrodes in a battery must be made of different materials or the cell will not be able to develop an electrical potential and thus will not conduct electrical current. The electrolyte completes the internal circuit in the battery by supplying ions to the positive and negative electrodes. The separator is used to electrically isolate the negative and positive electrodes which only allow ion transfer between the electrolyte and electrodes.

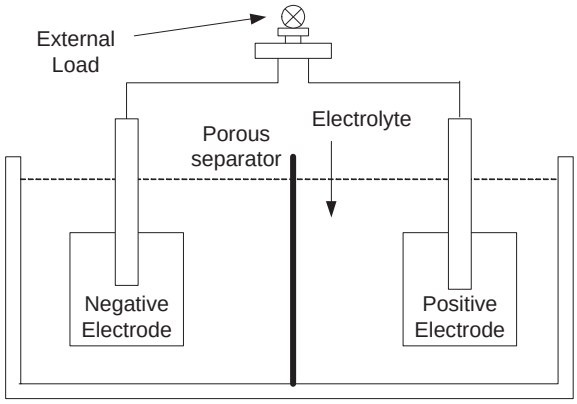

FIGURE 1.4: Operating principle of an electrochemical battery

Lithium-ion batteries, sometimes abbreviated Li-ion batteries, are a type of rechargeable battery in which a lithium ion moves between the anode and cathode. The lithium ion moves from the anode to the cathode during discharge and from the cathode to the anode when charging.

Lithium ion batteries are commonly used in consumer electronics. They are currently one of the most popular types of battery for portable electronics, with one of the best energy-to-weight ratios, no memory effect, and a slow loss of charge when not in use. Certain kinds of mistreatment may cause Li-ion batteries to explode. In addition to uses for consumer electronics, lithium-ion batteries are growing in popularity for defense, automotive, and aerospace applications due to their high energy density [33].

The three primary functional components of a lithium ion battery are the anode, cathode, and electrolyte, for which a variety of materials may be used. Commercially, the most popular material for the anode is graphite, although materials such as TiS2 were originally used. However, the cathode is generally one of three materials, a layered oxide, such as cobalt oxide, a polyanion, such as lithium iron phosphate, and a spinel, such as manganese oxide. Depending on the choice of material for the anode, cathode, and electrolyte, the voltage, capacity, life, and safety of a lithium-ion battery can change dramatically. Lithium-ion batteries are not to be confused with lithium batteries, the key difference being that lithium batteries have a metallic lithium anode and lithium ion batteries have an anode material into which lithium inserts.

In this thesis, a model is coded according to the resistive companion method. It allows systematic handling of nonlinearities in the model equations and easy connection to

other objects in a system-level simulation and provides sufficient accuracy to capture the major electrical and thermal properties of the battery.

1.4 Optimization

In a smart grid, most planning and operating problems can be considered as the optimization problems. They consist of maximizing or minimizing the objective function by systematically choosing input values within an allowed set and computing the value of the function. The generalization of optimization theory and techniques to other formulations comprises a large area of applied mathematics. More generally, optimization includes finding best available values of some objective function given a defined domain. The problem may consist of a variety of different types of objective functions and different types of domains. Normally, linear programming and nonlinear programming can be used to deal with these optimization problems.

Linear programming itself was first developed by Leonid Kantorovich, a Russian mathematician, in 1939 [34]. The method was kept secret until 1947 when George B. Dantzig published the simplex method and John von Neumann developed the theory of duality as a linear optimization solution, and applied it in the field of game theory. Later, many industries found its use in their daily planning. Linear programming (LP) or linear optimization is a mathematical method for determining the best outcome, such as maximum profit or lowest cost in a given mathematical model for some requirements represented as linear relationships. Linear programming is a specific case of mathematical programming or mathematical optimization.

More formally, linear programming is a technique for the optimization of a linear objective function, subject to linear equality and linear inequality constraints. Its feasible region is a convex polyhedron, which is a set defined as the intersection of finitely many half spaces, each of which is defined by a linear inequality. Its objective function is a real-valued affine function defined on this polyhedron. A linear programming algorithm finds a point in the polyhedron where this function has the smallest or largest value if such a point exists.

In mathematics, nonlinear programming (NLP) is the process of solving a system of equalities and inequalities, collectively termed constraints, over a set of unknown real

variables, along with an objective function to be maximized or minimized, where some of the constraints or the objective function are nonlinear.

In the power system planning and operation, most of the problems can be formulated as (1.1) where $\mathbf{x} \in \Re^n$ is a vector of decision variables, including the control and nonfunctional dependent variables. $c : \Re^n \rightarrow \Re$ is a scalar function that represents the cost function's optimization goal. $g : \Re^n \rightarrow \Re^m$ is a vector function with equality constraints. $\mathbf{h} : \Re^n \rightarrow \Re^p$ is a vector of nonlinear functional bounds and simple bound variables, with a lower bound $\underline{\mathbf{h}}$ and a upper bound $\overline{\mathbf{h}}$. $\mathbf{p} \in \Re^m$ is a vector of decision variables, and it depends on problem B.

$$\begin{aligned} &Min/Max && c(\mathbf{x}) \\ &s.t. && g(\mathbf{x}) + \mathbf{p} = 0 \\ & && \underline{\mathbf{h}} \leq h(\mathbf{x}) \leq \overline{\mathbf{h}} \end{aligned} \tag{1.1}$$

The traditional problems of a power system like unit commitment, economic dispatch and optimal power flow can all be represented by (1.1) under different objective functions and constraints.

1.5 Motivation

Currently much research works are being undertaken in the area of microgirds (MGs), a kind of smarter distributed power system with renewable energy and energy storage. Inside a smarter grid, there could be many MGs. The common issue of smart grid and MG is that they both need to face the renewable energy integration problem. Compared with smart grid, the structure of MG is much simple and easier for testing the research methods. Hence some proposed methods are first tested in MG and then be tested in smart grid.

Some model architectures of MG have been proposed in the literature [35], [36], [37], [38], [39]. Although components of the MGs are fairly well understood, the system as a whole is not. When several sources are connected to form a MG, the system behavior is unpredictable. In order to develop an appropriate management system, system modeling

and planning form the heart of MG research. Several research groups around the world are investigating the feasibility and benefits that the MGs may provide [36].

The MG concept assumes a cluster of loads and microsources operating as a single controllable system that provides both power and heat to its local community [40]. A MG is an integrated energy system consisting of interconnected loads and distributed energy resources (DERs) which include renewable (clean) energy resources such as solar cells, fuel cells, wind turbines and hydro turbines, as shown in Figure 1.5 [41]. In addition, a MG must be capable of assessing its health in real-time, predicting its behavior, adapting to new environments, handling distributed resources, stochastic demand, and providing optimal response to smart devices.

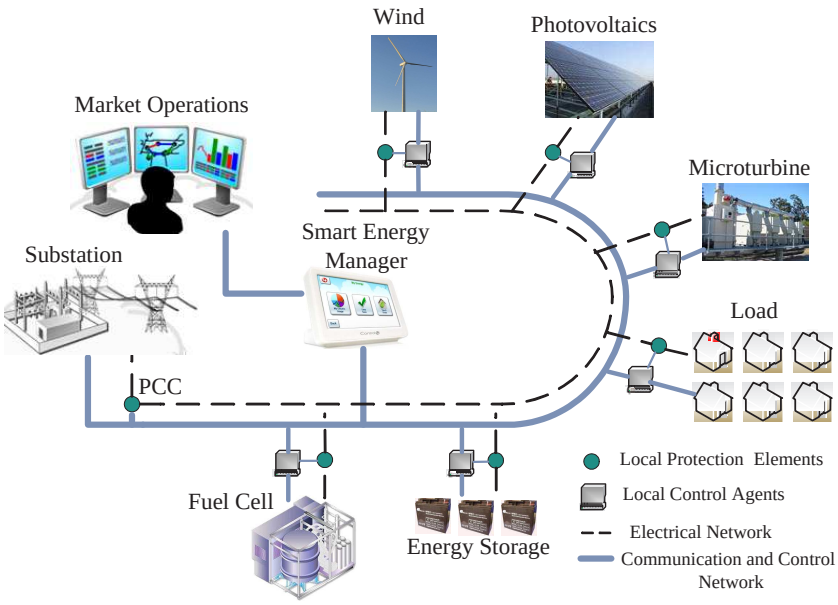

FIGURE 1.5: A simple architecture of microgrid

This concept provides a new paradigm for defining the operation of distributed generation. A MG can be built either at a customer facility or location that includes parts of the local distribution system. It will improve service reliability of supply and provide better power quality [42]. Some model architectures and control strategies have been proposed in the literature. Reference [35] proposed a system approach which considers power generators and associated loads as a MG. The MG in the Kythnos island and the MG energy management framework of General Electric (GE) have been introduced in [36]. Figure 1.6 shows a real 125-kW MG in Laboratory for Clean Energy

Research, Nanyang Technological University, Singapore. It is part of the A⋆STAR Intelligent Energy Distribution System (IEDS) project initiatives in Singapore. The online management and control strategies for MGs have been addressed in [37], [38] and [39]. Some problems encountered include issues dealing with the unbalanced loads and harmonics associated with the system, i.e. under-voltage and over-voltage, phase shift, frequency and power quality problems [43].

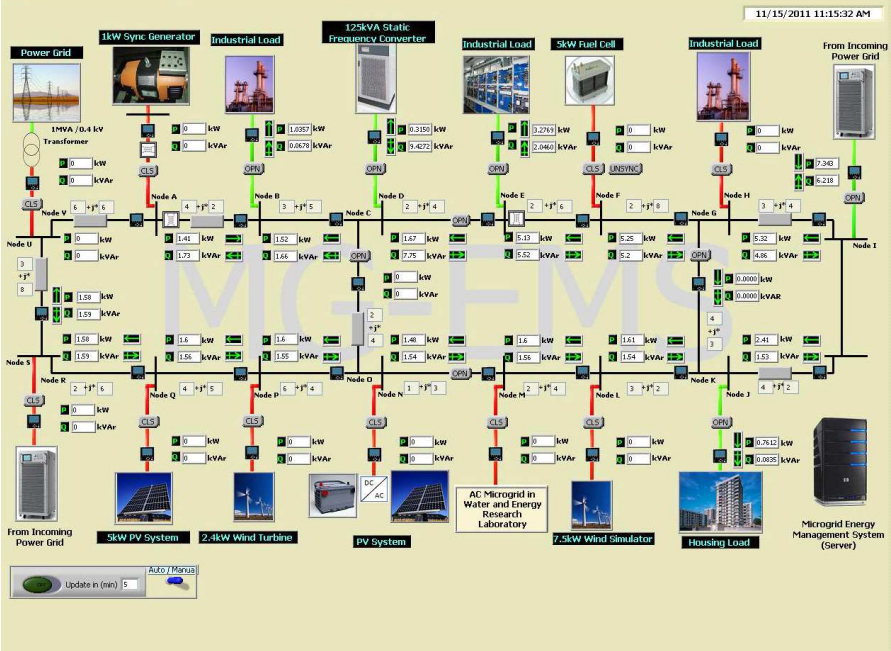

FIGURE 1.6: Microgrid in Laboratory for Clean Energy Research

MG technologies are playing an increasingly important role in the customer's energy portfolio. They can be used to meet base load power, peaking power, backup power, remote power, power quality, and cooling and heating needs. Customers usually own small-scale, on-site power generators which may be owned and operated by a third party. If the distributed generator does not provide 100% of energy needs to customers at all times, it can be used in conjunction with a distributed energy storage device or a connection with the local grid for backup power. The MG resources can support and strengthen the centralized model of electricity generation, transmission, and distribution.

The conventional arrangement of a modern large power system offers a number of advantages [44]. Large generating units can be operated efficiently with only a relatively small number of personnel. The existing interconnected high voltage transmission

network equipped with a sophisticated energy management system allows the generator reserve requirement to be minimized, the most efficient generating plant to be dispatched at any time, and bulk power to be transported long distances with limited electrical losses. The distribution network can be designed for unidirectional flows of power and can be sized to accommodate customer loads only. However, over the last few years a number of influences have led to the increased interest in MGs [35], [40]. Among them are:

1. Reduction in gaseous emissions (mainly CO_2) – With the renewable energy integrated in MG, the power consumption can depend less on traditional generators. It will help reduce the coal and oil consumption, which can reduce the gaseous emissions.

2. Energy efficiency or rational use of energy – With the setup of the MG, the power generation is close to the load center. It means that the power generated can be consumed locally. It will help reduce the transmission loss compared with the power transmitted over a long distance.

3. Enhanced supply reliability – Traditional interconnection rules require generators to trip in the event of any disturbance, while one of the key objectives of MG development is to achieve systems that can island and ride through grid problems.

4. Diversification of energy sources – Compared with the traditional power system, a MG can be integrated with more renewable energy sources.

5. National and global power requirements – With depleted oil and gas resources, renewable energy needs to be considered in the future. It is an added advantage for the introduction of MGs.

Modeling is an important component for the energy management system. A precise model helps the electric utility make wise unit commitment decisions to reduce operating costs and carbon emission appropriately. Besides playing a key role in meeting the load demand, it is also essential to maintain the reliability of the MG. The central controller uses the modeling results as a basis of off-line network analysis to determine if the system might be costly and have high emissions. If so, corrective actions should be prepared, such as power purchases and bringing other units on line. This thesis focuses on the

modeling of MGs and discusses new management approaches for reducing the operating costs and carbon emissions.

Interior point method is chosen for the research work in this thesis. It is also referred to as a barrier method and belongs to a certain class of algorithms which solve linear and nonlinear convex optimization problems. Since the first publication [45] in 1984, interior point methods have evolved both theoretically and computationally as a well-known field nowadays. The primal-dual interior point method is used in this report. The fundamental ideas of primal-dual methods were developed between 1987 and 1991. The major causes of this burst of activities were the explicit definition of the primal-dual central path and the insight into its properties provided by a number of authors [46].

This thesis also proposed a new method called the Jump and Shift method. It aims to solve the large scale linear/nonlinear programming problem where the constraints are related to another large scale linear/nonlinear programming problem. The shift factor χ is used to make this convergence method very fast. It is very helpful when applied to solve a multi-objective optimization problem. The details of the proposed method are described in Chapter 5.

1.6 Organization of Thesis

This thesis consists of eight chapters. Chapter 1 is the introduction of the thesis. The concept of a smart grid is introduced and the motivation of the research is discussed. Sustainable energy and energy storage systems are introduced. The optimization method for a smart grid is also discussed.

In Chapter 2, the models of the power system are introduced. The quadratic function is used to represent the cost of traditional generators and the linear function is used to represent the cost of microturbines and fuel cells. The time-series model is introduced and used to forecast the wind speed. A piecewise linear function is used to calculate the wind power. A feed-forward neural network is introduced and used to forecast the solar radiation. A maximum power point tracker is assumed to be used when the PV power is calculated from solar radiation. An energy storage system and a transmission/distribution line model are also introduced.

In Chapter 3, an optimal capacitor planning method based on optimal power flow is proposed for a power system with wind generators and photovoltaics (PV) arrays. The system is formulated as a mixed nonlinear integer problem. This method minimizes not only the total system cost, but also the system losses. The capacitor cost function, which considers the lifetime of capacitors and interest rate for financing the installed capacitors, is also developed in this chapter.

In Chapter 4, a real-time dynamic scheduling algorithm for energy storage in a PV/battery system based on the battery charge and discharge characteristics, and current and temperature dependence of the capacity of the battery is presented. The work aims to extend existing battery-aware scheduling techniques. It takes into consideration many aspects of battery characteristics. This allows better use of the battery bank and can prolong the battery service time. This Chapter also builds a simple PV/battery system in the SIMPLORER within Very High Speed Integrated Circuit Hardware Description Language (VHDL) for real-time simulation.

In Chapter 5, Smart energy management system (SEMS) is introduced and a new technique called the Jump and Shift method is developed to handle the multi-objective optimization in SEMS. A case study is shown to verify the multi-objective optimization algorithm based on the Jump and Shift method. The results show that the proposed technique performs very well to solve the multi-objective optimization in SEMS for smart grids.

In Chapter 6, a new method based on the cost-benefit analysis for optimal sizing of an energy storage system in a MG is presented. The unit commitment problem with spinning reserve for MG is considered in this method. Two mathematical models have been built for both the islanded and grid-connected modes of MGs. The main problem is formulated as a mixed linear integer problem (MLIP). The effectiveness of the approach is validated by case studies where the system rating for optimal energy storage of the islanded and grid-connected MGs are determined. Quantitative results show that the optimal size of BESS exists and differs for both the grid-connected and islanded MGs in this chapter.

In Chapter 7, an online energy management system for Li-ion batteries is proposed to predict the state of charge (SOC) of the Li-ion battery via the online measured voltage and current. The mathematical battery model of Li-ion battery is proposed. The

adaptive EKF algorithm is employed and the SOC is considered as the state variable for the charging or discharging process of the Li-ion battery. The effectiveness and robustness of the online energy management system is validated. Experimental results show the estimated SOC is accurate for various operating conditions.

Chapter 8 concludes of the research studies for the smart grid and the suggestions to future works are also presented.

Chapter 2

System Modeling

In the development of the electricity supply industry, it becomes increasingly important for a power system to respond faster to load variation and to introduce intelligent control to handle the integration of renewable energy. Microgrids and smart grids are new concept of power systems which are designed to address variability in both demand and supply. Some important aspects for MGs are renewable energy, ESS, smart meters and communication devices. To understand the MG's behavior, each component is modelled individually in this chapter. The components modelled include traditional generators, microturbine and fuel cell, wind power, solar power, battery storage system, and transmission/distribution lines. Each component is first modelled and studied individually, and then they are combined to form a complete model of a MG. The models described will be used in the other chapters for developing optimal online management techniques based on the MG modelled.

2.1 Traditional Generators

Traditional synchronous generators have been used for many years. They supplied most of the electrical power and played an important role in the early power system. They are still very important for power generation. Synchronous generators have several kinds of supply curves, e.g. linear or quadratic functions. Normally, a generator offer file comprises the incremental offer curve and the start-up cost curve. Many electric utilities

prefer to represent their generator offer price as a single-segment or a multiple-segment linear cost function. With faster computing speed, a quadratic cost function is more frequently adopted. It is used in this thesis. The offer price for each generator can be represented by a quadratic cost function, while the start-up and no-load costs are spread over the running period. The generator offer price is taken as the sum of the operation cost of the generating set at no-load and the cost for producing the output of the generating set. The formulation is given as follows:

$$C(P) = a_1 + b_1 P + c_1 P^2 \tag{2.1}$$

where a is the no-load cost. Figure 2.1 shows the quadratic offered cost function $C(P)$.

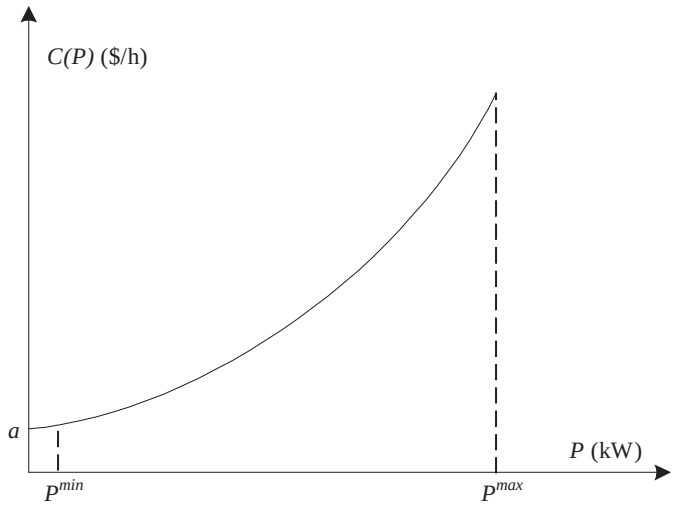

FIGURE 2.1: Generator offered cost as a function of output power

2.2 Microturbines and Fuel Cells

Microturbines (MTs) are small single-staged combustion turbines ranging from a few kWs to serval MWs, although their size varies. MTs are usually powered by natural gas, but can also be powered by biogas, hydrogen, propane or diesel. The operation principle of the MTs follows the same principles of conventional gas turbines depending on Brayton cycle [47]. The electrical energy, passing through the transformer, is delivered to the distribution system and the local load. The transformer boosts the converter output voltage up to the voltage level of the distribution system.

Considering the installation cost and the fuel cost, the total cost function of MTs can be obtained in (2.2) [48] where a_2 and b_2 are the cost coefficients.

$$C(P) = a_2 + b_2 P \tag{2.2}$$

Fuel cells generate power through the electrochemical reaction between hydrogen and oxygen. The conversion is highly efficient and leaves only water and heat as by-products. This is the main motivation for the increasing interest in the technology [49]. The operations of the fuel cells are based on the fundamental electrochemical principles [49]. The reaction of hydrogen gas (H_2) and oxygen gas (O_2) forms water (H_2O). The reaction process is presented in (2.3).

$$2H_2 + O_2 \Rightarrow 2H_2O \tag{2.3}$$

Fuel cells have an electrolyte between two electrodes. The process occurs naturally and is caused by the fact that the charged particles migrate towards regions of lower electro-chemical energy. Fuel cells are on the cutting edge of future technologies and have the potential to reshape our energy future. Fuel Cells offer lower emission and higher efficiency than diesel engines but are likely to be too expensive for many applications. They use an electrochemical process to turn hydrogen and oxygen into pollution-free electricity and heat. The total cost of fuel cells can also be presented in equation (2.2) with different cost coefficients.

2.3 Wind Power

Wind power is electrical power generated by wind turbines, which are installed in locations with strong and sustained winds. The wind pushes against the fan blades of a wind turbine, mounted on a tower at an elevation high above and away from ground obstructions and obstacles and where wind currents are strong and consistent. Wind turbines have no control over their energy output and are constrained by their physical limits in their operation and applications.

The availability of the power supply generated from wind energy depends on the availability of the wind. Thus, wind speed forecasting plays a key role in wind power

prediction of an electrical energy system. Consequently, extensive research has been directed toward the development of good and reliable wind power forecasts in recent years and many different forecasting approaches have been developed [50], [51], [52]. The time-series model in [50] yields reasonable good results in wind speed forecast studies. References [53], [54] introduced the artificial intelligence (AI) models for wind speed forecast. They include artificial neural networks (ANNs), mixture-of-experts (ME), nearest-neighbor search (NNS), and a combined particle swarm optimization (PSO) and support vector machines (SVMs). Compared with other wind speed forecast methods, the time-series model is much easier to be implemented and can also achieve good accuracy. Hence, the time-series model is chosen for the wind speed forecast study in this thesis.

2.3.1 Time-Series Models

Generally a time-series model of wind speed can be established in (2.4)

$$y_t = f(W_t, \mu_t, \sigma_t, \mu, \sigma, \ldots) \tag{2.4}$$

where W_t is the observed wind speed at hour t; μ_t and σ_t are the mean observed wind speed and the standard deviation of the observed wind speed at hour t respectively; μ and σ are the mean observed wind speed and the standard deviation of the observed wind speed obtained from all the measurements respectively.

The data series set y_t can be used to build the following Auto-Regressive and Moving Average ARMA(n,m) time-series model,

$$y_t = \phi_1 y_{t-1} + \phi_2 y_{t-2} + \cdots + \phi_n y_{t-n} + \alpha_t - \theta_1 \alpha_{t-1} - \theta_2 \alpha_{t-3} - \cdots - \theta_m \alpha_{t-m} \tag{2.5}$$

where $\phi_i (i = 1, 2, \ldots, n)$ and $\theta_i (i = 1, 2, \ldots, n)$ are the auto-regressive and moving average parameters of the model respectively. $\{\alpha_t\}$ is a normal white noise process with a zero mean and a variance of σ_a^2.

A pure AR(n) model can be treated as a special form of ARMA(n,m) by setting $m = 0$. Once the time series model of the wind speed is established, the simulated wind speed

SW_t can be calculated as follows,

$$SW_t = f^{-1}(y_t, \mu_t, \sigma_t, \mu, \sigma, \ldots) \tag{2.6}$$

where $f^{-1}(\cdot)$ is the inverse function of $f(\cdot)$.

The linear least square approach can be used to estimate the parameters ϕ_i and σ_a^2 when $m = 0$; whereas the non-linear least square approach should be adopted to estimate the values of ϕ_i, θ_i and σ_a^2 when $m \neq 0$. The basic steps used in the least square approch include estimating the initial values and searching for the optimal values based on the initial guesses.

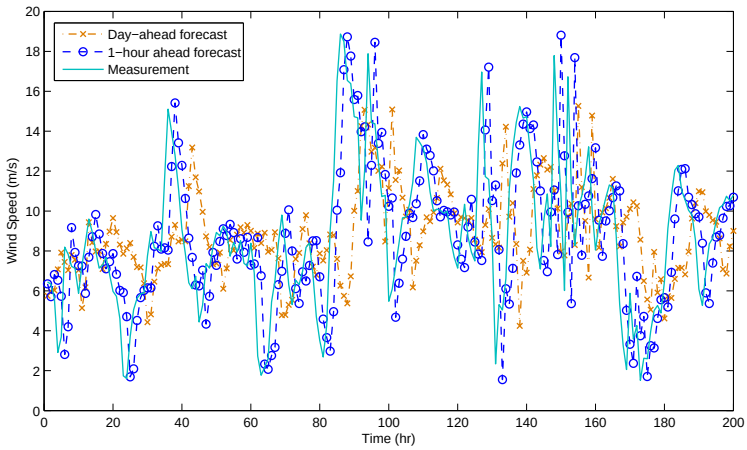

FIGURE 2.2: Measured and forecasted wind speed using time series model

Figure 2.2 shows the time-series results of the 1-hour ahead and day ahead forecast for the wind speed and its wind speed measurements over 200 hours. The high forecast accuracy will be obtained using historical data. One year of wind speed data is used. Figure 2.2 also shows that the accuracy of the 1-hour ahead forecast is better than that of the day ahead forecast using the time-series model.

2.3.2 Wind Power Output

The wind power generation output can be considered as a function of wind velocity [55]. A typical wind power output characteristic curve is shown in Figure 2.3, which is based on the data from a manufacturer of wind turbines.

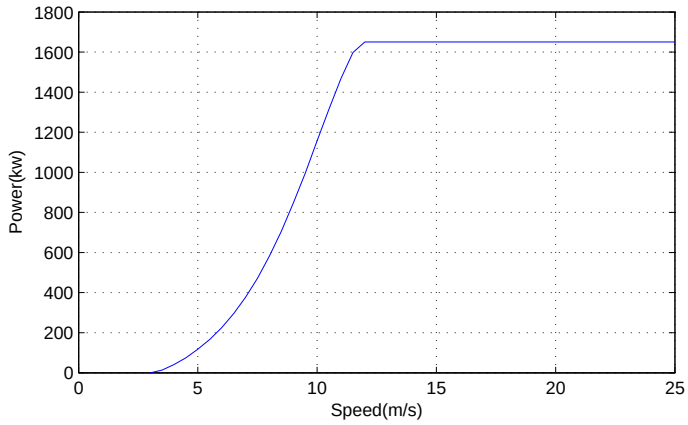

FIGURE 2.3: Power generated by wind turbine at different wind speeds

A piecewise function can be simply used to fit the relationship between output power and wind speed (v), which is shown in Figure 2.3 [56]. The formulation in (2.7) is used. A plot of P_w versus v based on (2.7) is shown in Figure 2.4 [55], [57].

$$P_w = \begin{cases} 0 & v \leq v_c \\ p_r * \frac{v - v_c}{v_r - v_c} & v_c \leq v \leq v_r \\ p_r & v_r \leq v \leq v_f \\ 0 & v \geq v_f \end{cases} \tag{2.7}$$

where:

p_r is the rated electrical power.

v_c is the cut-in wind speed.

v_r is the rated wind speed.

v_f is the cut-out wind speed.

In Figure 2.4, the cut-in wind speed, v_c, is the minimum speed to start the wind turbine and the cut-out wind speed, v_f, is the maximum speed to shutdown the wind turbine. Some error exists between the calculated wind power and the real wind power due to the error in the forecasted wind speed. It is expressed as a root mean square error ($RMSE$) for the time-series model and has been addressed in many research papers [53], [58].

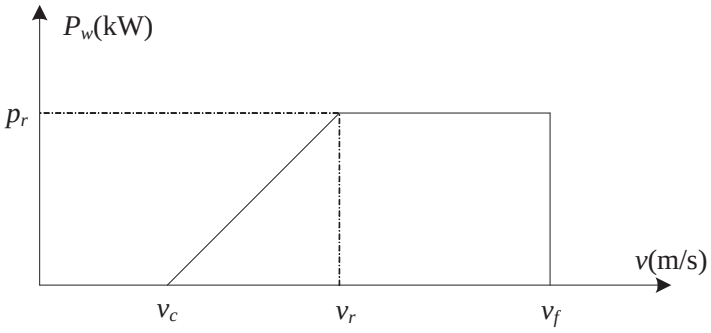

FIGURE 2.4: Power wind speed characteristic

2.4 Solar Photovoltaic Power

PV is an attractive source of renewable energy for distributed urban power generation due to their relatively small size and noiseless operation. Their applications are expected to significantly increase all over the world. Solar photovoltaic power is a generic term used for electrical power that is generated from sunlight. A solar photovoltaic system converts sunlight into electricity. The fundamental building block of solar photovoltaic power is the solar cell or photovoltaic cell [59], [60]. A solar cell is a self-contained electricity-producing device constructed of semi-conducting materials. Light strikes on the semi-conducting material in the solar cell, creating direct current (DC) [61].

Figure 2.5 shows the voltage and current characteristic curves of a photovoltaic (PV) cell. The current will decrease when the voltage increases, which means the power generated by PV is not a constant. It is very easy to find the maximum power point with the help of a power curve in Figure 2.5. When the PV works at the maximum power point, the energy transfer efficiency from sunlight to electrical power is at its maximum [60].

The equivalent circuit of a PV module used is shown in Figure 2.6. In the calculation of the power output of a PV module, we assume that a maximum power point tracker will be used. Manufacturers of PV modules supply information on the voltage and current of the maximum power point at reference temperature and reference irradiance. The output current I can be expressed as a function of the output voltage V from the equivalent circuit of the PV module.

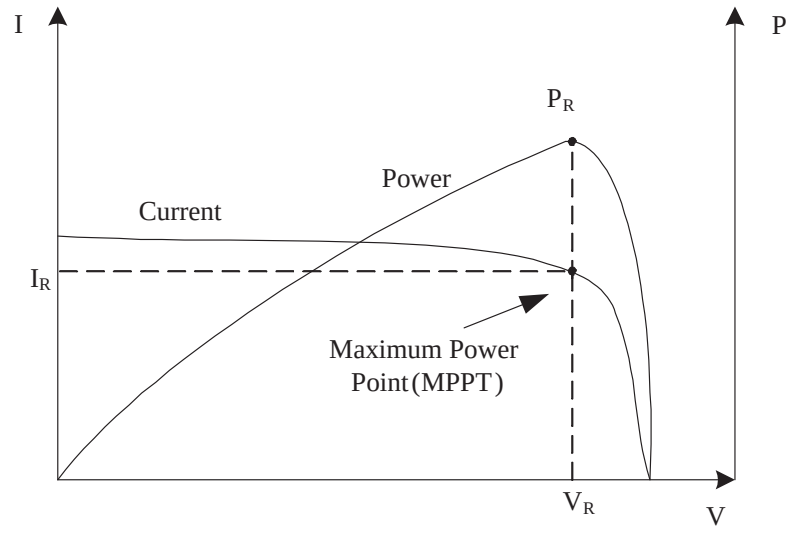

FIGURE 2.5: V-I characteristic curve and maximum power point of PV

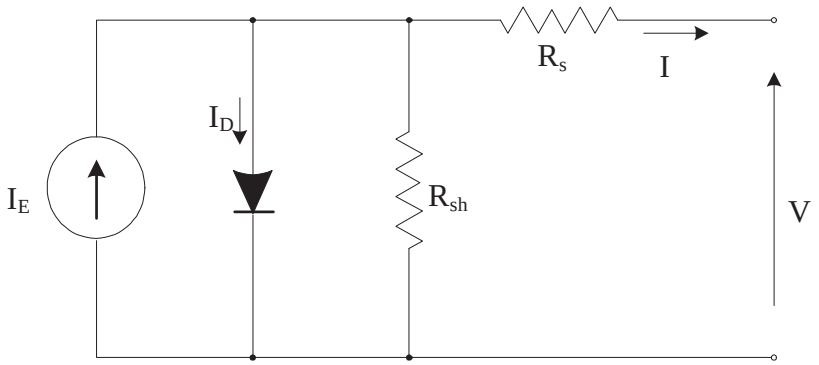

FIGURE 2.6: Equivalent circuit of a PV module

Normally, the power output curve at every hour is used for the power system optimization. The forecasting data of PV power output based on the maximum power point tracker is used for implementation of the PV module.

In the PV system, we assume that a maximum power point tracker will be used. The maximum power output is presented by (2.8) [62], [63].

$$p_s = \eta SI(1 - 0.005(t_o - 25)) \tag{2.8}$$

where η is the conversion efficiency of the solar cell array (%); S is the array area (m^2); I is the solar radiation (kW/m^2); and t_o is the outside air temperature ($^\circ C$).

A feed-forward neural network (FNN) is the most popular and most widely used models in many practical applications [64]. It is used to forecast the solar radiation based on the past one month solar radiation and weather data. It is formed by a large number of highly interconnected processing elements through a learning process [65]. FNN is able to learn the complex relationships between the inputs and the specific targeted output after training.

A basic neural network consists of three layers. They are the input layer, hidden layer and output layer. In a multi-layer FNN, neurons are organized in a distinct layered topology as shown in Figure 2.7. A FNN only allows data flow in a forward direction, i.e., the data flows from the input layer neurons, through the hidden layer neurons, and finally reaching the output layer neurons.

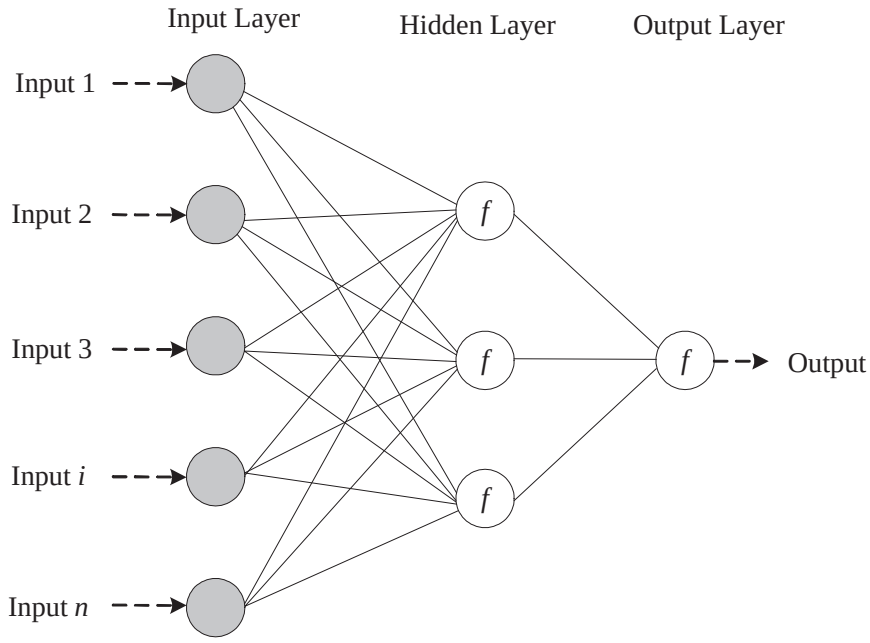

FIGURE 2.7: A simple three-layer feed-forward neural network

The widely used learning method in FNN is the backpropagation algorithm. Backpropagation is a form of supervised learning in which the network is provided with

examples of inputs and the target output. The training starts with random weights and the objective is to adjust them to make sure that the error is minimal. The values of the hidden layer neurons can be expressed in (2.9).

$$h_j = f_1(\sum_{i=1}^{n} v_{ij}x_i + \theta_j) \tag{2.9}$$

where h_j is the value of the hidden layer neuron; $f_1(\cdot)$ is a tangent sigmoid transfer function; x_i is the value of the input layer neuron; v_{ij} is the adjustable weight between the input and hidden layers and θ_j is the bias of the hidden layer neuron.

The hidden layer will be considered as the input to the output layer and the value of the output layer neurons is shown in (2.10)

$$o_j = f_2(\sum_{i=1}^{n} w_{ij}h_i + \gamma_j) \tag{2.10}$$

where o_j is the value of the hidden layer neuron; $f_2(\cdot)$ is a linear transfer function; w_{ij} is the adjustable weight between the hidden and ouput layers and γ_j is the bias of the output layer neuron.

FNN is used to forecast the solar radiation based on the past one month solar radiation and weather data. Besides, the forecasted weather data on the study day also needs to be obtained from National Environment Agency (NEA). The original data is included in the input layer. The output layer is the solar radiation on the study day [66]. Figure 2.8 shows the actual and forecasted solar radiation of one day using FNN.

Mean Absolute Percentage Error ($MAPE$) is used to express the difference between the actual and forecasted radiation. $MAPE$ can be calculated by (2.11) [67].

$$MAPE = \frac{100}{N}\sum_{i=1}^{N}\left|\frac{I_f^i - I_a^i}{I_a^i}\right|\% \tag{2.11}$$

I_f and I_a are the forecasted and actual radiation respectively. N is the data size.

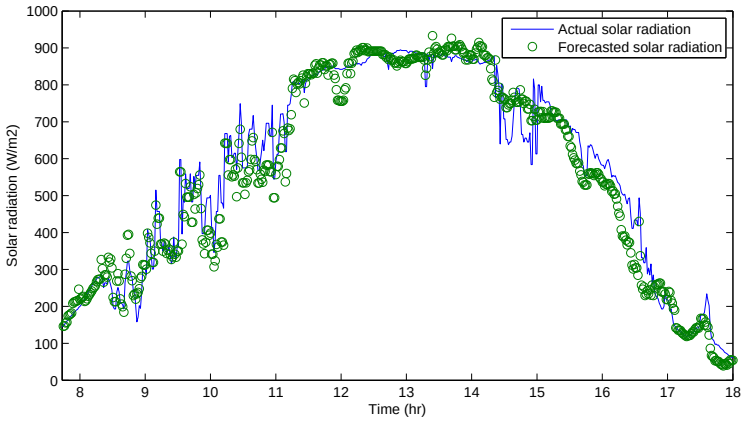

FIGURE 2.8: Actual and forecasted solar radiation using FNN

2.5 Energy Storage Systems

In recent years, several forms of energy storage were studied intensely. These include electrochemical batteries, super-capacitors, compressed air energy storage, super-conducting magnetic energy storage and flywheel energy storage. Lithium ion (Li-ion) batteries are chosen in this study.

The charge and discharge equations are shown in (2.12). $P_t^{E,d}$ is the power discharged by the battery bank during the time period t. $P_t^{E,c}$ is the power of the battery bank charged by the grid, i.e. the battery bank is being charged up. $C(t)$ is the energy stored in the battery bank at time t. Δt is the duration time of each interval. η_d and η_c are the discharge efficiency and charging efficiency respectively. The battery bank should also satisfy the constraints from (2.13) to (2.15).

$$\begin{aligned} Discharge &: C(t+1) = C(t) - \Delta t P_t^{E,d}/\eta_d \\ Charge &: C(t+1) = C(t) + \Delta t P_t^{E,c}\eta_c \end{aligned} \tag{2.12}$$

subject to the following battery constraints:

Power limits:

$$\begin{aligned} 0 \leq P_t^{E,d} \leq P_E^{d,max} \\ 0 \leq P_t^{E,c} \leq P_E^{c,max} \end{aligned} \tag{2.13}$$

Stored energy limits:

$$C_{min} \leq C(t) \leq C_{max} \tag{2.14}$$

Starting and ending limits:

$$C(0) = C(T) = C_S \tag{2.15}$$

where $P_E^{d,max}$ is the maximum discharge rate; $P_E^{c,max}$ is the maximum charge rate; C_{min} and C_{max} are the minimum and maximum energy stored in the battery bank; $C(0)$ is the initial energy inside the battery bank and C_S is the initial stored energy limit of the battery bank. For the energy balance of the energy storage system, the stored energy inside the battery bank $C(T)$ is set the same as the initial stored energy.

The cost of ESS includes the one-time ESS cost and the annual maintenance cost. The battery energy storage system (BESS) is made up of small battery blocks. This means that the one-time ESS cost, FC in \$/kWh, which includes the cost of batteries purchased and their installation is a variable cost proportional to the size of BESS. The maintenance cost per year is also a variable cost proportional to the size of BESS. If BESS's life time is l years and the maintenance cost is MC(\$/kWh) per year, then the total cost of BESS is $CE(FC + l * MC)$ (\$). CE is the size of BESS.

The cost of generation is calculated in 24 hours, which is one day. Hence we need to normalize the total cost of BESS in $\$/day$. If the interest rate r for financing the installed BESS is considered, the annualized one-time ESS cost ($AOTC$) in \$/year for BESS is shown in (2.16).

$$AOTC = \frac{r(1+r)^l}{(1+r)^l - 1} FC * CE \tag{2.16}$$

The total cost of BESS can be obtained by adding $AOTC$ and the maintenance cost together. Then the cost per day ($TCPD$) of BESS installed in \$/day can be found in (2.17).

$$TCPD = \frac{1}{365}(AOTC + CE * MC) \tag{2.17}$$

2.6 Transmission/Distribution Line Model

Line models are used to calculate power loss. Fixed loads are modeled as constant real and reactive power consumption at each bus, P_d and Q_d, are specified in the bus injection matrix. The shunt admittance of any constant impedance shunt elements at a bus is specified by G_{sh}andB_{sh}. Hence, the shunt elements Y_{sh} of the bus admittance matrix is as follows:

$$Y_{sh} = G_{sh} + jB_{sh} \tag{2.18}$$

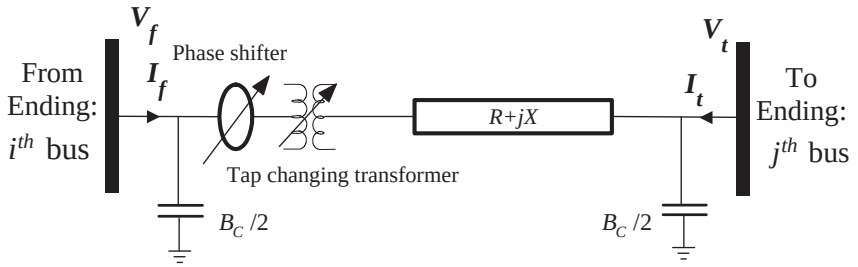

FIGURE 2.9: A simple transmission/distribution line model in a power system

Each branch, which could be a transmission line, transformer or phase shifter, is modeled as a standard π model, with a resistance R and a reactance X in series with an ideal transformer with a tap ratio τ and a phase shifter with an angle θ_{shift}. The total line charging capacitance B_c is split into two halves which form two shunt elements of the π-model. The model is shown in Figure 2.9 [68]. Branch voltages and currents from the $from$ end to the to end of the branch are related by the branch admittance matrix Y_{br} as follows:

$$\begin{bmatrix} I_f^l \\ I_t^l \end{bmatrix} = Y_{br} \begin{bmatrix} V_f^l \\ V_t^l \end{bmatrix} \tag{2.19}$$

where $Y_{br} = \begin{bmatrix} (Y_s \frac{1}{\tau^2} + j\frac{B_c}{2}) & -Y_s \frac{1}{\tau e^{-j\theta_{shift}}} \\ -Y_s \frac{1}{\tau e^{j\theta_{shift}}} & Y_s + j\frac{B_c}{2} \end{bmatrix}$ and $Y_s = \frac{1}{R+jX}$.

Chapter 3

Reactive Power Planning of Power System with Renewable Energy

Reactive power is very important for power system operation. Reactive power flows can give rise to substantial voltage changes across the system, which means that it is necessary to maintain reactive power balances between sources of generation and points of demand. A power system could achieve a better power transmission efficiency by lowering the transmission loss through optimal reactive power flow. This chapter will address planning issues specifically the reactive power of power system with renewable energy. The issues of optimal power flow with more renewable energy and energy storage will be discussed in chapter 5.

3.1 Introduction

Reactive power planning of power systems provides the strategy of reactive power compensation so that the real power loss can be reduced and the system voltage profile and power factor can be improved [69]. The static var compensator (SVC) which uses the power electronic controller technique for adaptive reactive power compensation, has been applied in the industrial power system to compensate for large changes in reactive

power demand, but it is still not cost-justifiable in distribution systems. On the other hand, capacitor banks have been verified to have satisfactory cost benefits and are widely used for passive reactive power compensation in distribution systems and it is chosen in the case study.

Up to now, many capacitor planning methodologies have been proposed by homogeneous reactive power load distribution and uniform conductor size along the feeder [70, 71, 72]. The early analytical methods for capacitor placement are mainly developed by Neagle and Samson [73]. The problem is to determine the location and size of a given number of capacitors for minimizing the system loss at a given load level. These analytical methods are also integrated with some heuristics to obtain computer oriented solution methodologies and thus to overcome some of their shortcomings. Cook [74] extended the formulation of the problem to include peak power and energy loss reduction and proposed such a solution method to determine the number as well as the location and the size of capacitors. Grainger et. al. have researched extensively on this topic and employed methods such as normalized feeder/load techniques [75, 76, 77, 78, 79, 80, 81, 82, 83, 84]. Dynamic programming has been employed by Duran [85]. Baran and Wu [86] developed a complete formulation by including an objective function to minimize the costs and to model the system through a set of equations and regular limiting constraints. They decomposed the problem into two parts of optimal placement and optimal sizing. This helps in disassociating the integer part of the problem corresponding to optimal placement from the continuous part of optimal sizing. The problem of starting from an infeasible solution is seldom addressed. It is usually overcome by placing capacitors in the power system using heuristic knowledge possessed by the planner. Further, most of these methods do not consider renewable energy and thus are not comprehensive in their solutions. In addition, they also do not consider the economic dispatch in their optimal problem.

The basic idea in this chapter is to consider renewable energy, wind generators and PV arrays, based on the general capacitor planning problem. We use ac power flows to model high R/X ratios and consider both voltage constraints and line constraints in our problem. In the proposed method, the objective function is to minimize not only the cost of new capacitors, but also the cost of generating companies (GENCOs) as well as to minimize the penalty of real power loss in a power system.

3.2 Problem Formulation

3.2.1 Cost of Capacitors

The cost incurred in locating new capacitors includes one-time cost and maintenance cost. The one-time cost is divided into fixed costs and variable costs proportional to the size of capacitors. Hence the one-time cost of installing a capacitor at the i^{th} bus of QC_i $(MVAr)$ amount would be: $\gamma_i * (FC_i + QC_i * VC_i)$ where FC_i (\$) is a fixed cost; VC_i $(\$/MVAr)$ is a variable cost; and γ_i is a binary variable that assumes a value of one if the capacitor is located at i^{th} bus and zero otherwise. The maintenance cost per year is also a variable cost proportional to the size of capacitors. If the capacitor's life time is n years and the maintenance cost is $MC_i(\$)$ per year, then the total cost of the capacitor at the i^{th} bus is $\gamma_i * (FC_i + QC_i * VC_i + n * MC_i)$ (\$). Hence, the total cost of all capacitors $(TCAC)$ located in the system is

$$\begin{aligned} TCAC(QC_i, \gamma_i) = \sum_{i=1}^{N} \gamma_i * (FC_i \\ + QC_i * VC_i + n * MC_i) \end{aligned} \tag{3.1}$$

$TCAC$ in (3.1) shows the total payment for all the capacitors in n years. However, the cost of generators is calculated using the cost of power generators per hour. Hence we need to normalize the $TCAC$ in $\$/MW$ or $\$/hr$. It is not easy to forecast the total demand very accurately among these n years. Here we choose to normalize $TCAC$ in each hour.

If the interest rate r for financing the installed capacitors is considered, the annualized one-time cost $(AOTC)$ for the capacitor located at the i^{th} bus is shown in (3.2).

$$AOTC_i = \frac{r(1+r)^n}{(1+r)^n - 1} * \gamma_i * (FC_i + QC_i * VC_i) \tag{3.2}$$

The total cost of the capacitor can be obtained by adding $AOTC$ and the maintenance cost together. Then the cost per hour $(TCPH)$ of the capacitor installed at the i^{th} bus can be found in (3.3).

$$TCPH_i = \frac{1}{8760} * (AOTC_i + \gamma_i * MC_i) \tag{3.3}$$

3.2.2 Cost of Renewable Energy

Wind generators can be modeled using two methods based on their construction. Some wind energy generators (WEGs) are constructed using induction generators without a maximum power tracking scheme. Such WEGs can be modeled as a constant impedance for a given wind speed using the IEEE model and considering an appropriate reactive power compensation.

In this case, the WEG would deliver a constant real power output. An appropriate reactive power compensation to ensure unity power factor is assumed. The WEG is treated as a constant negative power load. For a given WEG, using a generic conversion formula for translating the wind speed data to power output [87], one may get output power as (2.7) in chapter 2.

The total cost of wind energy only includes construction cost and maintenance cost. We can simplify the cost of wind power generator as $CP_w = \beta_w * P_w$, where β_w is the cost coefficients of wind generator w and P_w is the power output of wind generator w.

The PV array generates electric power by using solar cells packaged in photovoltaic modules which convert energy from sunlight into electricity. The cost function of PV arrays can be used in the similar format as that of the WEG, which is $CP_s = \beta_s * P_s$, where β_s is the cost coefficients of the PV array s, and P_s is the power output of the PV array s.

3.2.3 Objective of Cost Minimization

The main purpose here is to obtain the maximum benefit for the electric utility. If we consider the demand, price of electricity, cost of generators and capacitors and also loss penalty, the benefit of the electric utility ($BOEU$) can be shown in (3.4), where ρ is the electricity price, P_m is the active power generated by fossil fuel generator m, and P_D, P_{Loss} and $C(P_m, P_w, P_s, QC_i)$ are demand, loss and cost of generators and capacitors

respectively. The third part $\rho * P_{Loss}$ is considered as the penalty of loss in $BOEU$, which means the GENCO pays the cost of line losses in the power system.

$$BOEU = \rho * P_D - C(P_m, P_w, P_s, QC_i) - \rho * P_{Loss} \tag{3.4}$$

Generally, the demand and electricity prices are decided by the power market, GENCOs and customers. We discuss the optimal problem at a given load level and the electricity price does not change very much in a short time interval, 1 hour in our case. Hence it can be considered as a known constant value. After that the question is to find the minimum value of the second and third parts in $BOEU$, which is shown in (3.5).

$$Min: \ C(P_m, P_w, P_s, QC_i) + \rho * P_{Loss} \tag{3.5}$$

where

$$\begin{aligned} &C(P_m, P_w, P_s, QC_i) = \textstyle\sum_{m=1}^{M} CF_m \\ &+ \textstyle\sum_{w=1}^{W} CF_w + \sum_{s=1}^{S} CW_s + \sum_{i=1}^{N} TCPH_i \end{aligned} \tag{3.6}$$

$$P_{Loss} = \sum_{l=1}^{L} |real(V_f^l * I_f^{l*} - V_t^l * I_t^{l*})| \tag{3.7}$$

subject to:

$$P_m - P_d^m - P_{br}^m = 0, \quad m = 1, \cdots, M \tag{3.8}$$

$$P_w - P_d^w - P_{br}^w = 0, \quad w = 1, \cdots, W \tag{3.9}$$

$$P_s - P_d^s - P_{br}^s = 0, \quad s = 1, \cdots, S \tag{3.10}$$

$$P_{br}^k + P_d^k = 0, \quad k = 1, \cdots, K \tag{3.11}$$

$$Q_i + QC_i - Q_d^i - Q_{br}^i = 0, \quad i = 1, \cdots, N \tag{3.12}$$

$$P_m^{min} \leq P_m \leq P_m^{max}, \quad m = 1, \cdots, M \tag{3.13}$$

$$P_w^{max} \leq P_w \leq P_w^{max}, \quad w = 1, \cdots, W \tag{3.14}$$

$$P_s^{max} \leq P_s \leq P_s^{max}, \quad s = 1, \cdots, S \tag{3.15}$$

$$Q_i^{max} \leq Q_i \leq Q_i^{max}, \quad i = 1, \cdots, N \tag{3.16}$$

$$0 \leq S_l \leq S_l^{max}, \quad l = 1, \cdots, L \tag{3.17}$$

where, CF_m, CF_w and CF_s represent the cost of fossil fuel generator m, wind generator w and PV array s respectively. P_d^m, P_d^w, P_d^s and P_d^k represent the active demand at the node of fossil fuel power generator m, wind generator w, PV array s and load k respectively. P_{br}^m, P_{br}^w, P_{br}^s and P_{br}^k represent the active power transferred to all the other buses connected at the node of fossil fuel power generator m, wind generator w, PV array s and load k respectively. They can be easily obtained from the power flow equations. Q_i and QC_i are the injected reactive power by the generator and capacitor at system bus i respectively. Q_i will be zero if there is no generator at bus i and so is QC_i if there is no capacitor at bus i. Q_{br}^i represents the reactive power at bus i transferred to all the other buses. This can be easily obtained from the power flow equations.

The objective function in (3.5) consists of two terms. The first term is the cost of power generators, wind generators and capacitors, which can be found in (3.6). The second term is the loss penalty in the system and is shown in (3.7). The active and reactive power flow equations are given in (3.8)-(3.12). Equations (3.13)-(3.15) are limits of the active output capability of fossil fuel, wind generators and PV arrays. Considering the cost of renewable energy (wind and PV)and their pollution-free property, the wind and PV arrays work at its maximum output point at some wind speed and solar radiation. The generator reactive power and power line MVA constraints are given in (3.16)-(3.17).

The optimal problem is a mixed-integer nonlinear programming problem that can be solved using KNITRO, a mixed-integer nonlinear solver, of A Modeling Language for Mathematical Programming (AMPL). Table 3.1 provides the dimension of this problem, which is expressed as the number of binary variables, real variables and constraints.

TABLE 3.1: Computational size of program

Number of binary variables	N
Number of real variables	5N+2L
Number of constraints	2(N+W+M+S)+K+L

3.3 Case Study

In this section, numerical simulations are conducted to illustrate how the proposed capacitors planning method works. An IEEE 14-bus test system is used. In this study,

one wind generator and one PV array are added to the system. Table 3.2 provides the generator data, which includes the minimum and maximum power and parameters of their cost function. The coefficient β is for the wind generator and PV array and the coefficients a, b, c are only for fossil fuel generators. As we mentioned before, the output of the wind generator and PV array are operated at their maximum output point under some condition.

TABLE 3.2: Generator data

Unit	Type	Location	Max (MW)	Min (MW)	Cost coefficients			
					a	b	c	β
1	Fossil fuel generator	Bus 1	300	75	167.1297	10.3103	0.0053	-
2	Fossil fuel generator	Bus 2	50	-	27.4597	17.1775	0.5957	-
3	Wind generator	Bus 3	30	0	-	-	-	30
4	PV	Bus 4	10	0	-	-	-	150

The fixed cost FC and the variable cost coefficient VC for capacitors are set at 100 (\$) and 1000 ($\$/MVAr$) respectively in this case. We also assume that they last for three years before a replacement is made. Normally it is 3-5 years.

The problem of capacitors planning based on the optimal benefit of GENCOs is formulated as a mixed integer nonlinear problem and solved using KNITRO of AMPL [88]. The optimal results are shown in Table 3.3.

TABLE 3.3: Optimal results

Bus	Voltage(pu)	$\theta(^\circ)$	γ	$QC(MVAr)$
1	1.0100	0.00	0	
2	0.9861	-5.12	0	
3	0.9600	-12.19	1	25.63
4	0.9622	-10.21	0	
5	0.9693	-9.19	0	
6	1.0900	-16.50	1	22.07
7	1.0681	-19.76	0	
8	1.0681	-19.76	0	
9	1.0738	-19.53	0	
10	1.0734	-19.37	1	5.93
11	1.0796	-18.13	1	2.33
12	1.0820	-17.63	1	1.84
13	1.0779	-17.95	1	6.57
14	1.0655	-19.98	1	5.34

TABLE 3.4: Output of generators

Unit	Type	Location	Output (MW)
1	Fossil fuel generator	Bus 1	221.29
2	Fossil fuel generator	Bus 2	22.00
3	Wind generator	Bus 3	20.00
4	PV	Bus 4	8.00

The optimal results in Table 3.3 show where the location (bus #) and $MVAr$ ratings of the installed capacitors. For this test system, the total installed capacity is 69.68 $MVAr$. The minimum value in (3.5) turns out to be \$5384.65. The loss penalty in 1 hour under this system is \$122.9 and the cost of generators and capacitors is \$5261.75. Table 3.4 shows the MW dispatch of all generators in the system.

3.4 Conclusion

This chapter develops an economic optimization method for capacitor planning in the power system. The proposed technique is tested on the IEEE 14-bus test system. It is formulated as a nonlinear mixed integer programming problem. The method considers fossil fuel generators, wind generators and PV arrays together. The cost function of the capacitor is designed to include the one-time cost, maintenance cost, capacitor's life time and interest rate for financing the installed capacitors. Hence, they make this optimal capacitor planning method more realistic. The loss penalty is also considered in this chapter, and ensures that GENCOs could get minimum loss penalty as well as obtain the minimum generation cost via the optimization.

Chapter 4

Scheduling of Energy Storage in a Grid-Connected PV/Battery System

4.1 Introduction

It has become increasingly important and necessary to deal with numerous challenges that affect global energy, economics, environment, and security. These challenges have in part resulted from population growth, electric utility restructuring, production of fossil fuel and its delivery and usage in various parts of the world, environmental pollution, and global warming. These driving forces underline the need and the opportunity for enhancing the structure for generating, transmitting, and delivering reliable and affordable energy [89].

It is envisioned that a portfolio of distributed generation (DG) technologies could provide a sizeable fraction of the electricity generation requirements and, in concert with other generation sources, could supply reliable energy in a constrained energy infrastructure. DG systems generally consist of the following: small and modular generating systems such as microturbines, reciprocating engines, fuel cell systems, cogeneration of heating and electricity generation, and hybrid units. They use a diversity of fuels, such as natural

gas and hydrogen and renewable energy resources such as PV, solar, wind, geothermal, biomass, tidal, and hydropower.

In this chapter, we focus on the grid-connected PV systems with battery storage because of the popularity of this type of system. With further developments in the PV technology and lower manufacturing costs, it is envisaged that the PV power will account for a higher percentage of electric power generation in the near future. PV possesses superior characteristics as a pollution free and abundant alternate source of energy with little running costs [90] [7]. However, the maximum power output of PV generally occurs when solar radiation is the strongest, which may not be consistent with the period of system peak load. To solve the problem of two distinct peak periods of a typical system load profile, batteries are installed to store energy from PV and grid during off-peak periods and to discharge during evening peak hours [91].

The grid-connected PV system is an electrical power generating system that uses a PV array as the primary source of electricity generation and is intended to operate synchronously and in parallel with the ac utility grid. Such a system may include battery storage and other generating sources for supplying on-site loads during grid outages and peak load hours. Figure 4.1 shows a simple PV/battery system.

There are many grid-connected PV/battery charging and discharging schemes in current studies. Some are considering economic power dispatch only based on the macrostructure of the distribution system. However, in practice the safety reasons should be considered first for battery operation. In addition, the useful life of the battery, generally less than 5 years, is much shorter than that of the PV arrays. A well designed battery-based charging/discharging scheme can prolong the battery's life and save time and money for preservation of the grid-connected PV system.

A real time charging/discharging scheme is built based on the battery's charging/discharging characteristics, and current and temperature dependence. The scheme can ensure that the scheduling algorithm is more accurate in charge/discharge control as well as the safe operation of a battery bank. The scheduling algorithm considers many aspects of battery characteristics that were not considered previously [92, 93, 94, 95]. Upon completion of the design, this real-time scheduling algorithm is implemented based on the VHDL-AMS method in SIMPLORER [96]. The PV/battery

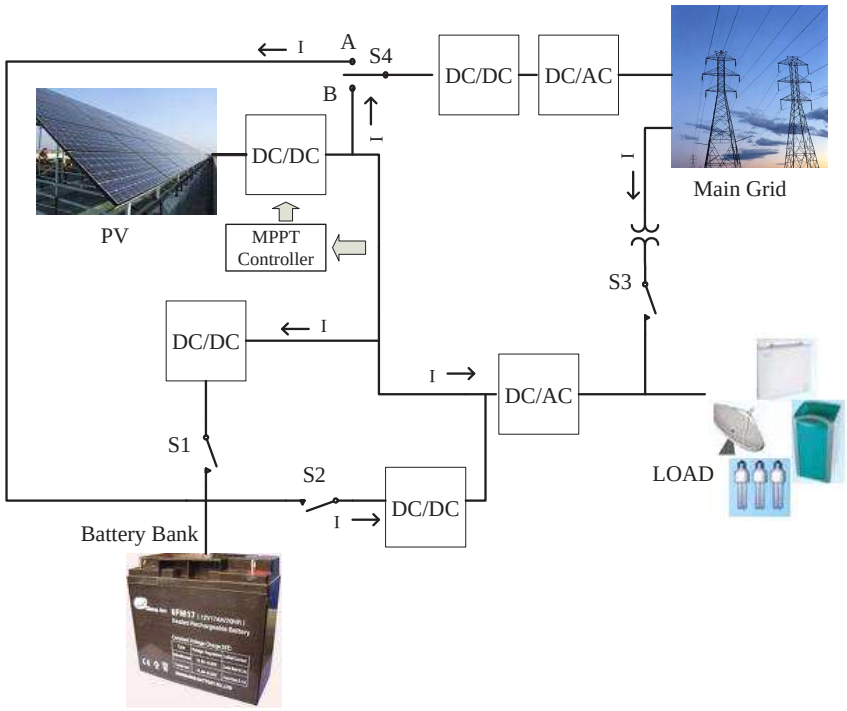

FIGURE 4.1: A simple PV/battery system structure

system shown in Figure 4.1 will be built in SIMPLORER for one-day real-time simulation purposes.

4.2 Real-Time Scheduling of Grid-Connected PV/Battery

The main aim of this system is to satisfy the requirements of the electrical loads qualitatively while maximizing the utilization of the renewable energy source and optimizing the operation of the battery bank and PV. Therefore, an efficient control strategy for this system is necessary. The developed control strategy must be capable of sensing the continuous variations in electrical loads and variation in power production from PV in order to be able to make fast and correct decisions. A successful operation is only possible through high quality of interaction among the battery bank, PV and grid.

4.2.1 Battery Unit Characteristics

In practice, the battery storage bank used in the PV/battery system could consist of a matrix of identical batteries based on the capacity of the PV array. The ULTRALIFE UBBL 10 lithium-ion battery is chosen to serve as the energy storage. The mathematical model of this battery can be built based on [97]. Dozens of identical batteries would be connected in series to boost the voltage level of the battery matrix, while multiple battery strings are connected in parallel to increase the working current level of the battery storage system. The rated capacity for the ULTRALIFE UBBL 10 lithium-ion battery is 6.8 AH. However the valid capacity depends on the discharge current and ambient temperature during the actual setup.

Table 4.1 shows the valid capacity rates of the battery at different discharge current rates when the ambient temperature is $25°C$. Table 4.2 shows the valid capacity rate of the battery at different ambient temperatures when the discharge current is 2 A. All the data is collected from the ULTRALIFE UBBL 10 lithium-ion battery test results [97].

TABLE 4.1: Valid capacity rate at different discharge current rates

Discharge current (A)	Valid capacity rate of battery
1.0	1.0
3.0	1.0
4.0	0.95
6.0	0.90

TABLE 4.2: Valid capacity rate at different ambient temperatures

Ambient temperature ($°C$)	Valid capacity rate of battery
-30	0.75
-20	0.93
25	1.00
50	1.01
60	1.01

4.2.2 Real-time Scheduling Algorithm

In this chapter, the scheduling is based on the characteristics of the battery. The valid capacity rate λ is affected by the discharge current and ambient temperature in practice. We define this relationship in (4.1).

$$\lambda = f(i(t), T) \tag{4.1}$$

where $i(t)$ is the discharge current of the battery bank, and T is the ambient temperature. Taking the derivative on both sides of (4.1) will yield

$$\partial\lambda = \frac{\delta f}{\delta i}\partial i + \frac{\delta f}{\delta T}\partial T \tag{4.2}$$

The corresponding ∂i, ∂T and $\partial\lambda$ can be easily calculated based on the data from Table 4.1 and Table 4.2. The superscript n is the index of different data points. Expressed them in matrix form, we get (4.3)

$$\begin{bmatrix} \partial\lambda^1 \\ \vdots \\ \partial\lambda^n \end{bmatrix} = \begin{bmatrix} \partial i^1 & \partial T^1 \\ \vdots & \vdots \\ \partial i^n & \partial T^n \end{bmatrix} \begin{bmatrix} \frac{\delta f}{\delta i} & \frac{\delta f}{\delta T} \end{bmatrix}^T \tag{4.3}$$

Using the least-square method to obtain the values of $\frac{\delta f}{\delta i}$ and $\frac{\delta f}{\delta T}$, then λ can be obtained as

$$\lambda = \frac{\delta f}{\delta i}(i - i_{ref}) + \frac{\delta f}{\delta T}(T - T_{ref}) + \lambda_{ref} \tag{4.4}$$

where the reference values can be chosen from Table 4.1 or Table 4.2. In this chapter, $\lambda_{ref} = 1.0$, $T_{ref} = 298K(25°C)$, and $i_{ref} = 1.0A$. The positive direction is defined when the current flows out from the battery. Hence the charge current is considered as a negative value. Normally SOD is defined as the state of discharge, which is shown in (4.5)

$$SOD = \frac{\int_0^t i d\tau}{Q} \tag{4.5}$$

Based on the definition, SOD is 0 at the beginning of discharge and is 1 when the battery is fully discharged. Generally speaking, i is the discharge current of the battery, and Q

is the capacity of the battery. If the discharging current i can be negative, i.e., it can represent the charging current, and t is the total time that the battery has been used. SOD gives an indication on the energy remains in the battery. For example, SOD is 0.5 after several charging and discharging cycles. This means that there is still one-half energy inside the battery.

In the real-time scheduling algorithm, SOD must be controlled between 0 and λ considering the safety of the battery. λ can be calculated using (4.1) based on the average discharge current in a short time and the ambient temperature. Here, the average current is used to avoid the effect of a big variation in discharge current. Charging/discharging current must be controlled to meet the safety requirement of the battery.

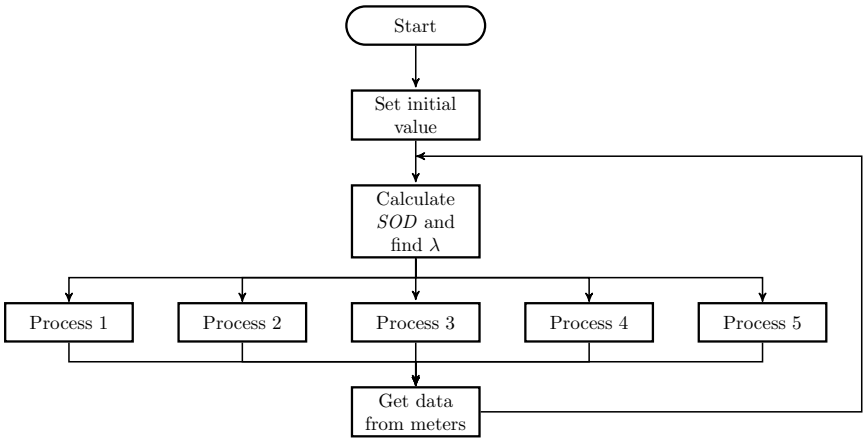

FIGURE 4.2: Real-time scheduling algorithm flow chart

The real-time scheduling algorithm is shown in the flow chart in Figure 4.2 and Figure 4.3. To make better use of the battery in the PV/battery system and control the charging/discharging of the battery in real-time, there are several rules which must be followed:

Process 1 When the power production from the PV is greater than load and the SOD of the battery bank is between 0 and λ, the PV will charge the battery so that the excess power is stored in the battery bank. Power is transferred from the PV to the load as well as from the PV to the battery bank. Switch 1 will be on.

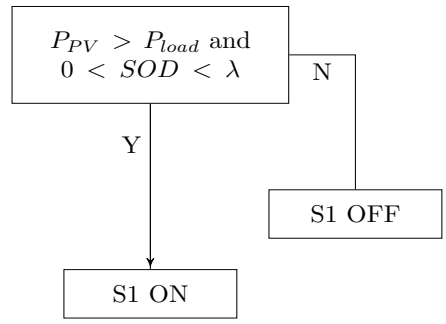

(a) Process 1

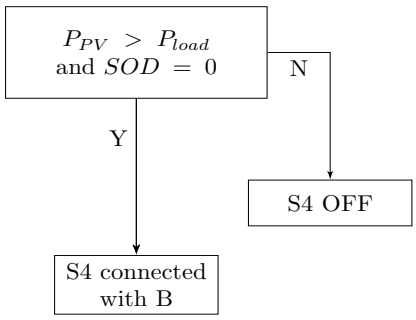

(b) Process 2

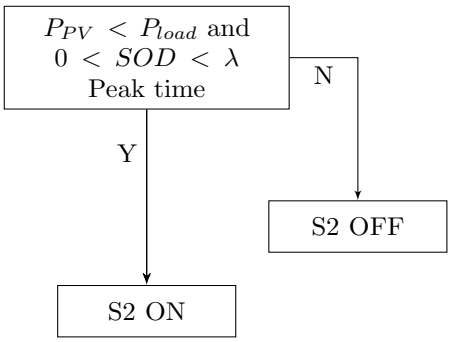

(c) Process 3

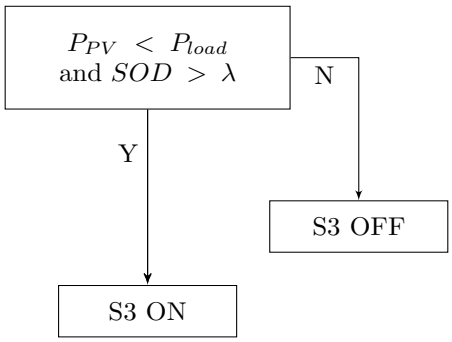

(d) Process 4

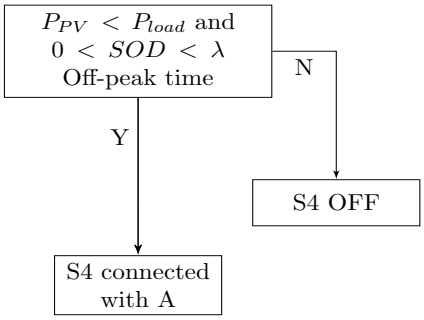

(e) Process 5

FIGURE 4.3: Process flow chart

Process 2 When the power production from the PV is greater than load and the SOD of the battery bank is equal than 0, the extra power from the PV will be sent to the main grid. Power is transferred from the PV to the load as well as from the PV to the main grid. Switch 4 will be connected with B.

Process 3 When the power production from the PV is less than load and the SOD of the battery bank is between 0 and λ, the battery bank will discharge its energy to the load during peak time. Power is transferred from the PV to the load as well as from the battery bank to the main grid. Switch 2 is on.

Process 4 When the power production from the PV is less than load and the SOD of the battery bank is greater than λ, the battery bank will not supply the energy to the system. Power is transferred from the PV to the load as well as from the main grid to the load. Switch 3 will be on.

Process 5 When the power production from the PV is less than load and the SOD of the battery bank is between 0 and λ, the battery bank will get charged from the main grid during off-peak time. Power is transferred from the PV to the load as well as from the main grid to the battery bank. Switch 4 will be connected with A.

Some economic issues are also considered in the rules. The battery bank should be charged during off-peak hours when there is no energy in the battery and should be discharged during peak hours if possible.

The processes in Figure 4.3 correspond to the state of switches in Figure 4.1, i.e. the state of switches 1-3 depends on processes 1-3, respectively. Processes 4 and 5 help to make decision for switch 4.

4.2.3 PV Array and Load

Electricity is generated when photons from sunlight hit electrons into a higher state of energy in the photovoltaic solar panel. The term photovoltaic denotes the unbiased operating mode of a photodiode in which the current flowing through the device is entirely caused by light energy. A PV array generates electric power by using solar cells

packaged in photovoltaic modules, often electrically connected in multiples, to convert energy from the sun into electricity.

Many mathematical descriptions of current/voltage terminal characteristics of PV cells can be used to model the PV cells [98, 99, 100]. These papers focus on the power production in the PV array. Because human activities follow certain cycles, most systems supplying energy services to a large population will experience similar cycles. They include the electric power system and PV system. One attractive factor of PV is that generation roughly correlates with the peak electricity demand of a selected area as shown in Figure 4.4 [101, 102].

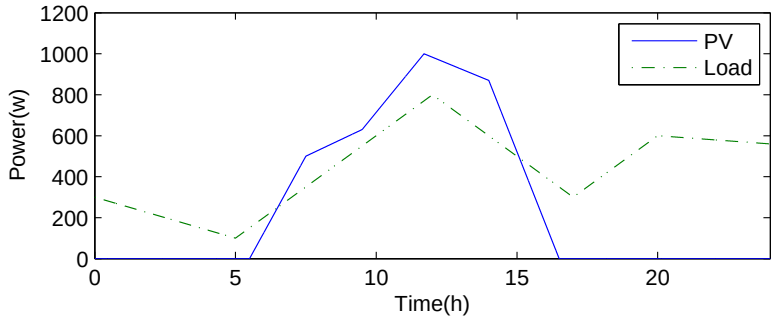

FIGURE 4.4: Sample hourly PV generation and System load

4.3 Simulation and Results

The PV and load can be built using the VHDL-AMS method in SIMPLORER based on the data of Figure 4.4. The battery bank also can be built in SIMPLORER using the method described in [7]. The control panel is built in SIMPLORER using the real-time scheduling algorithm which is described section II. The whole PV/battery system is shown in Figure 4.5.

The simulation system is simplified by using the DC power source in place of the AC power source, which does not affect the simulation results. The voltage sources E1, E2 and current source I3 are used to represent the main grid. I1 and I2 are used to control the charge and discharge current in a safe range, which can be implemented in practice by the controller of the power converter. The capacity of the battery bank is chosen as 6.8 AH. The method of choosing the capacity of the battery bank will be covered in

Chapter 6. The capacity can be easily changed by setting the appropriate parameter value in the battery model and it does not affect the analysis of the results.

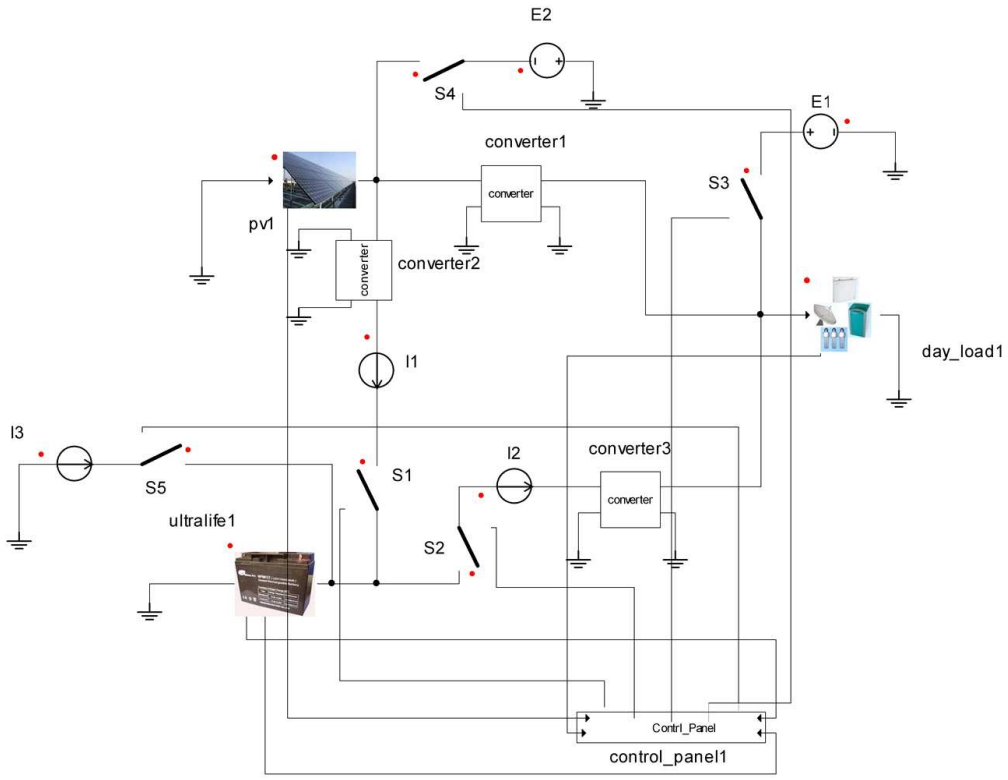

FIGURE 4.5: Simulation diagram of PV/battery system

The simulation PV/demand curve and the state of the battery bank are shown in Figure 4.6. The PV/demand curve is the same as the curve in Figure 4.4. The battery bank is charged when the power production from PV is greater than the demand or during the off-peak hours and is discharged when the power production from PV is less than the demand, which can be easily seen from Figure 4.6. SOD of the battery bank is kept at 0.92 at the end of the discharge cycle. This is because the discharge current is controlled at 5A in the simulation system. Based on the 5A of discharge current and the normal temperature, λ is found to be 0.92. This value is quite reasonable that the valid capacity will drop when discharge current goes higher as shown in Table 4.1. It closely meets the scheduling algorithm discussed in Chapter 4.2.2.

The switches (S1-S3) in the PV/battery simulation system correspond to those of the system shown in Figure 4.1 and the states of switches are shown in Figure 4.7. S5 and S4 correspond to S4 (A) and S4 (B), respectively.

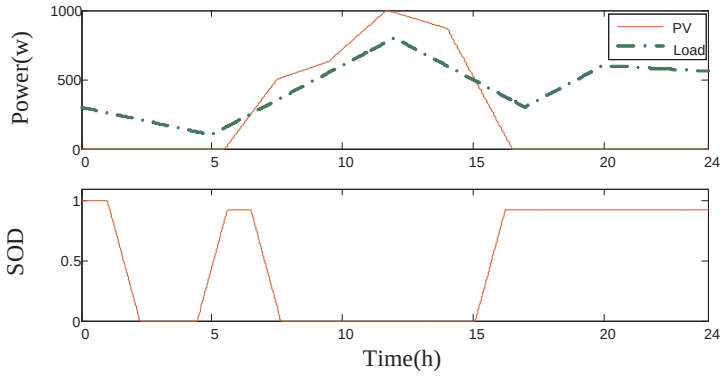

FIGURE 4.6: Simulation PV, demand curve and state of battery bank

Considering Figure 4.6 and Figure 4.7 together, SOD is 1 at the beginning of the simulation, which means that the battery bank is fully charged and cannot supply system load anymore. The power generated by PV is zero at that time. From Figure 4.7 the state of switch S3 is 1, which means that it is on and power is transferred from the main grid to the load.

During 01:00-04:00 in the morning, the switch of S4 (A) is turned on. The battery bank is charged at that time because it is the off-peak time defined in the control scheme in the simulation system. One hour later, the battery bank is fully charged (SOD = 0) and switch S4 (A) is turned off.

After 05:30, the PV starts to generate electricity. However the power is not enough for the load at that time. The switch S3 is turned on in Figure 4.7. Power is transferred from the grid to the load as well as from the PV to the battery bank. One hour later, the power generated by PV is greater than load. The power is transferred from the PV to the load as well as from the PV to the battery bank. Switch S2 is turned on at that time. The battery bank is fully charged (SOD = 0) at about 07:40 from Figure 4.6. The power generated by PV is still greater than load. Hence switch S4 (B) is turned on. Power is transferred from the PV to the load as well as from the PV to the main grid.

This situation of power transfer is kept until 15:06. After that the power production from the PV is less than the load requirement. Switch S2 needs to be turned on and the battery bank begins to supply load again. The battery bank is fully discharged at 16:15. λ is 0.92 at that time which is less than 1. However, the discharge current is 5

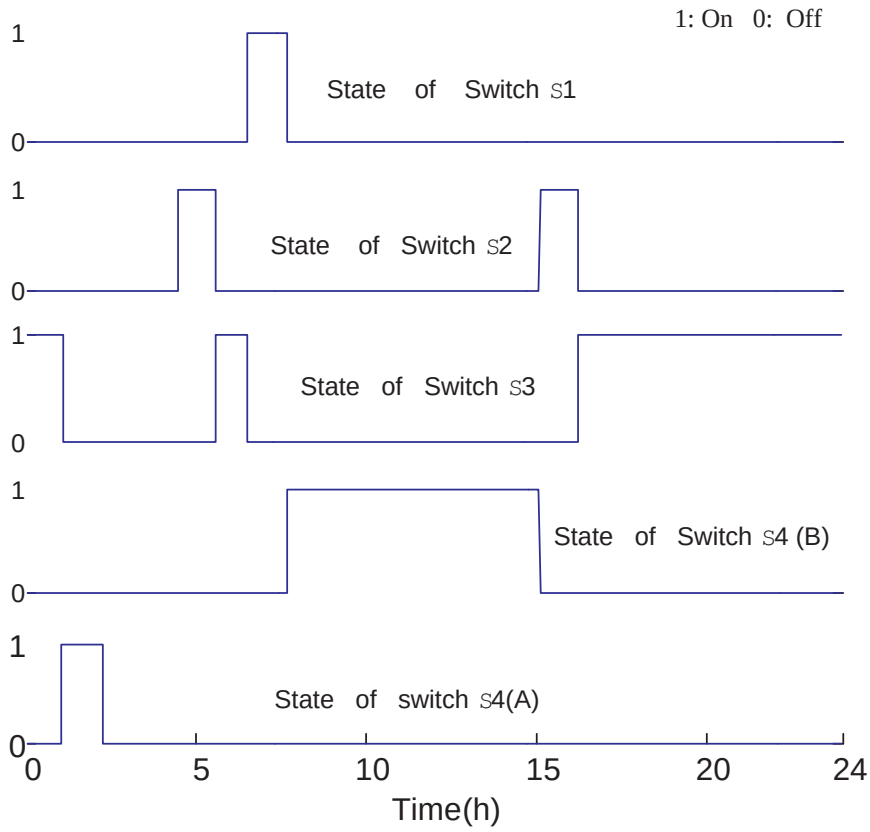

FIGURE 4.7: Simulated states of switches

A in this simulation system. Considering the safety of batteries discussed in Section II, switch S2 needs to be turned off to stop discharging. Switch S3 is turned on at that moment which means power is transferred from the PV to the load as well as from the main grid to the load. After 16:30, there is no power from PV. Power is transferred only from the main grid to the load.

4.4 Conclusion

In this chapter a special real-time scheduling algorithm of energy storage in a grid-connected PV/battery system has been developed and implemented in SIMPLORER using the VHDL-AMS method. The scheduling algorithm considers many aspects of battery characteristics that were not considered previously. They include battery's charging/discharging characteristics, and current and temperature dependence.

A simple simulation system has been built in SIMPLORER. The results of the one-day simulation using the scheduling algorithm have been analyzed. The valid capacity rate λ at different discharge currents and ambient temperatures has been discussed in the algorithm and it ensures that the battery bank works in its safe range. The simulation results match with the main design idea of the scheduling algorithm quite well.

Chapter 5

Multi-Objective Optimization for Smart Energy Management System

To understand the behavior of a smart grid, this thesis develops models suitable for overall analysis and design. The final goal is to lay a groundwork which would allow efficient management of the smart grid by minimizing the operating costs and by reducing the emission level while meeting the load demand. More specifically, the optimal AC power flow solution will be obtained to meet the unit and line constraints and for control of smart devices.

Unit Commitment (UC) and Optimal Power Flow (OPF) are two of the key functions in the operation of the MG, particularly in the network management of distribution systems. The UC function is responsible for economic optimization of the power system and the OPF function is responsible for the security optimization of the network. The OPF can be executed iteratively between active and reactive power security optimization until voltage violations and/or line overloads are all eliminated. When it executes in active power security mode, it eliminates or reduces existing overloads through rescheduling of generation, load shedding in the MG, and/or modifying power import/export with the upstream grid. In reactive power security mode, it eliminates or reduces existing over-/under-voltage through rescheduling of generator's reactive power,

flexible AC transmission systems (FACTS) via capacitor and reactor control and on-load tap changers (OLTCs).

Smart energy management system (SEMS) is a core part of a MG system, which can make this system more intelligent. In SEMS, the recommended MW/MVar amounts rescheduled are sent to generators, FACTS, OLTCs and load controllers for immediate implementation via communication devices. Through constant monitoring and real-time security control, it is possible to coordinate the operation of the MG and upstream grid supply such that the microgrid can aid the external system during system-wide emergency by exporting its generation as much as it could without jeopardizing its own security. At times of its own shortage, the microgrid can count on the upstream grid to meet its needs.

Many research papers have studied the UC and OPF works separately and independently [103], [104]. Few papers considered these two functions together without renewable energy resources and energy storage systems (ESS) [105], [106]. With the help of smart meters installed in the MG system, SEMS can make decision relatively fast for the unexpected situation. Also it needs to consider UC and OPF within SEMS to obtain a multi-objective optimization for both planning and real time operation. A new technique called the Jump and Shift method is developed, as a solution approach to solve these two problems at the same time. The design of the software algorithms and control schemes that can be used for network management of distribution systems while ensuring the economical operation of the MG will be presented. The Jump and Shift method is employed to yield multi-objective optimization as follows:

- Minimize the total UC schedule cost of the power system as well as the total line loss of the power system.
- Determine the scheduling and output of traditional power generators.
- Determine the charge and discharge period for the energy storage system.
- Determine the power transferred between the energy storage system and smart power system.
- Determine the reactive power injected for the power system with renewable energy resources.

- Obtain the optimal transformer tap ratios, and the optimal angle of the phase shifter to meet the voltage and line constraints.

5.1 Concept of Jump and Shift Method

The proposed Jump and Shift method aims to solve a large scale linear/nonlinear programming problem where the constraints are related to another large scale linear/nonlinear programming problem. Consider the following large scale problem A in (5.1).

$$\begin{aligned} Min \quad & c(\mathbf{x}) \\ s.t. \quad & g(\mathbf{x}) + \mathbf{p} = 0 \\ & \underline{\mathbf{h}} \leq h(\mathbf{x}) \leq \overline{\mathbf{h}} \end{aligned} \tag{5.1}$$

where,

$\mathbf{x} \in \Re^n$ is a vector of decision variables, including the control and nonfunctional dependent variables.
$c : \Re^n \rightarrow \Re$ is a scalar function that represents the cost function's optimization goal.
$g : \Re^n \rightarrow \Re^m$ is a vector function with equality constraints.
$\mathbf{h} : \Re^n \rightarrow \Re^p$ is a vector of nonlinear functional bounds and simple bound variables, with a lower bound $\underline{\mathbf{h}}$ and a upper bound $\overline{\mathbf{h}}$.
$\mathbf{p} \in \Re^m$ is a vector of decision variables, and it depends on problem B.

Another large scale problem B is described in (5.2).

$$\begin{aligned} Min \quad & ||\mathbf{p}||_2 \\ s.t. \quad & \mathbf{p} = g_1(\mathbf{x}, \mathbf{y}) \\ & f(\mathbf{x}, \mathbf{y}) = 0 \\ & \underline{\mathbf{h}}_1 \leq h_1(\mathbf{x}, \mathbf{y}) \leq \overline{\mathbf{h}}_1 \end{aligned} \tag{5.2}$$

where,

$||\mathbf{p}||_2$ is the norm of vector $\mathbf{p}$.
$\mathbf{x} \in \Re^n$ is the same vector of decision variables as that of problem A, and depends on problem A.
$\mathbf{y} \in \Re^n$ is a vector of decision variables, including the control and nonfunctional dependent variables.
$g_1 : \Re^n \to \Re^m$ is a scalar function that represents the vector of decision variables $\mathbf{p}$.
$f : \Re^n \to \Re^k$ is a vector function with equality constraints.
$\mathbf{h}_1 : \Re^n \to \Re^l$ is a vector of nonlinear functional bound and simple bound variables, with a lower bound $\underline{\mathbf{h}}_1$ and an upper bound $\overline{\mathbf{h}}_1$.

If these two problems are both very simple and small scale, it is very easy to solve by combining them together. A new combined problem in (5.3) is usually created.

$$\begin{aligned} Min \quad & c(\mathbf{x}) \\ s.t. \quad & g(\mathbf{x}) + g_1(\mathbf{x}, \mathbf{y}) = 0 \\ & f(\mathbf{x}, \mathbf{y}) = 0 \\ & \underline{\mathbf{h}} \leq h(\mathbf{x}) \leq \overline{\mathbf{h}} \\ & \underline{\mathbf{h}}_1 \leq h_1(\mathbf{x}, \mathbf{y}) \leq \overline{\mathbf{h}}_1 \end{aligned} \tag{5.3}$$

However, it is more difficult to solve the combined large scale problem. There is another way which can be used to solve this kind of problems. Consider the large scale problem A in (5.1). It can be solved with an initial value $\mathbf{p}_1$. The vector $\mathbf{p}_1$ is updated to $\mathbf{p}_2$ by using the problem B solution in (5.2). It continues until the value of $\mathbf{p}$ remains unchanged. This is the basic idea of the Jump and Shift method.

In the Jump and Shift method, any nonlinear programming technique such as the interior point method and genetic algorithm can be used to solve problems A and B. The interior point method (IPM) is chosen because it is a very effective method to solve the OPF problem and its implementation is easy [46].

To begin with, the following functions are defined in (5.4).

$$\begin{aligned} \mathbf{x} &= \mathcal{F}^{-1}(A)|_{\mathbf{p}} \\ \mathbf{y} &= \mathcal{G}^{-1}(B)|_{\mathbf{x}} \\ \mathbf{p} &= \mathcal{K}^{-1}(B)|_{\mathbf{x}} \end{aligned} \tag{5.4}$$

where,

$\mathcal{F}^{-1}$ is a function that represents solving $\mathbf{x}$ in problem A with an assumed value $\mathbf{p}$ by using the interior point method.
$\mathcal{G}^{-1}$ is a function that represents solving $\mathbf{y}$ in problem B with an assumed value $\mathbf{x}$ via the interior point method.
$\mathcal{K}^{-1}$ is a function that represents optimum $\mathbf{p}$ in problem B with an assumed value $\mathbf{x}$ via the interior point method.

A new parameter χ is defined in (5.5), which is also called the shift factor where the variable $\mathbf{x}^{new}$ is used to replace the variable $\mathbf{x}$ in problem B.

$$\left|\frac{\mathbf{x}(i)^{new} - \mathbf{x}(i)}{\mathbf{x}(i)}\right| \leq \chi \qquad \forall i \tag{5.5}$$

The $\mathbf{x}(i)$ represents the i^{th} scalar variable of the vector variable $\mathbf{x}$. The constraints of $\mathbf{x}$ also apply to $\mathbf{x}^{new}$. A small value of χ will lead to a better convergence speed, which may also increase the risk of non-convergence. Based on the simulation, χ will slow the convergence speed if it is greater than 10%. In this report χ is chosen as 3% for the smart energy management system optimization problem. This would make the problem converge fast with a reasonable good accuracy.

In the Jump and Shift method, equation (5.4) can be considered as the jump action of the solution process and equation (5.5) represents the shift action of the solution process.

Starting with the initial value $\mathbf{p}_1$ in problem A, one can get $\mathbf{x}_1 = \mathcal{F}^{-1}(A)|_{\mathbf{p}_1}$ in (5.4). Then $\mathbf{x}_1$ can be used to solve problem B. In the Jump and Shift method, the factor χ is used to relax $\mathbf{x}_1$ to $\mathbf{x}_1^{new}$, which makes problem B easier to solve. It also enhances the probability of problem B in getting the minimum $\mathbf{p}$ for every update. After that, $\mathbf{p}_2$ is obtained by $\mathbf{p}_2 = \mathcal{K}^{-1}(B)|_{\mathbf{x}_1^{new}}$ in (5.4). One can also get $\mathbf{y}_1$ by $\mathbf{y}_1 = \mathcal{G}^{-1}(B)|_{\mathbf{x}_1^{new}}$ in (5.4). Next replace $\mathbf{p}_1$ by $\mathbf{p}_2$ and the process continues. The process stops when $||\mathbf{p}_{n+1} - \mathbf{p}_n||_2 \leq \varepsilon$, where n and $n+1$ are the iteration steps of the Jump and Shift method, and ε is the convergence tolerance. The whole idea is shown in the following iterative process, where $\mathbf{p}_n$ is updated by $\mathbf{p}_{n+1}$ and $\mathbf{y}_n$ is set as the initial value of

problem B.

$$\left.\begin{array}{l} Problem\ \ A \\ \mathbf{p}_n \\ Problem\ \ B \end{array}\right\} \Rightarrow \mathbf{x}_n \rightarrow \mathbf{x}_n^{new} \Bigg\} \Rightarrow \left\{\begin{array}{l} \mathbf{p}_{n+1} \\ \mathbf{y}_n \end{array}\right.$$

Figure 5.1 shows the iterative process. This iterative process will continue until the solution converges. The start point is chosen as $\mathbf{x}_0$. The interior point method is used here to obtain the expected solution $\mathbf{x}_1$ (jump action), which would be found in the area bounded on condition 1 ($\mathbf{p} = \mathbf{p}_1$) in problem A. Then use $|\frac{\mathbf{x}_1(i)^{new} - \mathbf{x}_1(i)}{\mathbf{x}_1(i)}| \leq \chi$ to get a small search circle where χ is the radius for each element of $\mathbf{x}_1^{new}$ under a preset shift factor χ (shift action). Problem B is next solved to get condition 2 ($\mathbf{p} = \mathbf{p}_2$) for problem A. $\mathbf{x}_1^{new}$ is also searched in the area defined in equation (5.5) by solving problem B. This process is repeated under condition 2 and a new start point is set as $\mathbf{x}_1^{new}$. After executing the interior point solver the solution $\mathbf{x}_2$ is obtained.

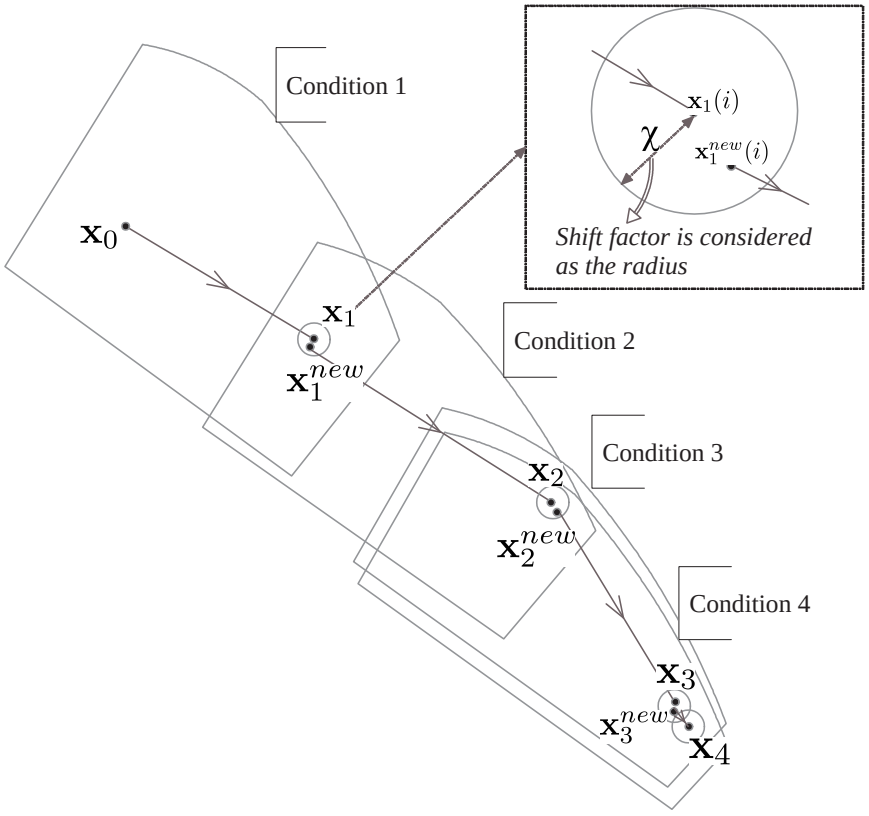

FIGURE 5.1: Process of Jump and Shift Method

The process will go on until condition $\mathbf{p}$ is stable and acceptable, which means that $||\mathbf{p}_{n+1} - \mathbf{p}_n||_2 \leq \varepsilon$. During this process, different $\mathbf{p}$ values represent different conditions, e.g. condition 1 is represented by $\mathbf{p} = \mathbf{p}_1$. Each scalar element in vector $\mathbf{x}$ will have its own search circle bounded by the radius χ in (5.5).

The Jump and Shift method will converge on condition that $\mathbf{p} = \mathbf{p}_e$ and will solve the whole problem under that condition. As shown in Figure 5.1, the condition gets closer to the optimal situation where $||\mathbf{p}_{n+1} - \mathbf{p}_n||_2 \leq \varepsilon$. The flow chart of the Jump and Shift method is shown in Figure 5.2 and the calculation details will be shown in a case study later.

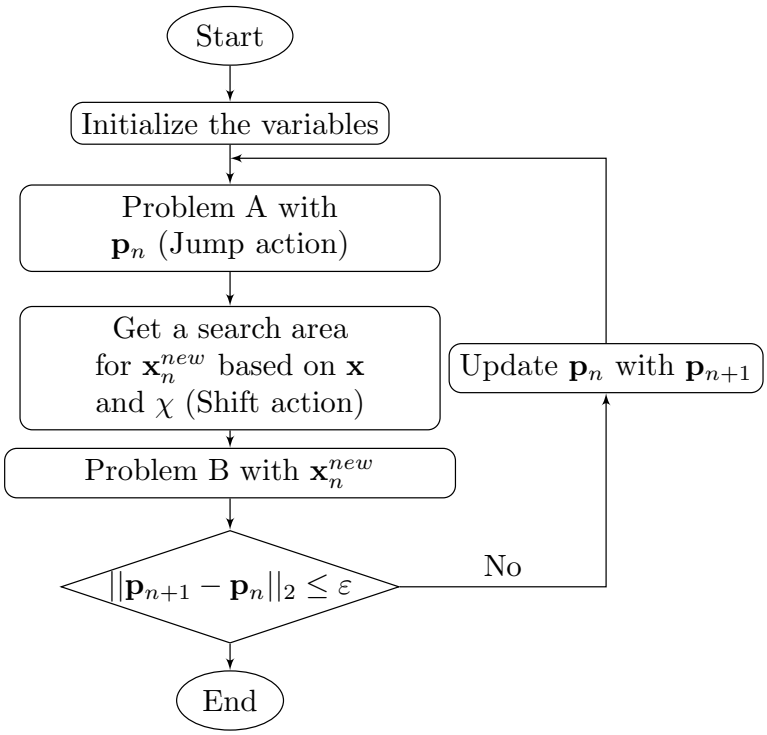

FIGURE 5.2: Flow chart of Jump and Shift Method

The Jump and Shift method offers a new way to solve a large scale multi-objective problem with the help of typical nonlinear programming techniques. The interior point method is incorporated to solve the multi-objective optimization problem via the Jump and Shift method. If the shift factor χ is infinity, the main problem will change to solving two independent problems. The IPM will solve these two independent problems

and its convergence has been discussed in [46]. The vectors, $\mathbf{p}_n$ and $\mathbf{p}_{n+1}$, will be the same in every iteration step, which means that $||\mathbf{p}_{n+1} - \mathbf{p}_n||_2 \equiv 0$.

If the shift factor χ is zero, the main problem will change to solving a decomposition problem. Based on the theorem in [107], [108], which states that problem C is a partitionable problem and it can be decomposed into problem A and problem B. After running the solution algorithm, an optimal solution will be obtained for problem A and problem B or proves that there is no optimal solution for the initial partitionable problem C or the decomposed problems including problem A and problem B. The decomposed problems will converge if the initial partitionable problem converges.

The shift factor χ is a small value, e.g. 3%. The vector $\mathbf{x}$ in problem B will be updated by $\mathbf{x}^{new}$. However, $\mathbf{x}^{new}$ will also follow the same constraints of $\mathbf{x}$ in problem (5.3) as specified in II.A, which means that problem B is a subproblem in (5.3). Following the theorem in [109], It will converge or there is no solution for the initial combined problem (5.3).

5.2 System Modeling and Problem Formulation

5.2.1 System Modeling

The output power of the wind generator can be considered as a function of wind speed [110], [111]. A piecewise linear function can be used to fit the relationship between output power and wind speed (v).

PV power is a generic term used for electrical power that is generated from sunlight. A PV system converts sunlight into electricity. The fundamental building block of PV is the solar cell or photovoltaic cell [59]. The forecasting data of the PV output power based on the maximum power point tracker is used for implementation of the PV module [60], [112], [113].

Traditional generators have several kinds of supply curves, e.g. linear or quadratic functions, as shown in Chapter 2. Normally, a generator cost file comprises the incremental cost curve and the start-up cost curve is used. The quadratic function is more accurate and is frequently adopted. This is used in this chapter.

Lithium ion (Li-ion) batteries are chosen as energy storage. The charge and discharge equations are shown in (2.12). P_t^E is the power supplied by the battery bank during the time period t. When P_t^E is positive, it means that the battery bank is discharged. When P_t^E is negative, the battery bank is charged up [7], [114]. The modeling of the battery bank can be found in Chapter 2.

5.2.2 Problem Formulation

5.2.2.1 Unit Commitment with Renewable Energy and Energy Storage

It is more complex to solve an optimal unit commitment schedule, especially when renewable energy resources and energy storage are included. The optimal solution is constrained by limits such as the hourly minimum spinning reserve, generator minimum up/down times, ramp rates and network security [104]. The formulation is as follows:

Minimize the total UC schedule cost (TC),

$$\begin{aligned} Min: \quad TC = & \textstyle\sum_t \sum_{n\in CG}(r_n R_{tn} + d_n SU_{tn} \\ & + U_{tn}(a_n + b_n P_{tn} + c_n P_{tn}^2)) \\ & + \textstyle\sum_t \sum_{n\in WG}(U_{tn} P_{tn} c_w) \\ & + \textstyle\sum_t \sum_{n\in PV}(U_{tn} P_{tn} c_{pv}) \end{aligned} \tag{5.6}$$

To solve the problem in (5.6), one needs to consider the following constraints:

Real power balance:

$$\begin{aligned} \textstyle\sum_{n\in CG} P_{tn} + \sum_{n\in WG} P_{tn} + \sum_{n\in PV} P_{tn} \\ + \textstyle\sum_{n\in ES} P_{tn} = \sum_i PD_{ti} + P_{Loss}^t \end{aligned} \quad \forall t \tag{5.7}$$

Unit spinning reserve capacity:

$$\begin{aligned} R_{tn} \le min\{R10_n U_{tn}, \quad & P_n^{max} U_{tn} - P_{tn}\} \\ & \forall t, n \in CG \end{aligned} \tag{5.8}$$

Capacity of largest online generator:

$$SR_t \geq P_n^{max} U_{tn} \qquad \forall t, n \in CG \tag{5.9}$$

System online reserve:

$$\sum_{n \in CG} R_{tn} + \sum_{n \in ES} C_{n,t} \geq \alpha SR_t \qquad \forall t \tag{5.10}$$

System 10-min reserve:

$$\begin{aligned} \textstyle\sum_{n \in CG} R_{tn} + \sum_{n \in G10} (1 - U_{tn}) P10 \\ + \textstyle\sum_{n \in ES} C_{n,t} \geq SR_t \qquad \forall t \end{aligned} \tag{5.11}$$

where CG, WG and PV are sets of conventional, wind and PV generators; n and t are subscripts indicating generator and hour respectively; a_n, b_n and c_n are cost coefficients of conventional generators; U_{tn} and SU_{tn} are vectors of binary integers representing unit status and start up status of units; r_n and d_n are the reserve cost and start up cost respectively; c_w and c_{pv} are the wind and PV energy cost respectively; P_{tn} is the output power of a generator; and R_{tn} is the online spinning reserve of a conventional generator. ES is the set of energy storage system; PD_{ti} is the power demand at the ith bus during the time period t; and P_{Loss}^t is the minimum power grid loss during the time period t, which can be obtained by solving the objective function in (5.12). $R10_n$ is the 10-min spinning reserve capacity. SR_t is the hourly required reserve capacity for the system. The system spinning reserve criteria are shown as two constraints in (5.10)-(5.11). ESS is considered in these criteria. $P10$ is the capacity of the 10-min quick start units; $G10$ is the set of 10-min quick start up units; α is the factor of the hourly online reserve to be maintained online; $C_{n,t}$ is the available energy stored in the nth ESS during the time period t; and the third term in (5.11) is the total energy stored in ESS minus its minimum capacity limit.

Meanwhile, the generator output limits, ramp rate limits and minimum up/down time limits need to be considered in this problem. For pollution-free and energy sustainability, the renewable energy is always assumed on.

5.2.2.2 Optimal Power Flow with Renewable Energy and Energy Storage

Usually the OPF performs the minimization of an objective function representing the generation cost and/or the transmission loss. The renewable energy and ESS are considered in the OPF problem. The constraints involved are the active/reactive power balance, the physical laws governing the power generation-transmission system and the operating limits of the equipment [115]. The formulation is as follows:

Minimize the total power system loss:

$$Min: \qquad P^t_{Loss} = \sum_{l=1}^{L} |real(V^l_{kt} I^{l*}_{kt} - V^l_{mt} I^{l*}_{mt})| \tag{5.12}$$

subject to the following constraints:

Active power balance:

$$\begin{aligned} P^G_{it} - P^L_{it} &= P^N_{it} \\ &= V_{it} \textstyle\sum_j V_{jt} Y_{ij} \cos(\theta_{it} - \theta_{jt} - \phi_{ijt}) \ \ \forall i, j, t \end{aligned} \tag{5.13}$$

Reactive power balance:

$$\begin{aligned} Q^G_{it} - Q^L_{it} &= Q^N_{it} \\ &= V_{it} \textstyle\sum_j V_{jt} Y_{ij} \sin(\theta_{it} - \theta_{jt} - \phi_{ijt}) \ \ \forall i, j, t \end{aligned} \tag{5.14}$$

where V^l_{kt}, I^l_{kt}, V^l_{mt}, and I^l_{mt} are voltages and currents at the $from$ bus and the to bus of transmission line l during the time period t, respectively. I^{l*}_{kt} and I^{l*}_{mt} are the conjugate variables of I^l_{kt} and I^l_{mt} respectively. P^G_{it} is the injected real power at bus i during the time period t, which includes the conventional and renewable energy. P^L_{it} is the active load power at bus i and P^N_{it} is the active power transferred out from bus i. Bus i is connected to bus j. Q^G_{it} is the injected reactive power at bus i; Q^L_{it} is the reactive load at bus i; and Q^N_{it} is the reactive power transferred out from bus i. The limits of power lines, bus voltages and power generation also need to be considered.

5.3 Multi-Objective Optimization Algorithm Based on Jump and Shift Method

Most UC problems, with or without active power flow, have been studied for several decades. However, these are not sufficient to cater for smart grid applications as they did not consider all the decision variables at the same time. It will be an improvement if the grid operators know the present and future active power output of generators and injected reactive power to make sure that the voltages meet the customer needs, while transformer taps and phase shifters are set optimally for some future hours in SEMS [42]. This chapter aims to design a multi-objective optimization algorithm to solve cost minimization as well as loss minimization at the same time for the MG. This will predict the injected active and reactive power, bus voltages and angles, optimal transformer tap ratios and phase shifter angles.

The multi-objective optimization algorithm based on the Jump and Shift method is shown in Figure 5.3. In the Jump and Shift method, problem A is the main problem. Solving problem B helps to solve the main problem A. The UC problem (5.6-5.11) is problem A and optimal power flow (5.12-5.14) is problem B. The power loss P_{loss} is considered as the variable $\mathbf{p}$ in (5.1). The generator on/off state U and real power output P_g which includes conventional generators, renewable energy generators and energy storage are considered as vector $\mathbf{x}$ in (5.1). The vector $\mathbf{y}$ in problem B is solved and it includes the injected reactive power Q_g, bus voltage magnitudes V and angles θ, optimal transformer tap ratios τ and phase shifter angles ψ.

System losses are a function of line parameters, unit generation, and system load and net interchange. Unit generation is increased or decreased as dictated by the loss sensitivities of unit penalty factors. A unit which results in positive loss sensitivity, i.e., an increase in unit generation results in more system losses, will be penalized by generating less MW output. Likewise, a unit which results in negative loss sensitivity will be asked to generate more MW output. If the total incremental cost due to the increase in generation is lower than the total decremental cost due to the decrease in generation, then a lower UC cost will result when the losses are minimized. Otherwise a higher UC cost may result. Hence it is difficult to say whether a minimum UC cost will always lead to a minimum system loss and vice versa as this depends on system parameters and operating conditions. The proposed solution is a trade-off technique where it attempts

to give the best possible solution, i.e. it gives the best compromise solution between the UC cost and system loss.

In this chapter, only the isolated mode is considered. However, the interconnected mode can be similarly treated by including the electricity market price in (5.6). This means that the objective function in (5.6) maximizes the MG benefit and the neighboring power system or upstream network contributes the system online spinning reserve in (5.10).

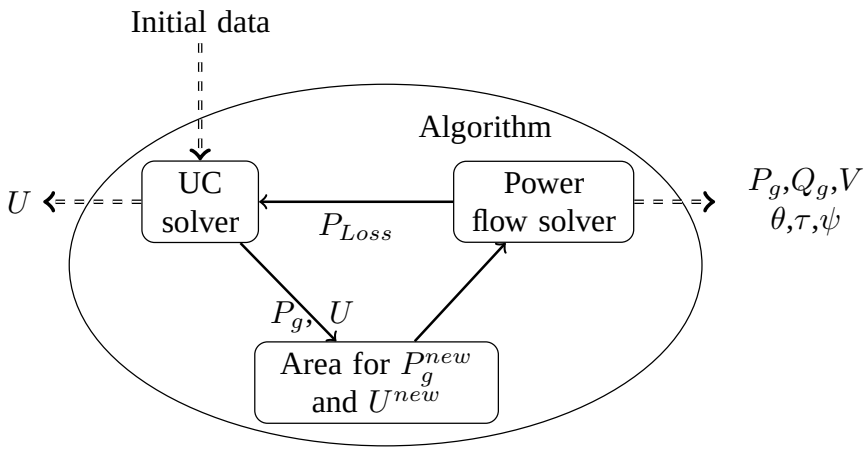

FIGURE 5.3: Data flow of multi-objective optimization algorithm via Jump and Shift Method

The multi-objective optimization algorithm is implemented in A Modeling Language for Mathematical Programming (AMPL) [88], where solver KNITRO is used to solve the minimization problem. The UC solver is designed to solve the UC problem and obtain the generator schedule U and active power output P_g. The objective function is the same as (5.6). A power flow solver is designed to solve the problem in (5.12-5.14). The optimal transformer tap ratios τ, phase shifter angles ψ, active power P_g and injected reactive power Q_g are obtained to meet the line and voltage constraints. As shown in Figure 5.3, U and P_g are obtained from the UC solver and U^{new} and P_g^{new} are bounded in a small circle of the shift factor χ. P_{loss} is passed from the power flow solver to the UC solver. Considering U and U^{new} are integers and χ is a small value of 0.03 in this case, $U^{new} = U$ as computed in (5.5). This means that only P_g is updated to P_g^{new}, which can simplify the solution problem greatly.

The above idea can be strictly formulated in the following multi-objective optimization algorithm:

1. Initialize the variables. Set the parameters for the power system model and input the forecasting load during the entire study time period T.
2. Run the UC solver with the initial P_{Loss} to get U and P_g.
3. Get a small circle for U^{new} and P_g^{new}. Set $t = 0$.
4. Let $t = t+1$. Run the OPF solver with the small circle for U^{new} and P_g^{new} obtained from step 3.
5. If $t \leq T$, then go to step 4.
6. Calculate the changes in system loss ΔP_{Loss}.
7. If $\Delta P_{Loss} \leq \varepsilon$, then update P_{Loss} by using $P_{Loss} = P_{Loss} + \Delta P_{loss}$ and go to step 2 with the new P_{Loss}.

The flow chart of the algorithm is shown in Figure 5.4.

With appropriate modifications, the proposed Jump and Shift solution method can also be used to solve other multi-objective problems. For example, (i) the dispatchers at the Power System Control Center (PSCC) may be interested in minimizing the UC schedule cost while maximizing the system reliability as part of the short-term power system operation problem and (ii) the planning engineers may be interested in minimizing the transmission line investment cost while maximizing the system reliability as part of the long-term reliability-cost/reliability-worth evaluation.

5.4 Test System and Results Analysis

5.4.1 Test System

A 14-bus MG is tested to verify the multi-objective optimization algorithm based on the Jump and Shift method. This power system is modified from the IEEE 14-bus test system. In this system, there are three conventional generators, one wind generator, one PV generator and one battery bank as ESS. Three conventional generators are located at buses 1, 2 and 4. The wind generator and ESS are located at bus 3. The PV energy

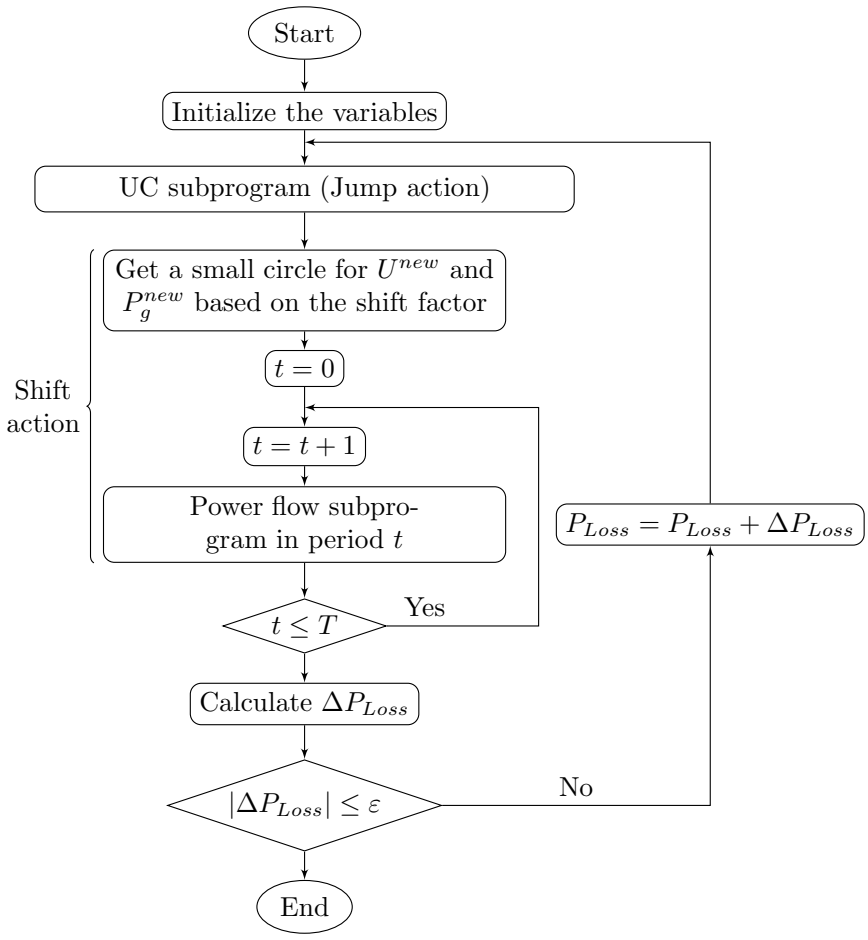

FIGURE 5.4: Flow chart of the multi-objective optimization algorithm

source is located at bus 12. In this 14-bus power system, there are also three synchronous condensers and one fixed capacitor located at buses 3, 8, 12 and 9, respectively. They provide the reactive power to support the power system. Three tap changing under load (TCUL) transformers are also used in this system to maintain the bus voltages. The cost data of the conventional generator is shown in Table 5.1.

Assume that we have the forecast wind speed data in a day as in Figure 5.5 (a). The parameters of this wind generator are given as: $p_r = 1000kW$, $v_c = 3m/s$, $v_r = 12m/s$, and $v_f = 30m/s$. Then the output of the wind generator can be obtained from [110], which is shown in Figure 5.5 (b). The forecasting output of the PV generator is shown in Figure 5.6. The cost coefficients of the wind energy generator and PV generator are $c_w = 0.06\$/kWh$ and $c_{pv} = 0.15\$/kWh$ respectively.

TABLE 5.1: Conventional generator data

Gen #	Bus #	a ($)	b ($/kW$)	c ($/kW^2$)	P_n^{min} (kW)	P_n^{max} (kW)	d ($/start)
1	1	80	0.03	0.000001	100	3000	50
2	2	200	0.06	0.000002	100	3000	30
3	4	1000	0.05	0.000003	100	3000	5

Gen #	r ($/kW$)	UT (hrs)	DT (hrs)	IC (hrs)	P10 (kW)	R10 (kW)	R60 (kW)
1	0.006	3	3	0	0	3000	3000
2	0.009	2	2	1	0	3000	3000
3	0.030	0	0	-1	3000	3000	3000

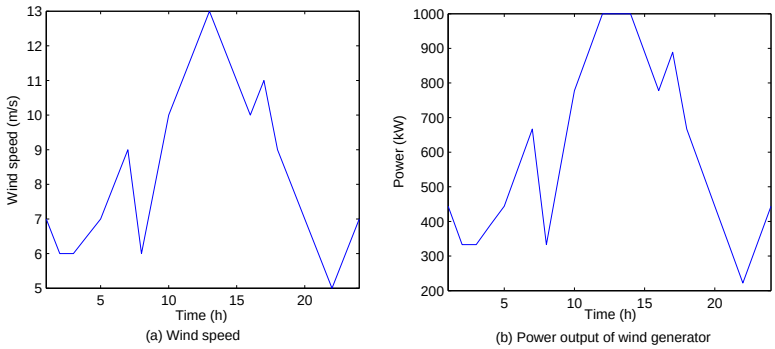

FIGURE 5.5: Forecast wind speed and wind power

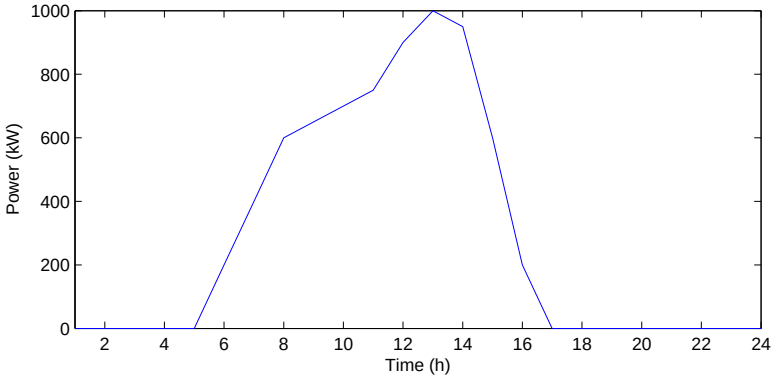

FIGURE 5.6: Forecast PV power

The active and reactive power values at the load bus in this 14-bus MG power system are shown in [116]. The line parameters can be obtained from the IEEE 14-bus test system [117].

To verify the Jump and Shift method in a larger power system, this chapter expands the above MG to a 112-bus power system by connecting eight MGs together. The line and branch parameters are shown in [118].

5.4.2 Test Results and Extended Analysis for 14-Bus MG Power System

The Jump and Shift method is used to solve multi-objective optimization for the smart energy management of the 14-bus MG. The shift factor χ is set at 0.03. The parameter α can be as low as 0.25 [119] and is set to 0.25 in this case.

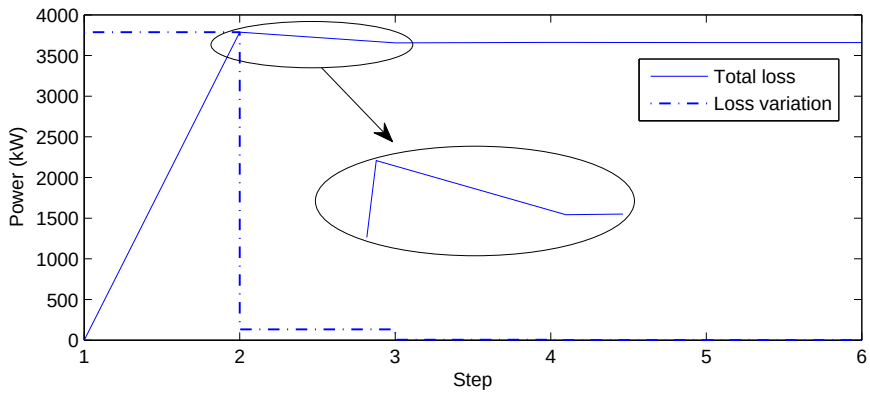

FIGURE 5.7: The total power loss at each solution step for 24-hour period

The total power loss for the 24-hour period at each solution step is shown in Figure 5.7. The initial value of P_{Loss} is set at $0kW$. Then it changes to $3,786.8kW$. After several steps, it stabilizes at $3,660.2kW$. The loss variation $|\Delta P_{Loss}|$ is also shown in Figure 5.7. $|\Delta P_{Loss}|$ is $3,786.8kW$ at the beginning. Then it changes to $132.04kW$ after second step and reaches $0.0105kW$ at the third step. Considering the Jump and Shift method in Figure 5.1, one can say that the loss variation $|\Delta P_{Loss}|$ in Figure 5.7 becomes smaller and smaller. The Jump and Shift method converges at $P_{Loss} = 3,660.2kW$ and the whole problem is solved under this condition. The total UC schedule cost via each step of the algorithm is shown in Figure 5.8. It converges very fast, e.g. three iterations and

remains unchanged from here onwards. One can get the final TC $\$8,457$ from Figure 5.8.

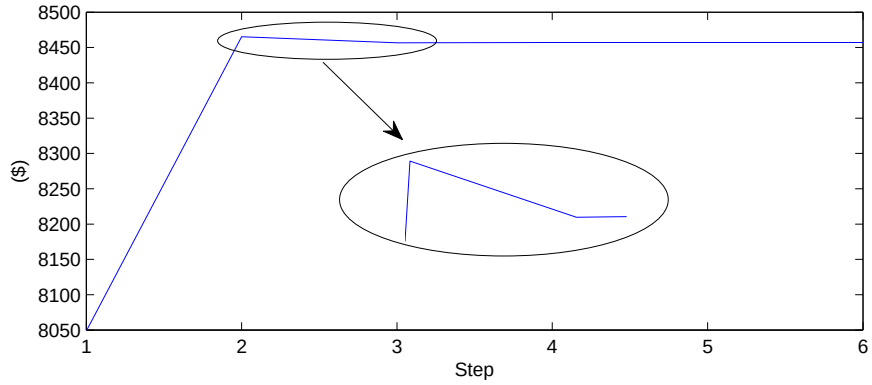

FIGURE 5.8: The total UC cost at each solution step

In multi-objective optimization for the smart energy management of the 14-bus MG, the total loss P_{Loss} is calculated by summing up the hourly loss of the day (24 hours). The changes of active power loss in each hour is shown in Figure 5.9. The study time is one day. Hence, there are 24 curves of power loss in each hour and they change as the solution step varies in Figure 5.7. Each of these curves exhibits the same characteristics and tendencies as those of the total loss P_{Loss}. They stabilize at the end of this solution algorithm.

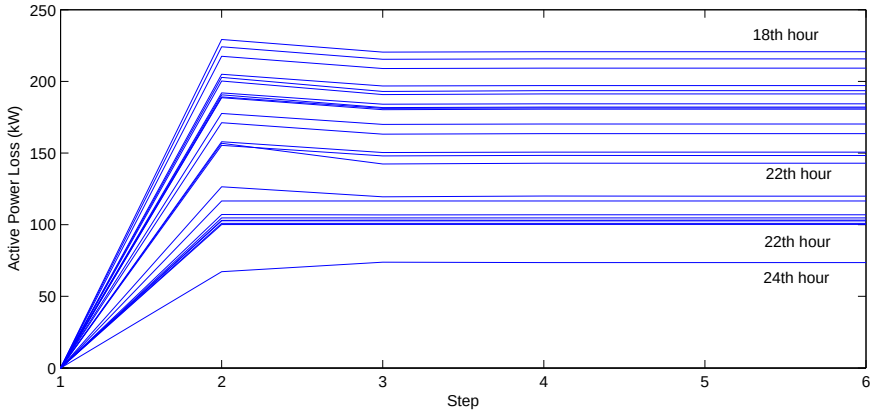

FIGURE 5.9: The active power loss in each hour at each solution step

5.4.2.1 Scheduling Results of Conventional Units and ESS

As mentioned before, the renewable energy generators are always on for pollution-free and sustainable properties. The schedule of the conventional generators and ESS are the control parameters for the SEMS of this 14-bus MG. After optimization and based on the Jump and Shift method, the schedule of conventional generators is shown in Table 5.2, where 1 is on, and 0 is off. $CG1$, $CG2$ and $CG3$ are the conventional generators at buses 1, 2 and 4.

TABLE 5.2: Schedule of conventional generator data

Hour	CG1	CG2	CG3	Hour	CG1	CG2	CG3
1	1	0	0	13	1	1	0
2	1	0	0	14	1	1	0
3	1	0	0	15	1	1	0
4	1	0	0	16	1	1	0
5	1	0	0	17	1	1	0
6	1	0	0	18	1	1	0
7	1	0	0	19	1	1	0
8	1	1	0	20	1	1	0
9	1	1	0	21	1	1	0
10	1	1	0	22	1	1	0
11	1	1	0	23	1	1	0
12	1	1	0	24	1	0	0

The system active power balance is shown in Figure 6.8 (a). The total system loss of each hour is considered here. Three curves are shown in Figure 5.10 (a). They are the hourly load curve, the combined hourly load and loss curve and the hourly kW output of the combined CG, WG and PV curve. In the traditional power system, the generation should meet the load demand and losses. However, it does not happen in this case because of the presence of ESS in this smart system. When the generation is lower than the sum of demand and loss, ESS supplies the deficiency by discharging its energy into the grid. When the generation is higher than the demand, ESS stores the energy from the grid. The charging and discharging of ESS are shown in Figure 5.10 (b), where energy discharge is reflected as a positive value. The control of ESS is based on the cost function (5.6) as obtained from the Jump and Shift method.

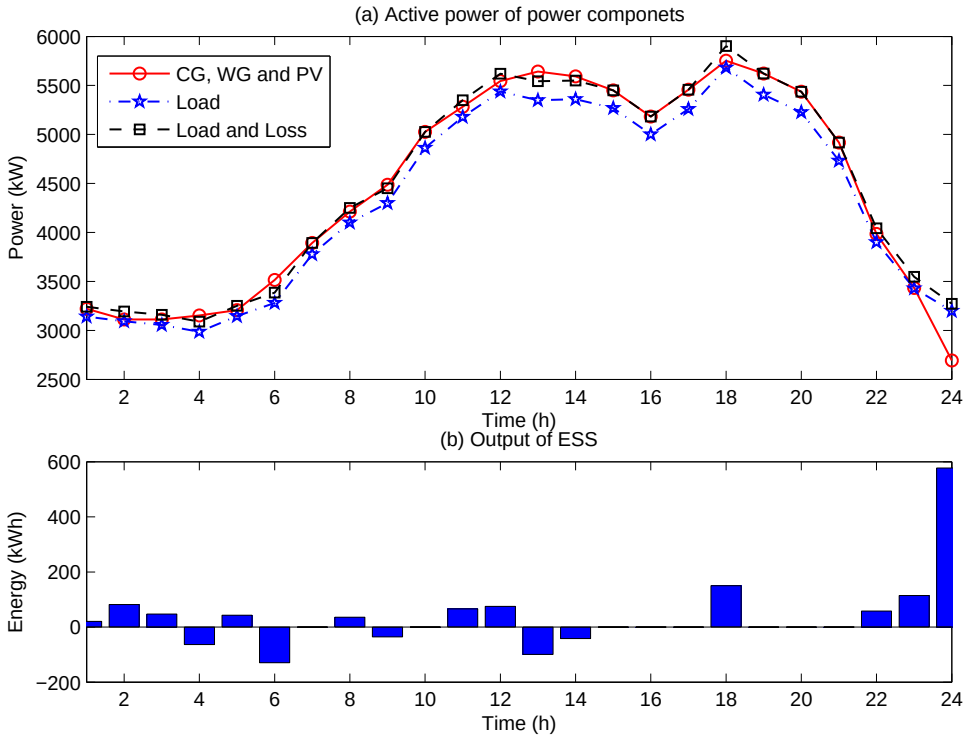

FIGURE 5.10: Active power of power components and output of ESS in 14-bus system

The energy stored in the ESS is shown in Figure 5.11. A battery bank is used in the ESS of this system. The batteries are constrained by the maximum and minimum energy stored in them. In this case, the maximum energy in the battery bank is set at $1000kWh$, which is the rated capacity of ESS. The minimum energy is set at $100kWh$. As shown in Figure 5.11, the energy stored in the ESS is between these two limits.

The spinning reserve for the MG is shown in Figure 5.12. Curve 1 is the hourly total system generation which includes load and power loss. Curve 2 is the minimum online capacity, which includes power output of all units, available energy stored in ESS and online spinning reserve of CG. Curve 3 is the hourly total capacity of online units and ESS. Curve 4 is the hourly total available capacity, which includes the total capacity of all on-line and off-line conventional generators, the renewable power output from PV and wind turbine and the hourly available energy stored in ESS.

In this 14-bus power system, unlike traditional power systems, ESS is also considered as a source of online spinning reserve. There is no start up cost for ESS, which is also a

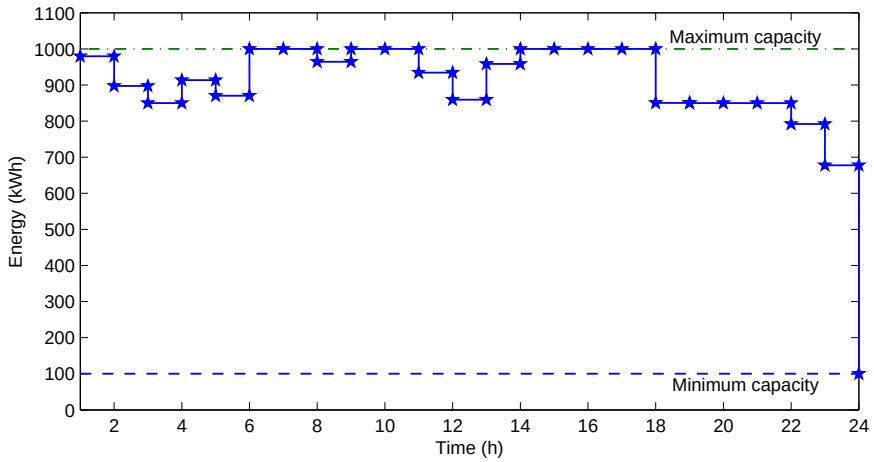

FIGURE 5.11: Energy stored in ESS

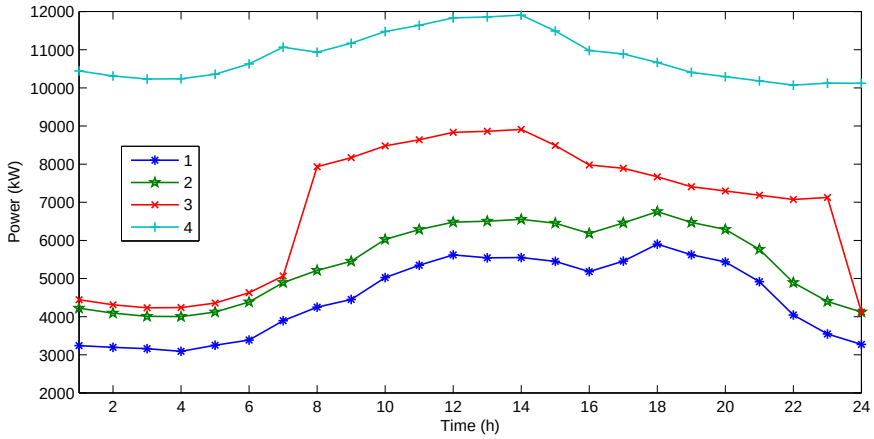

FIGURE 5.12: Spinning reserve with renewable energy and ESS

plus point for considering ESS as a source of online spinning reserve. Comparing Figures 5.12 and 5.11, one can easily show that ESS is considered as a source for spinning reserve contribution. It can support enough system spinning reserve to meet (5.10) and (5.11). The total online spinning reserve is the difference between curves 2 and 1 in Figure 5.12. The hourly total capacity of online units and ESS should be greater than or equal to the sum of total system generation and online spinning reserve, i.e. curve 3 is above curve 2. In this smart power system, curve 4 is not a constant horizontal line as in the conventional power system. One reason is that the available output power of renewable sources changes as ambient conditions change. Another one is that the hourly available energy stored in ESS is not the same every hour.

5.4.2.2 Power Flow and Transformer Tap Ratios

For the SEMS, line power flows need to be controlled when the optimum objective function in (5.6) is obtained. In this case, the AC power flow solution for the last hour (24th hour) is shown in Figure 5.13. The solution is obtained by solving the multi-objective optimization problem using the Jump and Shift method. The bus voltages are also controlled to meet the bus voltage limits by adjusting the injection of reactive power and transformer tap ratios. The voltage and angle at each bus for the last hour are shown in Table 5.3.

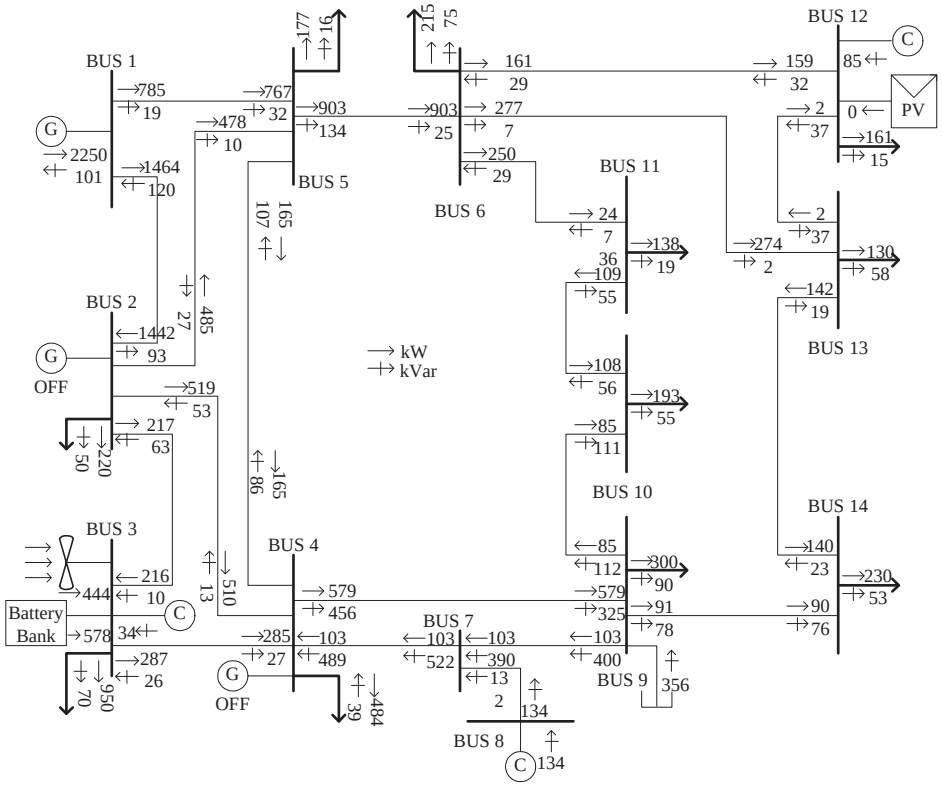

FIGURE 5.13: AC power flow of 14-bus power system at 24th hour

There are three kinds of bus types: Reference (Ref) bus, PV generation bus and PQ load bus. In this case the voltage limits for Ref, PV and PQ buses are 0.99-1.01, 0.96-1.04 and 0.91-1.09, respectively. Comparing these limits with the voltage solution in Table 5.3, it is clear that the bus voltage limits are all enforced.

TABLE 5.3: Bus voltages and angles at 24th hour

Bus #	type #	voltage (pu)	angle ($^\circ$)	Bus #	type #	voltage (pu)	angle ($^\circ$)
1	Ref	1.01	0	8	PV	1.0090	-15.06
2	PV	0.9979	-2.78	9	PQ	1.0199	-14.70
3	PV	0.9952	-4.20	10	PQ	1.0133	-14.81
4	PV	0.9843	-5.79	11	PQ	1.0123	-14.02
5	PQ	0.9833	-5.52	12	PV	1.0153	-13.77
6	PQ	1.0217	-12.40	13	PQ	1.0114	-13.50
7	PQ	0.9960	-15.06	14	PQ	1.0022	-15.16

Three TCUL transformers are used in this case. TCUL 1 is set between buses 4 and 7. TCUL 2 and TCUL 3 are set between buses 4 and 9, 5 and 6, respectively. The transformer tap ratio can be adjusted from 0.85 to 1.15 with a step of 0.05. The three optimum transformer tap ratios are shown in Figure 5.14.

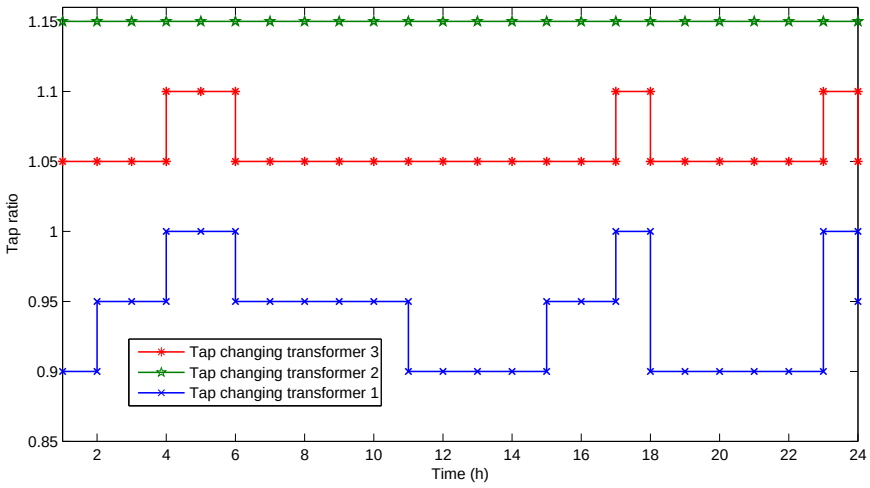

FIGURE 5.14: Transformer tap ratios of 14-bus power system

5.4.2.3 Results Comparison with Those of Typical Solution Method (solving UC and OPF independently and separately)

To compare with the results of the Jump and Shift method based on this 14-bus MG, the typical solution method which solves UC and OPF independently, one after another without passing the UC and OPF results iteratively back and forth is also employed.

For simplification, the power loss is taken as 5% of the real load during the UC problem in the typical solution method. For better comparison, the OPF problem is also set to run for the next 24 hours.

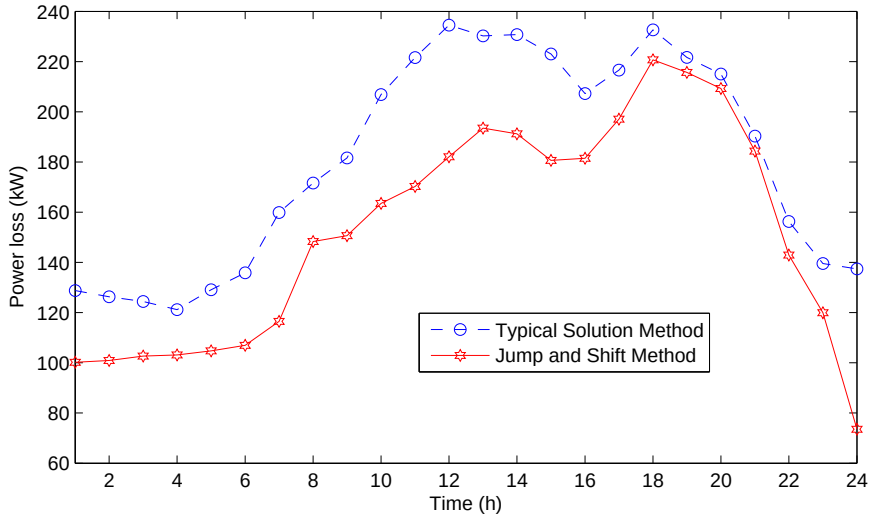

FIGURE 5.15: Loss comparison between typical solution method and Jump and Shift method

The total optimal schedule cost obtained in the typical solution method is \$8,544, whereas it is \$8,457 in the Jump and Shift method. Compared with the typical method, the proposed method reduces about \$87 per day, which is 1.03% of the total optimal schedule cost or \$31,755 on the average per year. The hourly power loss via the typical solution method is higher than the hourly power loss by the Jump and shift method. The comparison of the hourly power loss is also shown in Figure 5.15.

5.4.3 Test Results and Extended Analysis of 112-Bus Power System

For this 112-bus system, the shift factor χ is set at 0.03, the same in the 14-bus MG system. The parameter α for the online spinning reserve is 0.25. The results of the real power of system components and spinning reserve of the 112-bus power system follow the same trends of the 14-bus MG system except that they exhibit larger values. The total output of ESS and the optimal transformer tap ratios are shown in Table 5.4. There are 24 TCUL transformers in the 112-bus power system. Four of them are shown in Table 5.4. TCUL 1 is located between Buses 4 and 7. TCUL 2, TCUL 3 and TCUL

4 are located between buses 18 and 23, buses 46 and 49, buses 89 and 90, respectively. The transformer tap ratio can be adjusted from 0.85 to 1.15 with a step of 0.05 which is the same as that of the 14-bus MG. In the 112-bus power system the total optimal schedule cost is \$54,836 and the total power loss during 24 hours is 29,075 kW.

TABLE 5.4: Total output of ESS and transformer tap ratios in 24 hours

Hour	ESS (kWh)	TCUL1	TCUL2	TCUL3	TCUL4
1	155.6	0.9	1.15	0.9	1.05
2	661.2	0.95	1.15	0.95	1.05
3	383.2	0.95	1.15	0.95	1.05
4	-495.1	1	1.15	1	1.1
5	353.8	1	1.15	1	1.1
6	-1058.8	0.95	1.15	0.95	1.05
7	0	0.95	1.15	0.95	1.05
8	288	0.95	1.15	0.95	1.05
9	-288	0.95	1.15	0.95	1.05
10	0	0.95	1.15	0.95	1.05
11	545.8	0.9	1.15	0.9	1.05
12	608	0.9	1.15	0.9	1.05
Hour	ESS (kWh)	TCUL1	TCUL2	TCUL3	TCUL4
13	809.6	0.9	1.15	0.9	1.05
14	-344.1	0.9	1.15	0.9	1.05
15	0	0.95	1.15	0.95	1.05
16	0	0.95	1.15	0.95	1.05
17	0	1	1.15	1	1.1
18	1200	0.9	1.15	0.9	1.05
19	0	0.9	1.15	0.9	1.05
20	0	0.9	1.15	0.9	1.05
21	0	0.9	1.15	0.9	1.05
22	463.2	0.9	1.15	0.9	1.05
23	916.2	1	1.15	1	1.1
24	4620.6	0.95	1.15	0.95	1.05

5.5 Conclusion

The Jump and Shift method is developed to handle the multi-objective optimization for SEMS in this chapter. It aims to solve a large scale linear/nonlinear programming problem where its constraints are coupled to another large scale linear/nonlinear

programming problem. The shift factor χ is used to speed up the convergence of the iterative solution. The total computing time for the 14-bus MG power system based on the Jump and Shift method running on Intel(R) Core(TM)2 Quad CPU 2.67GHz, 3.25GB of RAM with Linux operating system is only 3.57s, which is acceptable. For the 112-bus power system, the total computing time is 10.5 mins. The computational details for the 14-bus MG and 112-bus power system are shown in Table 5.5.

TABLE 5.5: Computational size of program

Power system	14-bus	112-bus
# of variables	1,464	11,568
# of constraints	2,097	16,776
Computing time	3.57s	10.5mins

The expected goals of system optimization can be achieved by SEMS, which can make optimal use of the sustainable and varied energy sources as part of the smart grid. It is believed that SEMS can make a significant contribution to distributed power generation.

Chapter 6

Sizing of Energy Storage for Microgrids

6.1 Introduction

The MG consists of a group of radial and possibly ring feeders, which could be part of a distribution system. There is a single point of connection to the utility called point of common coupling (PCC). The MG also has microsources consisting of a photovoltaic (PV) system, a wind turbine (WT) system, two microturbines (MTs), a fuel cell (FC), and an energy storage system (ESS), as shown in Figure 1.1. The fuel input is needed only for the MT and FC as the energy input for the WT and PV comes from wind and sun. To serve the load demand, electrical power can be produced directly by MT, FC, PV and/or WT. The upstream power system can also support the power in grid-connected MGs. Furthermore, the central controller, i.e., smart energy management system, is the main control interface between the upstream grid and the MG. The central controller has the main responsibility for optimizing the MG operation, or alternatively, coordinating the actions of local controllers to produce the optimal output.

With renewable energy sources connected online, their integration and control pose more challenges to the operation of power systems. How to mitigate renewable power intermittencies, load mismatches and negative impacts on MG voltage stability are some key problems to be solved. A potential candidate solution to the identified problems is

using ESS to store electrical/renewable energy at the time of surplus and re-dispatch it appropriately later when needed [120].

ESS plays an important role in the MG, which is desirable to shave the peak demand and store the surplus electrical/renewable energy [121]. Sizing of ESS is to be considered first when considering ESS in the MG. Much research works have been done to address this question. Battery storage is being used in conjunction with renewable energy resources, i.e., solar and wind, as it provides a means of converting these non-dispatchable and highly variable resources into dispatchable ones [122],[59],[123]. ESS could also increase the reliability of power systems [124]. The sizing problem of the ESS for customers of time-of-use (TOU) rates has been addressed in [125]. References [126] and [127] introduced the ESS sizing problem for only one kind of renewable energy to cover the peak load requirement.

This chapter focuses on determining the size of ESS for MGs. It aims to find the optimal size of ESS for MGs by formulating it in the unit commitment problem both in the islanded and grid-connected modes of MGs. It also tries to find the relationship between the size of ESS and the total cost of the MG. Considering the daily cycle of the solar and wind pattern in Singapore, ESS will also follow the same charge and discharge cycle everyday. Typical results will be obtained based on the case study of a chosen day. Most MGs operate in the grid-connected mode. However, islanded MGs are also built for isolated islands or remote places. That is why both the grid-connected and islanded modes of MGs are considered.

For grid-connected MGs, the upstream grid can supply power to the MG during the peak load period. The extra power generated by renewable energy resources during the low load period can be sold back to the upstream grid. Market prices need to be considered in this mode and the objective function is to maximize the market profit. In the islanded mode, the MG must cover the power balance by itself. ESS is used to store the extra power generated by renewable energy resources during the low load period and re-dispatch it during the peak load period. The objective function is to minimize the total cost.

6.2 Problem Formulation

6.2.1 Islanded Microgrids

6.2.1.1 Minimum Size of Battery Energy Storage System

When BESS is installed, one also needs to consider the minimum size for $BESS$ needed by islanded MGs. Sizing a suitable battery bank, in terms of its power and energy rating, not only could help in shaving the peak demand but also for storing the excess renewable energy and supplying the load when the renewable energy is low. The amount of peak power shaving should be associated with the marginal cost of generating or importing electricity during the specified peak hours while the cost of the battery system is largely associated with its energy storage rating (kWh) rather than the power rating (kW) [123]. Hence a small discharge period is desired if it is possible [97]. Once the peak shaving is established, then the minimum energy supplied by $BESS$ is defined as:

$$E_{dis}^{min} = \int_0^T (P_{load}^t - P_{grid}^{t,max})\delta t, \quad P_{load}^t \geq P_{grid}^{t,max} \tag{6.1}$$

where T is the end of the time period set, which is one day; δt is the time interval, which is one hour in this chapter; P_{load}^t is the system load at time t; P_{grid}^t includes the power from both the renewable energy and traditional energy at time t; and $P_{grid}^{t,max}$ is the maximum power supplied by all the generators in a smart power system.

For a smart power system, renewable energy resources are supposed to supply electric power to the grid as much as they could. This means that renewable energy resources are kept on all the time if conditions permit. When the power supplied by renewable energy resources is more than the load in the system, it will be used to charge up the $BESS$. Then the minimum energy charged to $BESS$ is defined as:

$$E_{charge}^{min} = \int_0^T (P_{grid}^{t,min} - P_{load}^t)\delta t, \quad P_{grid}^{t,min} \geq P_{load}^t \tag{6.2}$$

where $P_{grid}^{t,min}$ represents the minimum power supplied by the renewable energy sources in the smart power system.

Finally the minimum value of $BESS$ energy storage rating E^{min}_{BESS} can be obtained in (6.3).

$$E^{min}_{BESS} = max(\frac{E^{min}_{dis}}{\eta_d}, \eta_c E^{min}_{charge}) \tag{6.3}$$

where η_d and η_c are the discharge efficiency and charge efficiency respectively. $\frac{E^{min}_{dis}}{\eta_d}$ and $\eta_c E^{min}_{charge}$ are the minimum discharge energy and charge energy of the battery bank.

6.2.1.2 Unit Commitment with Renewable Energy and Energy Storage System

The UC schedule is a complex challenging problem, especially when renewable energy resources and energy storage system are included. The solution method determines the set of committed generators to meet each hourly forecasted load over a specific study period. The UC schedule problem is constrained by the hourly minimum spinning reserves, generator start up/down times, ramp rates and network security [103].

The formulation is as follows:

Minimize the total UC schedule cost ($TUCC$),

$$\begin{aligned} &\textstyle\sum_t \sum_{n\in CG}(r_n R_{tn} + d_n SU_{tn} + U_{tn}(a_n + b_n P_{tn})) \\ &\quad + \textstyle\sum_t \sum_{n\in WG}(U_{tn} P_{tn} c_w) \\ &\quad + \textstyle\sum_t \sum_{n\in PG}(U_{tn} P_{tn} c_{pv}) \end{aligned} \tag{6.4}$$

where CG is a set of dispatchable distributed generators, which includes microturbines and fuel cell systems; WG and PG are sets of wind energy and PV renewable resources respectively; n and t are subscripts indicating generator/energy resource and hour index respectively; a_n and b_n are the cost coefficients of microturbines and fuel cell systems; U_{tn} and SU_{tn} are vectors of binary integers representing unit status and start up status; r_n and d_n are the reserve cost and start up cost respectively; P_{tn} is the generator output power; R_{tn} is the spinning reserve of dispatchable distributed generators; and c_w and c_{pv} are the wind and PV energy cost respectively.

Spinning reserve is the term used to describe the total amount of generation available from all units synchronized in the system, after subtracting the present load and losses

being supplied and addup the available energy storage in ESS. The unit commitment problem may involve various classes of scheduled reserves or off-line reserves.

To solve the problem in (6.4), one needs to consider the following constraints:

Real power balance,

$$\begin{aligned} &\textstyle\sum_{n\in CG} P_{tn} + \sum_{n\in WG} P_{tn} + \sum_{n\in PG} P_{tn} \\ &\qquad + \textstyle\sum_{n\in ES} P_{tn} = \sum_i PD_{ti} + PL_t \end{aligned} \qquad \forall t \tag{6.5}$$

ES is a set of energy storage system; PD_{ti} is the power demand at the ith bus in time period t; and PL_t is the distribution line loss in time period t.

The ESS model is introduced in Chapter 2.5, which is considered as a generator here. When ESS discharges its energy to the power grid, it is generating positive real power. When ESS absorbs energy from the power grid, it is treated as generating negative real power. The constraints for ESS are also considered here.

Unit spinning reserve capacity:

$$R_{tn} \leq min\{R10_n * U_{tn}, \quad P_n^{max} * U_{tn} - P_{tn}\} \forall t, n \in CG \tag{6.6}$$

where $R10_n$ is the 10-min reserve capacity.

Capacity of largest online generator:

$$CR_t \geq P_n \qquad \forall t, n \in CG \tag{6.7}$$

where CR_t is the hourly required spinning reserve capacity for the system.

The system reserve criteria are shown in the following two constraints in (6.8)-(6.9). The ESS and renewable energy forecasting error are both considered in these two criteria.

System spinning reserve:

$$\begin{aligned} &\textstyle\sum_{n\in CG} R_{tn} + \sum_{n\in ES} \eta_d (C_{n,t} - C_{min}) \geq \\ &\qquad \alpha * CR_t + RMSE \textstyle\sum_{n\in WG} P_n^w \\ &\qquad + MAPE \textstyle\sum_{n\in PG} P_{tn} + \kappa \sum_i PD_{ti} \end{aligned} \qquad \forall t \tag{6.8}$$

System 10-min operating reserve:

$$\begin{aligned} &\textstyle\sum_{n\in CG} R_{tn} + \sum_{n\in G10}(1-U_{tn}) * P10_n \\ &\quad + \textstyle\sum_{n\in ES} \eta_d (C_{n,t} - C_{min}) \geq \\ &\qquad CR_t + RMSE \textstyle\sum_{n\in WG} P_n^w + \\ &\qquad MAPE \textstyle\sum_{n\in PG} P_{tn} + \kappa \sum_i PD_{ti} \end{aligned} \qquad \forall t \qquad (6.9)$$

where $P10$ is the reserve contribution of the 10-min quick start units ($G10$); CR_t is the minimum spinning reserve requirement; κ is the load forecast error factor; α is the factor of hourly spinning reserve to be maintained online; and $C_{n,t}$ is the available energy stored in the nth ESS at time period t.

Meanwhile the generator output limits, ramp rate limits and minimum up/down time limits are also considered in this problem. For pollution-free and energy sustainability, the renewable energy is always assumed on.

6.2.2 Grid-Connected Microgrids

Consumers are assumed to be charged at the open market prices for grid-connected MGs. The optimization problem is formulated according to the assumed market policy, which is to maximize the profit from the energy consumed. The profit can be considered as revenue minus expenses. Revenue is described as the energy supplied to the consumers multiplied by the electrical price. Expenses include the cost of the energy bought from the upstream grid and the total UC schedule cost.

For grid-connected MGs, the upstream grid can be treated as a bi-directional generator, which can generate positive power when the power is transferred from the upstream grid to the MG and negative power when the power is transferred from the MG to the upstream grid. The output of this bi-directional generator is limited by the capacity of the transmission line between the MG and the upstream grid. With this consideration, the minimum BESS size of a grid-connected MG can be obtained via the approach described in section 6.2.1.1. The set of dispatchable generators CG will be extended to include this bi-directional generator for the grid-connected MG.

Considering the market price for the grid-connected MG, the maximum market benefit (MB) can be formulated in (6.10),

$$\begin{aligned} &Maximize: \\ &MB = \textstyle\sum_t (MP_t \sum_{n \in CG} P_{tn}) - TUCC \end{aligned} \tag{6.10}$$

where MP_t is the market price; $TUCC$ includes the dispatchable generator costs such as start-up cost, online spinning reserve cost and generating energy cost and renewable energy cost such as wind and PV energy cost.

The same constraints used in the islanded MG could also be considered for the problem in (6.10).

6.2.3 Solution Algorithm

Considering $TCPD$ of BESS introduced in section 2.5 for both the islanded and grid-connected MGs, the objective function will change to minimizing the total cost (TC) in (6.11) for the islanded MG and maximizing the total benefit (TB) in (6.12) for the grid-connected MG.

$$TC = TCPD + TUCC \tag{6.11}$$

$$TB = MB - TCPD \tag{6.12}$$

To obtain the optimal size of BESS, the main problem is to minimize TC in (6.11) for the islanded MG or maximize TB in (6.12) for the grid-connected MG. Figure 6.1 shows the algorithm developed in this chapter which is used to solve the optimal size of BESS. This algorithm will compute the different costs under different sizes of BESS between minimum size CE_{min} and maximum size CE_{max}. The optimal size can then be found at the minimum cost point of (6.11) for the islanded MG or maximum benefit point of (6.12) for the grid-connected MG.

The proposed solution is a mixed-integer linear problem. This algorithm is implemented in AMPL with CPLEX, a mixed-integer linear solver [88], and the results are double checked with another solver KNITRO. They proved to be the same values. The detail of this algorithm is as follows:

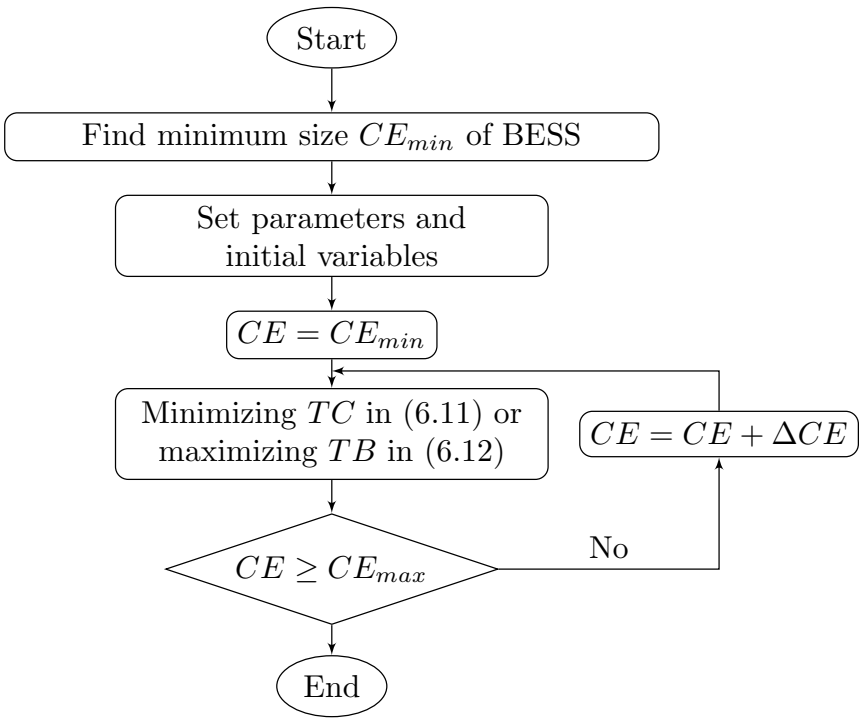

FIGURE 6.1: Algorithm used to solve optimal BESS capacity

1. Enter the forecasting renewable power and load. Calculate the minimum capacity CE_{min} of BESS.

2. Set CE_{max}, which is relatively large for the MG, ΔCE and the unit and system parameters. Initialize the variables.

3. Solve the objective function for CE, which is the size of BESS. Minimize the total cost in (6.11) for the islanded MGs or maximize the total benefit in (6.12) for the grid-connected MG.

4. If $CE < CE_{max}$, update CE using $CE = CE + \Delta CE$ and go to step 3. The algorithm will stop when $CE \geq CE_{max}$.

6.3 Cost-Benefit Analysis - Case Studies

These case studies attempt to determine the optimal BESS ratings for the MG which is shown in Figure 1.1. Forecasting techniques based on the time series method and FNN

is used to obtain the forecast wind speed and solar radiation of a chosen day separately. Their forecasted errors are also considered. An energy storage system may have different behaviors under different operating modes of MGs. Two scenarios are introduced here. The optimal BESS capacity problem of the grid-connected mode is addressed in scenario one while that of the islanded mode is considered in scenario two.

The parameters of the wind generator are: $P_R = 1000kW$, $V_c = 3m/s$, $V_R = 12m/s$, and $V_F = 30m/s$. The parameters of the PV source are: $\eta = 15.7\%$ and $S = 7000m^2$. The forecast wind speed and solar radiation is shown in Figure 2.2 and Figure 2.8 respectively. Then the output of the wind generator can be obtained by (2.7) and the PV power is calculated by (2.8). They are shown in Figure 6.2. The forecast load is also shown in Figure 6.2. The load forecast error factor κ is assumed at 3% [128]. The renewable power curve is the total power supplied by the PV and wind generator. There are two MTs and one FC in this microgrid and the details are shown in Table 6.1, where MT is the microturbine and FC is the fuel cell unit.

TABLE 6.1: Distributed generator data

Gen #	*Type*	a ($)	b ($/kW$)	P_n^{min} (kW)	P_n^{max} (kW)	d ($/start)
1	MT	30	0.13	100	2000	150
2	MT	50	0.35	100	1000	30
3	FC	80	0.50	100	1000	30

Gen #	r ($/kW$)	UT (hrs)	DT (hrs)	IC (hrs)	P10 (kW)	R10 (kW)
1	0.010	2	2	2	0	2000
2	0.010	0	0	-1	1000	1000
3	0.010	0	0	-1	1000	1000

The interest rate r for financing the installed BESS is set at 6%. From [129], the cost for BESS of 100 kWh is about $60,000 and it will drop very fast when the BESS technology is widely adopted in the future. The maintenance cost for this BESS is $2,000. The lifetime of BESS is set to three years. For this MG system, the maximum capacity is 2,900 kWh and the charge efficiency and discharge efficiency are the same and set at 90%. The maximum charge and discharge power rates are set as 50% of its full capacity, which means that BESS can be fully charged or discharged in two hours [130]. The

parameter α for the spinning reserve capacity factor can be as low as 0.25 [119] and is set to 0.8 in this chapter.

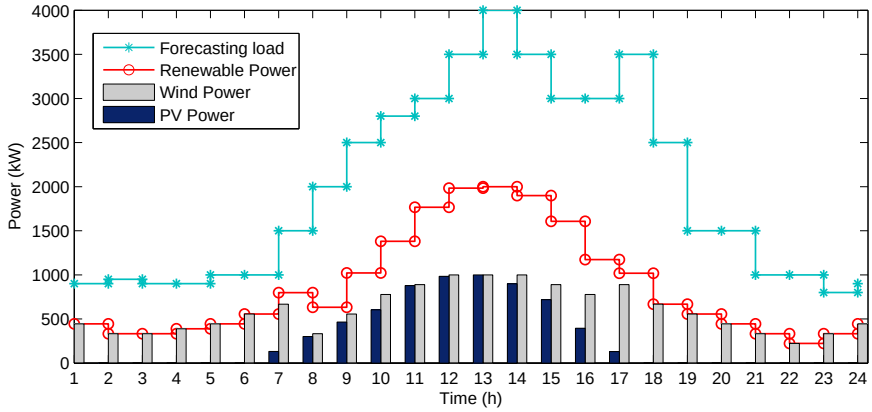

FIGURE 6.2: Forecast load, PV power and wind power

6.3.1 Scenario One

The MG is connected with the upstream power grid in this scenario, which means that it can buy power from the power market during the peak load period and sell power to the power market during the valley load period. The upstream grid can also support system reserve for the MG. The limit of the power transfer between the MG and the upstream grid is set at 1000 kW. The market price is shown in in Table 6.2.

As discussed before, the cost of BESS ($TCPD$) increases with a larger size, which is shown in Figure 6.3, the increment for the cost of BESS is \$67 per 100 kWh in one day. Meanwhile, as shown in Figure 6.3. The market benefit (MB) obtained in (6.10) also increases with a larger size of BESS. The benefit of increasing investment on BESS is to increase the market benefit (MB), but there is a trade-off between the benefit and the investment cost in this case. When the increment for MB and the cost increment of BESS have the same value, the optimal size of BESS may be found. This relationship is shown in Figure 6.3. The total benefit (TB) includes the cost of BESS and market benefit. As shown in Figure 6.3. The maximum value of TB is obtained at \$10,990 when the size of BESS is 500 kWh.

Considering this system without BESS, TB will be \$10,774. In this grid-connected MG, the minimum size of BESS is obtained as zero, which means that there is no need to

TABLE 6.2: Market prices of upstream power system

Hour	Price $/kWh	Hour	Price $/kWh
1	0.11	13	0.50
2	0.10	14	0.40
3	0.11	15	0.30
4	0.09	16	0.30
5	0.11	17	0.40
6	0.11	18	0.50
7	0.13	19	0.30
8	0.15	20	0.26
9	0.26	21	0.15
10	0.30	22	0.13
11	0.35	23	0.10
12	0.40	24	0.11

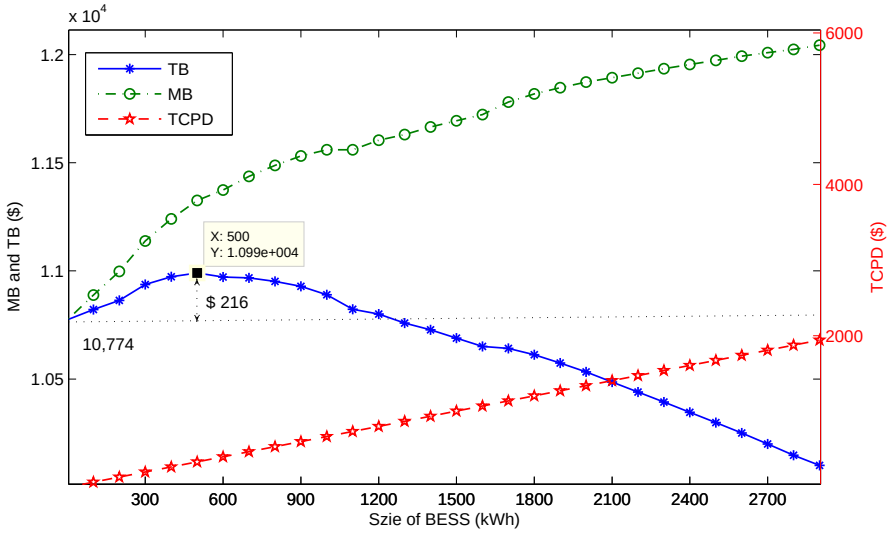

FIGURE 6.3: Benefit in one day for different size of BESS in scenario one

install BESS in this MG if TB does not increase after installing it. From Figure 6.3, TB is less than \$10,774 when the size of BESS is greater than 1200 kWh and it is greater than \$10,774 when the size of BESS is less than 1200 kWh. Hence, the range of the available size for BESS in this grid-connected MG is from 0 to 1200 kWh. This is because TB is higher than that without BESS installed when the size of BESS is between 0 and 1200 kWh. The maximum increment point of TB will also be the point of the maximum size for BESS. It is 500 kWh and the maximum increment of TB is

$216 in one day.

TABLE 6.3: Schedule of dispatchable generators when 500 kWh BESS is installed for MG in scenario one

Hour	MT1	MT2	FC	Hour	MT1	MT2	FC
1	$1 \to 0$	$0 \to 0$	$0 \to 0$	13	$1 \to 1$	$1 \to 1$	$0 \to 0$
2	$1 \to 0$	$0 \to 0$	$0 \to 0$	14	$1 \to 1$	$1 \to 1$	$0 \to 0$
3	$1 \to 0$	$0 \to 0$	$0 \to 0$	15	$1 \to 1$	$1 \to 0$	$0 \to 0$
4	$1 \to 0$	$0 \to 0$	$0 \to 0$	16	$1 \to 1$	$1 \to 1$	$0 \to 0$
5	$1 \to 0$	$0 \to 0$	$0 \to 0$	17	$1 \to 1$	$1 \to 1$	$1 \to 0$
6	$1 \to 0$	$0 \to 0$	$0 \to 0$	18	$1 \to 1$	$1 \to 1$	$0 \to 0$
7	$1 \to 0$	$0 \to 0$	$0 \to 0$	19	$1 \to 1$	$0 \to 0$	$0 \to 0$
8	$1 \to 1$	$0 \to 0$	$0 \to 0$	20	$1 \to 1$	$0 \to 0$	$0 \to 0$
9	$1 \to 1$	$1 \to 0$	$0 \to 0$	21	$1 \to 1$	$0 \to 0$	$0 \to 0$
10	$1 \to 1$	$1 \to 0$	$0 \to 0$	22	$1 \to 1$	$0 \to 0$	$0 \to 0$
11	$1 \to 1$	$1 \to 0$	$0 \to 0$	23	$1 \to 0$	$0 \to 0$	$0 \to 0$
12	$1 \to 1$	$1 \to 1$	$0 \to 0$	24	$0 \to 0$	$0 \to 0$	$0 \to 0$

The schedule of dispatchable generators when 500 kWh BESS is installed for the MG is shown in Table 6.3. With the help of the optimal size of BESS, the dispatchable generators can be shut down during some time periods to save cost under the same system constraints. The outputs of dispatchable generators and the power transfer between the upstream gird and the MG are shown in Figure 6.4. In the grid connected MG, it can buy power from the upstream gird during the low price period and sell power to the upstream grid during the high price period, which is also shown in Figure 6.4 for both the MGs without BESS and with BESS of 500 kWh.

From Figure 6.4. one can tell that the small output of dispatchable generators can be shifted to the upstream grid or the biggest generator due to the presence of BESS. MT #1 is shut down in the first seven hours when BESS of 500 kWh is installed in the MG. The output of MT #1 is covered by buying more power from the upstream grid due to its low market price in the first six hours. BESS can supply the spinning reserve which was previously supplied by MT #1 during these hours in the MG without BESS. In the 7th hour, the ouput of MT #1 is not fully covered by the increment of power from the upstream grid. The difference can be found in BESS, which is shown in Figure 6.5. BESS discharges 104.6 kWh to the MG in the 7th hour. Considering the charge efficiency of BESS, the MG can get 94.1 kWh from BESS, which is exactly the difference between the two power outputs of the MG with/without BESS at the 7th hour in Figure

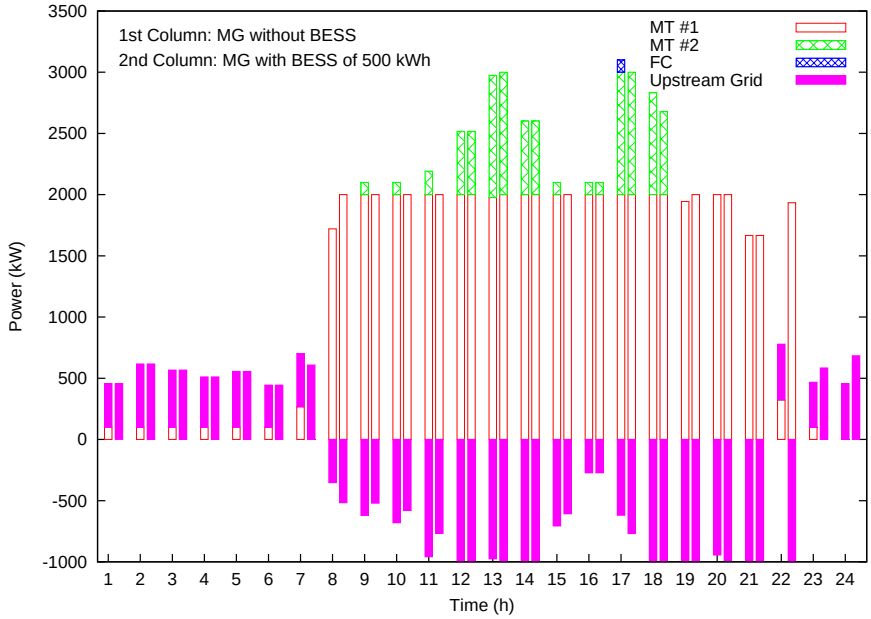

FIGURE 6.4: Comparison of dispatchable generator outputs between MG without BESS and MG with BESS of optimal size in scenario one

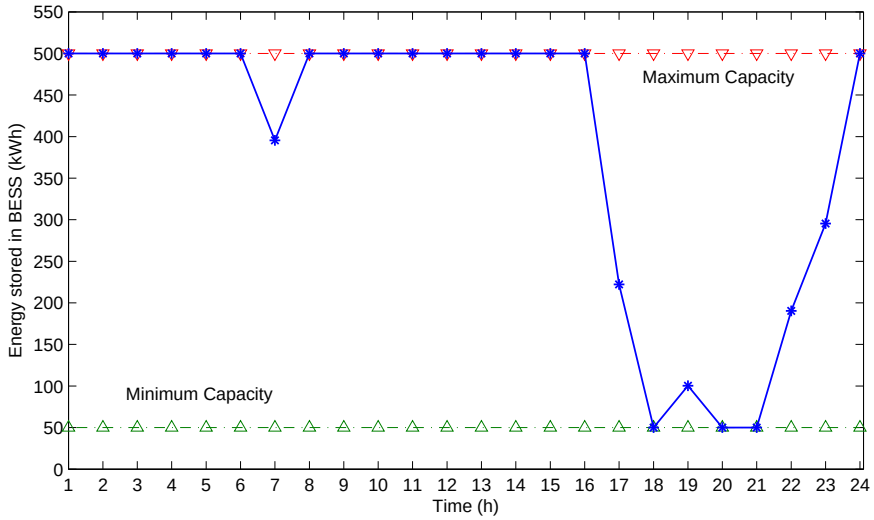

FIGURE 6.5: Energy stored in BESS at optimal size in scenario one

6.4. The same thing happens to MT #2 and FC. MT #2 is shut down at the 9th, 10th, 11th, and 15th hour and FC is shut down at the 17th hour. The output of MT #1 is increased at the 8th, 19th, and 22th hours to cover the changes from the upstream grid and BESS.

Figure 6.5 shows the energy stored in BESS. For an effective comparison with different BESS sizes, the starting and ending limits of BESS in this chapter are set as the full capacity of BESS. This will make sure that BESS only balances the power in the MG and it does not supply/absorb the extra energy to/from the MG. The minimum capacity is set at 10% of the full capacity and the maximum capacity is the full capacity of BESS, which are 50 and 500 kWh, respectively. The energy stored in BESS is within these limits and it supplies power to the MG during the peak load period. For most time during these 24 hours, the energy stored in BESS is unchanged, which means the BESS does not charge or discharge frequently. Considering the charge and discharge efficiencies, the process will waste energy during every charge or discharge cycle. Hence, when necessary BESS only discharges energy to the MG during peak load period and is charged up during the low market price period, which are reflected in the results shown in Figure 6.5. The energy stored in BESS will remain unchanged for the remaining time.

Beside covering the power output of the dispatchable generators, BESS also supports the MG as a source of spinning reserve. It will help to reduce the cost of spinning reserve generated by dispatchable distributed generators. The forecast error of renewable energy is considered in both the spinning reserve and 10-min operating reserve constraints. The reserve requirement will vary hourly and BESS will attempt to balance this variation.

6.3.2 Scenario Two

A MG in islanded mode is considered in this scenario. The data for dispatchable distributed generator, renewable energy resources and forecasted load is the same as that in scenario one. Unlike grid-connected MGs, the islanded MG needs to meet all the constraints in (6.5)-(6.9) without any external help. Besides, a minimum size of BESS requirement needs to be considered in the islanded MG. The minimum size of BESS is obtained at 0 kWh.

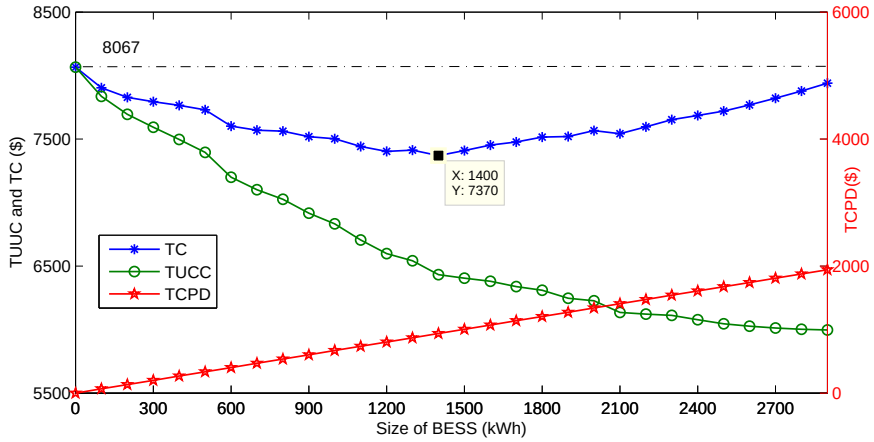

FIGURE 6.6: Cost in one day of different size of BESS in scenario two

The cost of different sizes of BESS is shown in Figure 6.6. $TCPD$ is the same as that in scenario one. It increases as the BESS size increases. The total UC operating cost ($TUCC$) reduces when the size of BESS increases, which is shown in Figure 6.6. However, the decrement of $TUCC$ is getting smaller and smaller when the size of BESS is greater than 1400 kWh. TC includes $TCPD$ and $TUCC$, and its optimal value is obtained by a trade-off between $TUCC$ and $TCPD$. From Figure 6.6, TC reduces when the size of BESS is small and increases when the size of BESS is greater than 1400 kWh. Hence, the optimal size of BESS can be found at 1400 kWh where TC is the minimum value at \$7,370. The maximum value of TC is \$8,067 at zero kWh of BESS installation.

The outputs of dispatchable generators in both the MG without BESS and the MG with BESS of optimal size are shown in Figure 6.7. The corresponding energy stored in BESS is shown in Figure 6.8. The start and end limits of energy storage are the same as those of scenario one, which are the full capacity of BESS. The minimum capacity of BESS is also set at 10% of its full capacity and the maximum capacity is its full capacity, which are 140 kWh and 1400 kWh, respectively.

The behaviors of the dispatchable generators are very similar to those of the grid-connected MG. MT #2 shuts down during the 8th-12th, 14th, 15th, and 20th hours and the outputs during these hours are shifted to the cheapest generator, MT #1, and BESS. It also happens for FC during the 13th, and 16th-18th hours.

In Figure 6.8, the energy stored in BESS remains unchanged for most of the time because of the charge and discharge efficiencies. BESS also serves as a source of online reserve,

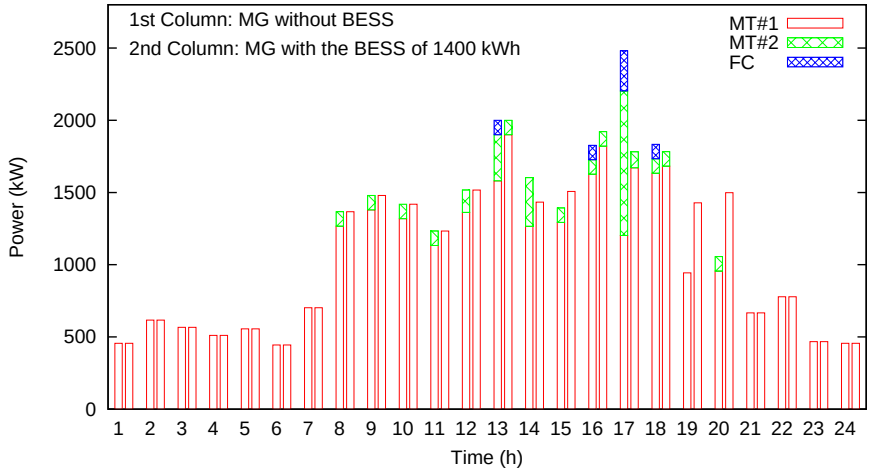

FIGURE 6.7: Comparison of dispatchable generator outputs between MG without BESS and MG with BESS of optimal size in scenario two

which is the same as in scenario one. One also can easily find that the system attempts to maintain BESS at its full capacity, which means that BESS will get charged up as soon as possible after it has discharged. For example, BESS is fully charged within 2 hours after 18:00 in Figure 6.8. This is because the upstream grid is not considered in this islanded MG. BESS does not need to wait to charge up its energy when the market price is cheap. BESS maintained at its full capacity will help to carry a higher spinning reserve share, which will lower $TUCC$.

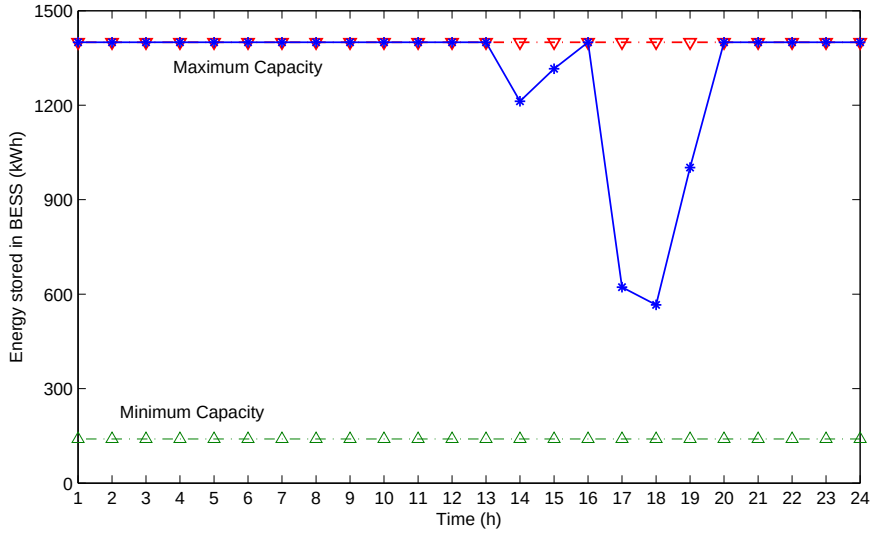

FIGURE 6.8: Energy stored in BESS at optimal size in scenario two

The lowest energy stored in BESS is 566 kWh in the 18th hour in Figure 6.8. It covers the spinning reserve which is contributed by MT #1 when BESS is not installed. The lowest energy stored in BESS is much higher than that of scenario one. This is because the upstream power grid can support the same MG as a source of spinning reserve, which could lower the optimal size of BESS. Whether or not BESS would discharge partially/fully its stored energy in the 18th hour or other hours very much depends on the co-optimization between the energy and reserve.

6.4 Conclusion

The problem of determining the optimal BESS size can be solved by the method presented. This method is tested using the forecast data over a day in a MG shown in Figure 1.1. Time series and FNN techniques are used for forecasting the wind speed and solar radiation respectively. The errors associated with forecasting wind speed, PV radiation and system load are also considered in this Chapter. The proposed approach employs a cost-benefit analytical technique to estimate the economic feasibility of the BESS deployment for both the grid-connected and islanded modes. Based on the results obtained the following points can be concluded.

Firstly, the quantitative results of the case study in both scenarios show that BESS for the MG could increase the benefit of the MG, i.e., increase MB in scenario one, or decrease the schedule cost of the MG, i.e., decrease $TUCC$ in scenario two. As the size of BESS increases, the benefit increases or the cost decreases. However, the rate of the increment of benefit or the rate of the decrement of cost is getting smaller and smaller. Considering that the $TCPD$ increases in a constant rate and when the size of BESS is greater than some optimal BESS value, the total benefit TB in scenario one will reduce and the total cost TC in scenario two will increase as shown in Figure 6.3 and Figure 6.6 respectively. Hence, the optimal size of BESS exists and differs in both the grid-connected and islanded MGs.

Secondly, the decrement of $TUCC$ includes two components in scenario two. The first component is that BESS can store the surplus renewable energy and re-dispatch it appropriately. This could smoothen the intermittent power supplied by distributed renewable resources, which could make the generators operate at a stable condition and

lower their cost by reducing the shutdown and startup frequency. The intermittency of the renewable energy and load is somewhat represented by their hourly average integrated energy forecast errors. BESS could be considered as a fast unit which participates in frequency regulation to compensate the forecast deficiency and to drive the real-time area control error (ACE) to zero. The second component is that energy stored in BESS can be considered as a form of reserve to help the MG meet the reserve constraints, which will reduce the reserve cost of the MG. These two components also increase MB in scenario one. Besides, the BESS in scenario one can store energy when the market price is low and re-dispatch it during the peak load period. This helps to increase MB.

Thirdly, from the results of scenarios one and two, one can easily say that installing BESS with optimal size could increase TB for the grid-connected MG and reduce TC for the islanded MG. Comparing with the grid-connected MG without BESS, installing an optimal size of 400 kWh BESS will increase TB about 2% per day in scenario one. Comparing with the islanded MG without BESS, installing an optimal size of 1400 kWh BESS will reduce TC about 8.64% per day in scenario two. The charging and discharging efficiency of BESS is considered. With the charging and discharging rates, the optimal solution will also minimize the frequency of charging or discharging for BESS. This will increase the operating life of batteries.

Chapter 7

Online Energy Management System for Lithium-ion Battery

7.1 Introduction

In recent years, several approaches on energy storage for power systems have been studied intensely. Reference [131] describes the use of battery energy storage systems (ESS) in wind generation schemes. ESS has been discussed in Chapter 6. The online management energy system of ESS is needed to detect the energy level and help to control the charging or discharging process of ESS.

There are many forms of ESS, such as batteries, super-capacitors, compressed air energy storage, pumped storage and superconducting magnetic energy storage systems. Selection of suitable ESS is governed by several factors, including consideration on capacity, relative maturity of technology, cost, safety, environmental concern and performance. Lithium-ion (Li-ion) batteries are suitable for ESS and are chosen in this chapter because of their high energy densities, long endurance time and easy implementation and maintenance [33], [57], [132]. They are increasingly being used in systems such as electric vehicles, portable electronics, space and aircraft power systems [129], [133]. The lithium ions move from the anode to the cathode during discharge and move from the cathode to the anode when charging.

The energy capability of the Li-ion battery depends on several parameters, such as charging or discharging current, temperature, voltage and age, which can be represented by state of discharge (SOC) [134]. The SOC is the relative amount of the present charge in comparison with the maximum possible amount. It depends on the battery type and applications [135] and cannot be obtained easily. Indirect and direct methods are used for the SOC estimation. Measuring open circuit voltage (OCV) is one of the indirect methods. Using this method, the battery needs to be open circuit and not connected for some time [136], which is not suitable for the online energy management system of Li-ion batteries. Another indirect method measures the online terminal voltage and checks the look-up table to find out the SOC [137], which could be used in online applications. However, the accuracy is very low. For direct methods, ampere-hour counting is the key technique. It needs the correct initial SOC and an accurate current meter [138]. The accurate SOC cannot be guaranteed when there is some error in the initial SOC or the current measurement.

This chapter proposes an online management energy system for Li-ion batteries. It combines the indirect and direct methods. The relationship between online terminal voltage and the SOC, i.e., an indirect method, is included in the proposed mathematical model of the Li-ion battery. The SOC is also updated by the ampere-hour counting technique, i.e., a direct method, with a proper discharging or charging efficiency. Two internal resistors are defined to address the effect of polarization and change of environment temperature of the Li-ion battery respectively. The age issue is also considered inside the mathematical model. To deal with the errors of the initial SOC and the measurement voltage and current, the adaptive Extended Kalman Filter (EKF) algorithm is employed and the SOC is considered as the state variable for the charging or discharging process of the Li-ion battery. The covariance parameters of the processing noise and observation errors are updated adaptively.

7.2 Modeling of Lithium-ion Battery and Adaptive Extended Kalman Filter

7.2.1 Modeling of Lithium-ion Battery

7.2.1.1 Discharging model

The approach used here begins with the experimental data obtained from a ULTRALIFE UBBL10 lithium-ion battery. The data is expressed in terms of battery terminal voltage curves during various constant discharge current levels and at different constant operating temperatures.

To describe adequately the behavior of the battery under these operating conditions, the battery model has two components: An equilibrium potential E and an equivalent internal resistance R_{int}, which has two sub-components, R_1 and R_2. The electrical schematic of these components is shown in Figure 7.1. The roles of these components and the mathematical relations that describe each component will be explained.

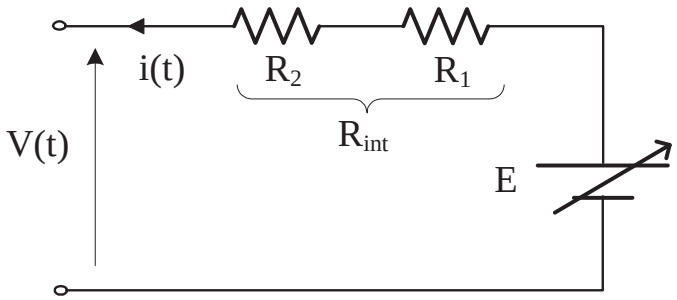

FIGURE 7.1: Equivalent circuit representation of lithium-ion battery

The equilibrium potential of the battery depends on the temperature and the amount of available active electrode material. This can be specified in terms of SOC of the battery. In fact, the discharge capacity of the battery generally depends on the discharge current and temperature too. Thus it is necessary to seek for a general expression for the potential $E(t, T(t), i(t))$, where $T(t)$ is the battery temperature, and $i(t)$ is the discharge current of the lithium-ion battery.

In view of the above, one can model the equilibrium potential $E(t, T(t), i(t))$ based on experimental data. Firstly, choose a typical battery voltage versus SOC curve arbitrarily as a reference curve. The terminal voltage $V(SOC)$ is then expressed in terms of the battery SOC in an nth order polynomial $g(SOC)$. Also, from Figure 7.1, the equilibrium potential $E(t, T(t), i(t))$ is also seen as a function of $V(SOC)$ and current $i(t)$. Secondly, the discharge rate and temperature corresponding to the reference curve are treated as the reference discharge rate and temperature.

Therefore in view of the above, expressions for $E(t, T(t), i(t))$, $V(SOC)$, SOC and R_{int} are

$$\begin{aligned} R_{int} &= R_1 + R_2 \\ SOC &= 1 - \tfrac{1}{\eta_d C} \int_0^t i(t)\delta t \\ V(SOC) &= g(SOC) \\ E(t, T(t), i(t)) &= V(SOC) + R_{int} i(t) \end{aligned} \tag{7.1}$$

where, C and η_d are the capacity and discharging efficiency of the lithium-ion battery respectively.

Normally, the internal resistance R_{int} will increase with the state of discharge as time increases. In this model, R_{int} has two components R_1 and R_2. R_1 is defined as the internal resistance of the Li-ion battery at $SOC = 100\%$, which is due to the polarization of Li-ion battery [135]. It depends on the discharge condition, i.e., temperature, and current level. A voltage drop will be caused by R_1 at the beginning of the discharge process, which is shown in Figure 7.2. R_2 is the resistance due to the change of the ambient temperature. R_2 can also be affected by SOC. It is proposed that an nth-order polynomial is used instead to describe the relationship between R_2 and SOC. A correction factor, $\alpha(T)$ will then be used later to compensate for variation of R_2 with T.

R_1 can be defined as a function of discharge current, temperature and lifecycle l, as follows:

$$R_1 = g_1(i(t), T(t), l) \tag{7.2}$$

Taking derivative on the both sides of (7.2),

$$\delta R_1 = \frac{\partial g_1}{\partial i}\delta i + \frac{\partial g_1}{\partial T}\delta T + \frac{\partial g_1}{\partial l}\delta l \tag{7.3}$$

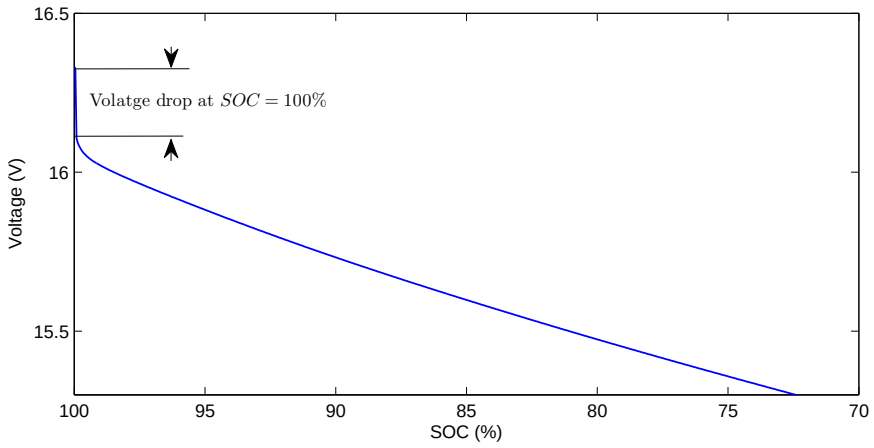

FIGURE 7.2: Battery voltage drop at beginning of discharging

R_1 can be calculated by dividing the initial voltage drop shown in Figure 7.2 by the discharge current $i(t)$ at $SOC = 100\%$. Hence, $\frac{\partial g_1}{\partial i}$, $\frac{\partial g_1}{\partial T}$ and $\frac{\partial g_1}{\partial l}$ can be calculated using the least square method with the help of δR_1, δi, $\delta T$and δl. Then the function of R_1 can be obtained as

$$\begin{aligned} R_1(i,T) = \tfrac{\partial g_1}{\partial i}(i - i^{ref}) + \tfrac{\partial g_1}{\partial T}(T - T^{ref}) \\ + \tfrac{\partial g_1}{\partial T}(l - l^{ref}) + R_1^{ref} \end{aligned} \tag{7.4}$$

where i^{ref}, T^{ref} and l^{ref} are the discharge current, temperature and lifecycle of the reference condition. R_1^{ref} is the internal resistance of the battery under the reference condition at $SOC = 100\%$.

In general, R_2 can be defined as a function of SOC and temperature as follows,

$$R_2 = g_2(T(t), SOC) \tag{7.5}$$

Choose another temperature discharge curve which is under the reference discharge current. Then the voltage drop, the difference between the chosen curve and reference curve at the same SOC, can be defined as $I * R_2^{ref}$, where I is the reference discharge current. The method to determine R_2^{ref} is illustrated in Figure 7.3, where the experimental data from the Li-ion battery is used. The reference curve and another curve at $-20°C$ are chosen to calculate the voltage drop $I * R_2^{ref}$. It is then divided by the reference discharge current I. Next an nth-order polynomial can be used to fit the

relationship between R_2^{ref} and SOC as follows,

$$R_2^{ref} = \sum_{k=0}^{n} r_k SOC^k[i(t), t] \tag{7.6}$$

A correction term $\alpha(T)$ is used to compensate for the variation of R_2 at different temperature conditions. One value of SOC is chosen first and then calculate the values of $I * R_2(SOC)$ and $I * R_2^{ref}(SOC)$. The correction term would be defined by (7.7).

$$\alpha(T) = \frac{I * R_2(SOC)}{I * R_2^{ref}(SOC)} \tag{7.7}$$

The selection of the SOC value can be arbitrarily because as shown subsequently, it does not cause any significant difference to the final simulation result. Normally, selecting SOC in the middle area of these curves yields a higher overall accuracy.

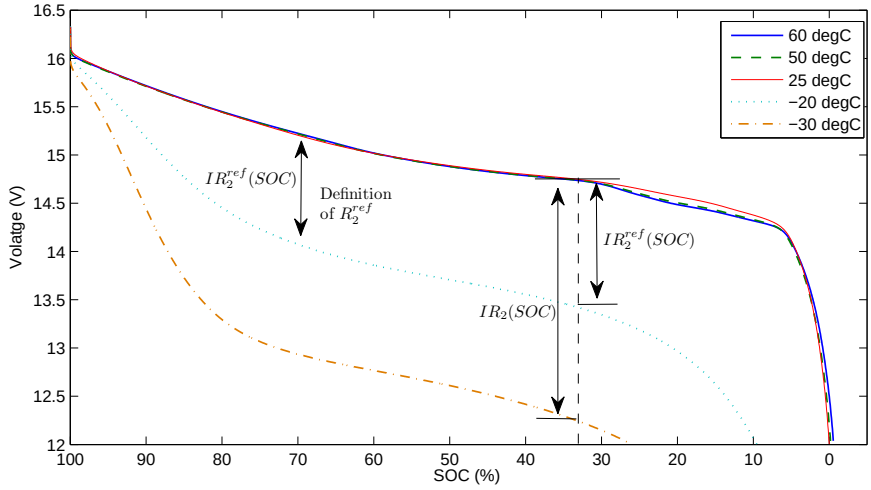

FIGURE 7.3: Determination of the R_2 for discharge condition at different temperatures

Actually the value of $\alpha(T)$ can only be obtained at certain temperatures based on the limited test results, i.e., $-30°C$, $-20°C$, $25°C$, $50°C$ and $60°C$ in Figure 7.3. A piecewise linear function can be built based on these five values and $\alpha(T)$ on other temperatures could be found from that function. Then R_2 can be expressed as

$$R_2 = \alpha(T) \sum_{k=0}^{n} r_k SOC^k[i(t), t] \tag{7.8}$$

7.2.1.2 Charging model

Compared with the discharging model for the battery, the charging model is much easier to build based on the strict charging condition from the manual of the lithium-ion battery, i.e., the charging temperature must be controlled between $10°C$ to $45°C$ and the charging current should not be greater than 3 A for a singe cell [130]. The manual also recommends using the standard constant current and constant voltage (CCCV) mode to charge the lithium-ion battery. Hence the charging behaviors would be very similar and the effects of the ambient temperature could be ignored in the charging mode.

The mathematical model in (7.1) can still be used to represent the charging mode without considering R_2. R_1 represents the voltage increment when $SOC = 0$ and can be obtained by using the similar method as in the discharging mode. The charging efficiency η_c will replace $\frac{1}{\eta_d}$ respectively.

7.2.2 Extended Kalman Filter

The Kalman Filtering algorithm is an optimum state estimator for a linear system, which can obtain an elegant and powerful solution. Extended Kalman Filter (EKF) is the nonlinear version of the Kalman Filter in estimation theory which linearizes around the current mean and covariance [139].

7.2.2.1 Adaptive EKF

For an optimal EKF operation, the measurement and process errors should be sequences of white Gaussian noise with zero mean. The operation of the EKF algorithm relies on the precise prior knowledge of the process and measurement errors in dynamic models and their properties. The uncertainty in the covariance parameters of processing noise (Q) and the observation errors (R) have a crucial impact on the EKF performance and may significantly degrade its performance. This is due to the fact that Q and R influence the weight that the EKF applies between the existing process information and latest measurements. Hence, the adaptive algorithm is involved to avoid this problem by estimating the Q and R parameters using the Maybeck's estimator of [140]. The summary of the employed adaptive EKF algorithm is shown in Table 7.1.

Based on the Maybeck's estimator, the approximate covariance parameters $\hat{\mathbf{Q}}$ and $\hat{\mathbf{R}}$ will be estimated in (7.9)

$$\begin{aligned}\hat{\mathbf{Q}}_k &= \tfrac{1}{\mathbf{N}} \sum_{j=k-N+1}^{k} (\mathbf{G}_j \mathbf{v}_j \mathbf{v}_j^T \mathbf{G}_j^T + \mathbf{P}_j \\ &\qquad -\mathbf{F}_{j-1}\mathbf{P}_{j-1}\mathbf{F}_{j-1}^T) \\ \hat{\mathbf{R}}_k &= \tfrac{1}{\mathbf{N}} \sum_{j=k-N+1}^{k} (\mathbf{v}_k^+ \mathbf{v}_k^{+T} - \mathbf{H}_j \mathbf{P}_j \mathbf{H}_j^T)\end{aligned} \tag{7.9}$$

where matrices $\mathbf{G}$, $\mathbf{P}$, $\mathbf{F}$, and $\mathbf{H}$ are given in Table 7.1. N is the number of recent sample periods. $\mathbf{v}_k$ and $\mathbf{v}_k{}^+$ are the observation error vectors calculated as

$$\begin{aligned}\mathbf{v}_j &= \mathbf{y}_j - \mathbf{h}(\hat{\mathbf{x}}_j^-, \mathbf{u}_j) \\ \mathbf{v}_j^+ &= \mathbf{y}_j - \mathbf{h}(\hat{\mathbf{x}}_j, \mathbf{u}_j)\end{aligned} \tag{7.10}$$

It should be noted that $\hat{\mathbf{Q}}$ is estimated assuming $\hat{\mathbf{R}}$ is known and $\hat{\mathbf{R}}$ is estimated assuming $\hat{\mathbf{Q}}$ is known in (7.9) [140]. The adaptive EKF can guarantee that the results are optimal. However, it cannot guarantee the estimated covariance is correct. Several ways are used to solve this problem. All the diagonal elements need to be reset to their absolute values in [141]. In [114] the negative eigenvalues of $\hat{\mathbf{Q}}$ and $\hat{\mathbf{R}}$ are reset to zero. The approach in [141] is used, i.e., diagonal elements in $\hat{\mathbf{Q}}$ and $\hat{\mathbf{R}}$ are set at their absolute value.

7.2.2.2 Linearization of the Proposed Lithium-ion Model

The *SOC* of lithium-ion batteries has a nonlinear relationship with its terminal voltage and current. In order to apply the EKF, the battery model in (7.1) must be linearized at every sampling instance.

During the discharging process, the *SOC* at the sampling time k is considered as the state variable. The state-space model in the discharging process can be defined in the following form:

$$\begin{aligned}SOC(k+1) &= SOC(k) - \tfrac{1}{\eta_d C} i(k)\delta t + \omega_k \\ V(k) &= E(k, T(k), i(k)) - (R_1 + R_2)i(k) + \upsilon_k\end{aligned} \tag{7.11}$$

An equilibrium potential $E(k, T(k), i(k))$ can be calculated from the reference discharge current curve, i.e., $E(k, T(k), i(k)) = V(SOC(k)) + (R_1 + R_2)i_r(k)$, where i_r is the

TABLE 7.1: Adaptive EKF algorithm

Non-linear state space model

$$\mathbf{x}_{k+1} = \mathbf{f}(\mathbf{x}_k, \mathbf{u}_k) + \mathbf{w}_k$$
$$\mathbf{y}_{k+1} = \mathbf{h}(\mathbf{x}_k, \mathbf{u}_k) + \mathbf{v}_k$$

where $\mathbf{w}_k$ and $\mathbf{v}_k$ are the processing and observation noises which are both assumed to be multivariate Gaussian noises of zero mean with covariance matrices $\mathbf{Q}_k = E[\mathbf{w}_k, \mathbf{w}_k^T]$ and $\mathbf{R}_k = [\mathbf{v}_k, \mathbf{v}_k^T]$ respectively.

Definitions

$$\mathbf{F}_k = \left.\frac{\partial \mathbf{f}(\mathbf{x}_k, \mathbf{u}_k)}{\partial \mathbf{x}}\right|_{\mathbf{x}=\hat{\mathbf{x}}_k} \qquad \mathbf{H}_k = \left.\frac{\partial \mathbf{h}(\mathbf{x}_k, \mathbf{u}_k)}{\partial \mathbf{x}}\right|_{\mathbf{x}=\hat{\mathbf{x}}_k^-}$$

Initialization

$$\hat{\mathbf{x}}_0 = E[\mathbf{x}_0] \quad \mathbf{P}_0 = E[(\mathbf{x}_0 - E[\mathbf{x}_0])(\mathbf{x}_0 - E[\mathbf{x}_0])^T]$$

For $k = 1, 2, \ldots,$ calculating
State estimation

$$\hat{\mathbf{x}}_k^- = \mathbf{f}(\hat{\mathbf{x}}_{k-1}, \mathbf{u}_{k-1})$$

Error covariance

$$\mathbf{P}_k^- = \mathbf{F}_{k-1}\mathbf{P}_{k-1}\mathbf{F}_{k-1}^T + \hat{\mathbf{Q}}_{k-1}$$

Kalman gain matrix update

$$\mathbf{G}_k = \mathbf{P}_k^-\mathbf{H}_k^T(\mathbf{H}_k\mathbf{P}_k^-\mathbf{H}_k^T + \hat{\mathbf{R}}_{k-1})^{-1}$$

State estimate update

$$\mathbf{v}_k = \mathbf{y}_k - \mathbf{h}(\hat{\mathbf{x}}_k^-, \mathbf{u}_k) \quad \hat{\mathbf{x}}_k = \hat{\mathbf{x}}_k^- + \mathbf{G}_k\mathbf{v}_k$$

Error covariance update

$$\mathbf{v}_k^+ = \mathbf{y}_k - \mathbf{h}(\hat{\mathbf{x}}_k, \mathbf{u}_k)$$
$$\mathbf{P}_k = (\mathbf{I} - \mathbf{G}_k\mathbf{H}_k)\mathbf{P}_k^-$$
$$\hat{\mathbf{R}}_k = \tfrac{1}{\mathbf{N}} \sum_{j=k-N+1}^{k} (\mathbf{v}_k^+\mathbf{v}_k^{+T} - \mathbf{H}_j\mathbf{P}_j\mathbf{H}_j^T)$$
$$\hat{\mathbf{Q}}_k = \tfrac{1}{\mathbf{N}} \sum_{j=k-N+1}^{k} (\mathbf{G}_j\mathbf{v}_j\mathbf{v}_j^T\mathbf{G}_j^T + \mathbf{P}_j - \mathbf{F}_{j-1}\mathbf{P}_{j-1}\mathbf{F}_{j-1}^T)$$

reference discharge current. Hence, equation (7.11) can be written as

$$\begin{aligned} SOC(k+1) &= f(SOC(k)) + \omega_k \\ V(k) &= h(SOC(k)) + \upsilon_k \end{aligned} \tag{7.12}$$

where,

$$\begin{aligned} f(SOC(k)) &= SOC(k) - \tfrac{\eta_d}{C} i(k)\delta t \\ h(SOC(k)) &= V(SOC(k)) \\ &\quad +(R_1+R_2)i_r(k) - (R_1+R_2)i(k) \end{aligned} \tag{7.13}$$

By definitions of $\mathbf{F}_k$ and $\mathbf{H}_k$ in Table 1, one can have

$$\begin{aligned} F_k &= \tfrac{\partial f(SOC)}{\partial SOC}\Big|_{SOC=S\hat{O}C(k)} = 1 \\ H_k &= \tfrac{\partial h(SOC)}{\partial SOC}\Big|_{SOC=S\hat{O}C(k)^-} \\ &= \tfrac{\partial g(SOC)}{\partial SOC}\Big|_{SOC=S\hat{O}C(k)^-} \end{aligned} \tag{7.14}$$

The SOC at the sampling time k is considered as the state variable during the charging process and its state-space model can be obtained by using the same approach of the above discharging process.

7.3 Implementation of Online Energy Management System for Lithium-ion Batteries

In the online energy management system for Li-ion batteries, one needs to detect the energy level of these batteries and whether they are in the charging state or discharging state. Besides, whether the next state should be charged or discharged also needs to be decided based on the energy level and the operation limits of Li-ion batteries.

Three operating modes are designed, i.e., charging mode, discharging mode and idle mode. The flow chart of the online energy management system for the Li-ion battery is shown in Figure 7.4 and I_e is a very small current that can be detected by the current meters.

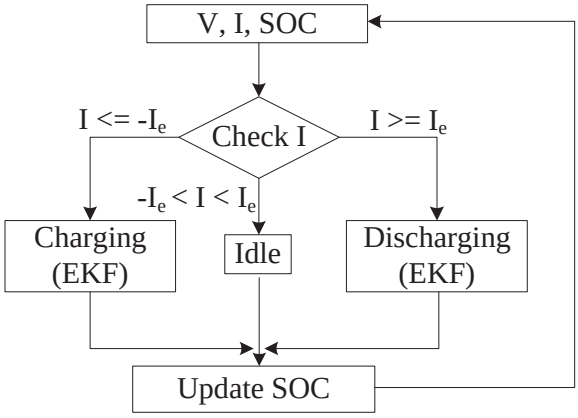

FIGURE 7.4: Flow chart of online energy management system for lithium-ion battery

When the current I flows out from the battery and is greater than or equal to I_e, the discharging mode is on. The adaptive EKF based on the battery discharging model is used to obtain SOC in the discharging mode. The idle mode is on if the absolute value of I is less than I_e. The current can be considered as zero and SOC is unchanged in the idle mode. The charging mode is on if I is less than or equal to $-I_e$. Adaptive EKF based on the battery charging model is employed to obtain SOC in the charging mode.

The NI 9225 C Series analog input module [142] is used to collect the analog signals in this chapter and the main adaptive EKF algorithm is implemented in the LabVIEW platform. The data flow is shown in Figure 7.5.

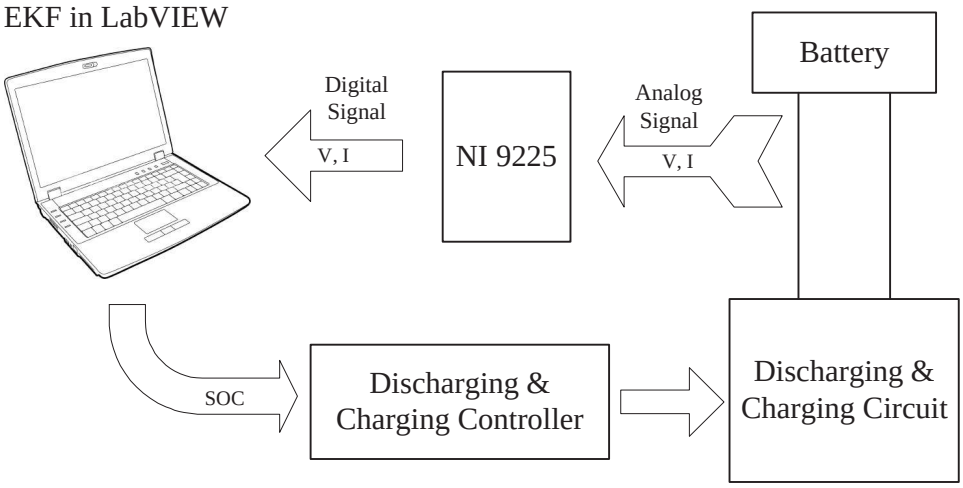

FIGURE 7.5: Data flow of online energy management system for lithium-ion batteries

The hardware setup is shown in Figure 7.6. The circuit at the top of Figure 7.6 is used to collect the charging data and discharging data. The latter includes discharging data at different constant current values and different constant ambient temperatures. Chroma 63200 electronic load is used to control the discharging current at different constant level in that circuit. Besides, a temperature chamber, SE-300, is also used to maintain the different constant temperature discharging conditions. The data collected from the circuit is used to build the battery charging and discharging models.

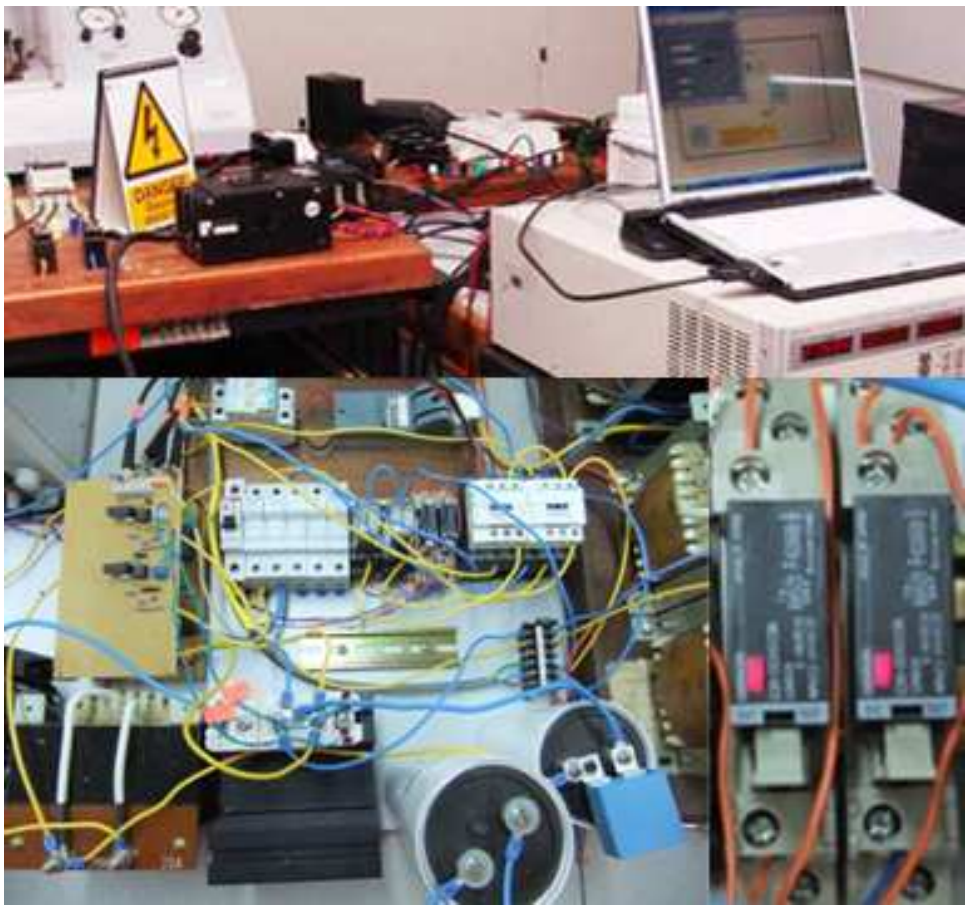

FIGURE 7.6: Hardware setup for online energy management system for lithium-ion batteries

The bottom-left of Figure 7.6 shows the bi-directional DC-DC buck-boost converter which is a part of the online energy management system for lithium-ion batteries. It can maintain the conditions of constant current, constant power and constant voltage

for the battery during the charging or discharging mode. The battery protection circuit is shown at the bottom-right of Figure 7.6.

7.4 Experimental Results and Analysis

Several case studies are performed to check the stability and robustness of the proposed state estimation model. The initial measurement noise covariance R and processing noise covariance Q are set to 0.002 [142] and 10^{-5} respectively. The charging efficiency η_c and discharging efficiency η_d are obtained at 0.87 and 0.96 respectively during the experiment. The battery lifecycle is not tested in the experiment due to the lack of battery lifecycle data, since it takes long time to collect the measurement. However, the age issue of the battery is addressed by the mathematical Li-ion model and the effectiveness and robustness of the proposed online management energy system can still be validated by the following case studies.

7.4.1 Discharging Mode

The experiment results of the proposed state estimation algorithm are collected and compared with the actual battery data. Both of the constant current and constant temperature are tested in the discharging mode. The discharging test is conducted under constant current levels of 1A, 2A, 3A, 4A and the temperature is $25°C$. The constant temperature discharging test is conducted under constant ambient temperature levels of $-30°C$, $-20°C$, $25°C$, $50°C$, $60°C$ and the discharging current is set at 1A.

Figure 7.7 shows the comparison between the actual and estimated SOC of three chosen discharging conditions, i.e., 1A and 3A under the ambient temperature of $25°C$ and 1A under the ambient temperature of $-20°C$. The solid line represents the actual data and the dotted line represents the estimated data. The actual SOC is calculated using coulomb counting which may include wrong initial SOC value, battery leakage current, and SOC drift, i.e., any small error in the integrated variable results in a drift in the SOC for the coulomb integration [143]. However, the battery leakage current and SOC drift are not very significant in the short time of coulomb counting and can be ignored

[144]. Hence, the coulomb counted SOC can be considered as the actual value with the correct initial SOC value, short time measurement and proper discharging efficiency.

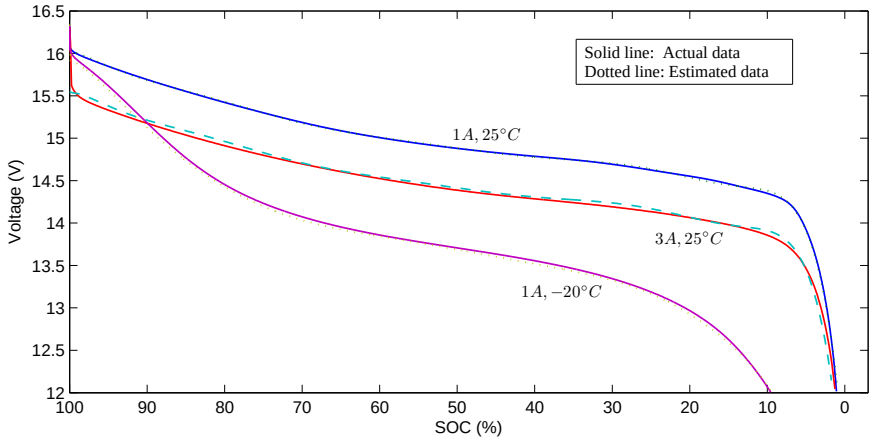

FIGURE 7.7: Comparison of actual and estimated data during battery discharge at different current and temperature levels

In Figure 7.7, some difference exists between the actual data and estimated data due to the error of the modeling and measurement. During the battery SOC estimation, this difference is expressed as a root mean square (RMS) error. The RMS error of the estimated data during the discharge is shown in Figure 7.8. For better comparison, the current is set at 1A during the different temperature discharge in Figure 7.8 (a) and the temperature is set at $25°C$ during the different current discharge in Figure 7.8 (b).

The error of SOC estimation during the different temperature discharge is shown in Figure 7.8 (a). The RMS error of SOC estimation is the lowest when the temperature is $25°C$ and it is 0.0040. It will increase with the temperature below and above $25°C$. However, the estimated SOC has a bigger error at the low temperature compared with the high temperature. As shown in Figure 7.8 (a), the RMS error of the SOC estimation is at the same value around 0.00455 when the temperature is between $-30°C$ and $-20°C$. When the ambient temperature is from $25°C$ to $50°C$ the SOC estimation error is nearly the same. Based on the RMS error given in Figure 7.8 (a), one can conclude that the best ambient temperature area for the SOC estimation of the proposed online energy management system for lithium-ion batteries is from $25°C$ to $50°C$. Other than this temperature range, the SOC estimation still works because the estimation error is still quite small.

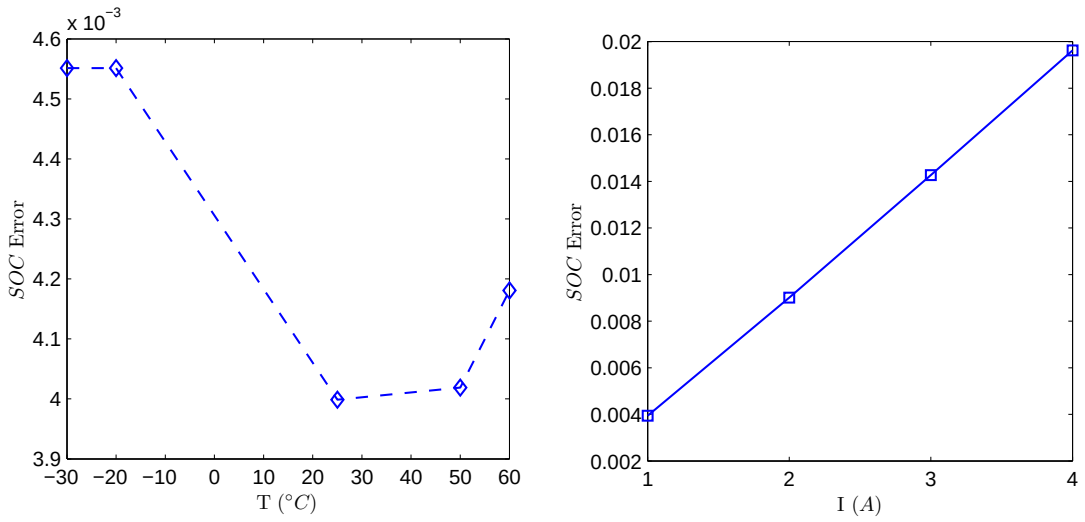

(a) RMS modeling error versus temperature

(b) RMS modeling error versus current

FIGURE 7.8: RMS error between the actual SOC and estimated SOC during battery discharge

The RMS error of estimated SOC during the different current discharge is shown in Figure 7.8 (b). The RMS estimation error will increase as the discharging current increases. It is 0.0046 when the discharging current is 1A and 0.0196 when discharging current is 4A. These RMS errors of the estimated SOC is less than 0.02 and the estimated SOC can be accepted for the online energy management system [138].

7.4.2 Charging Mode

Following the manual of the UBI-2590 lithium-ion battery, the standard UBI-2590 charger [145] is used to check the accuracy of the estimated SOC during the charging process. The CCCV pulse charging mode is the default setting in the UBI-2590 charger. The test results are shown in Figure 7.9.

Based on the measured voltage and current values, the estimated SOC converges quickly to the actual SOC in several seconds. The RMS error between the estimated and actual SOC is 0.0050.

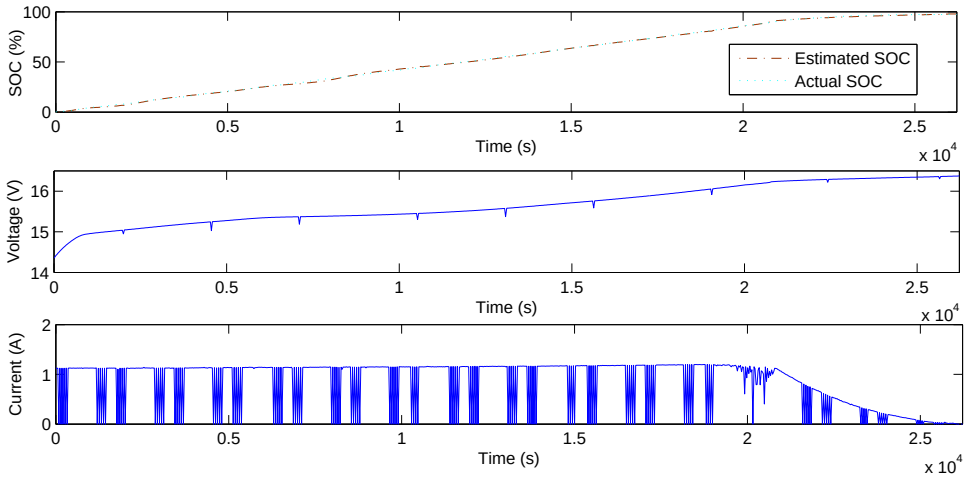

FIGURE 7.9: Test results of charging mode

7.4.3 Combined Mode

In the online energy management system for Li-ion batteries, the batteries may be charged at the present time period and may discharge its power in the next time period. Hence, it is very common to change from the charging to discharging mode or from discharging to charging mode for batteries. This is called the combined mode in this chapter. The initial SOC may not be known or incorrect in real time applications due to measurement faults. To simulate this scenario, the initial SOC in the combined mode test is set as 0.4, which is not correct for the online energy management system. The real initial SOC is about 0.061. The bi-directional DC-DC buck-boost converter is used to control the discharging and charging process of the batteries. The measured voltage and current of the combined mode are shown in Figure 7.10.

During the testing of the combined mode, the battery is in the idle mode and is not fully charged in the beginning. The battery is then changed to the discharging mode. The bi-directional DC-DC buck-boost converter tries to increase the discharging current from 0A to 2.5A during the period from the 16th second to the 35th second. The voltage of the battery drops substantially when the current increases because the battery is not fully charged in the beginning and is partly due to the polarization of the battery. The discharging current is maintained at 2.5A by the converter during the period from the 35th second to the 656th second. In the next 4 seconds, the discharging current drops to 0A and the battery is in the idle mode. The voltage of the battery will increase

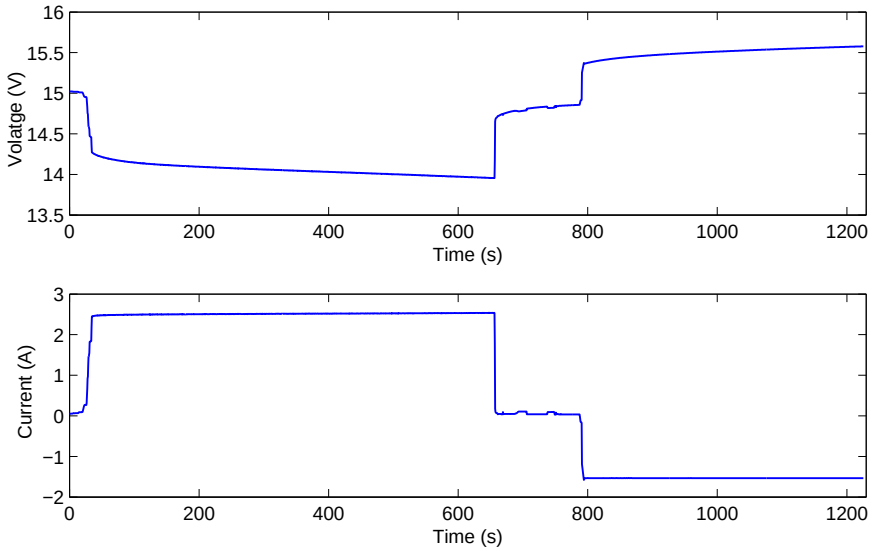

FIGURE 7.10: Measured voltage and current of combined mode

instantaneously when the discharging current drops to zero. It will increase slightly during the whole idle mode. This is because the battery is changed from the polarization state to the equilibrium state [135]. From the 790th second, the battery is changed to the charging mode and the charging current is increased to 1.5A at the 794th second. Due to the polarization, there is also a voltage deviation when the charging current is increased from 0A to 1.5A in a very short time. The estimated SOC of the combined mode is shown in Figure 7.11.

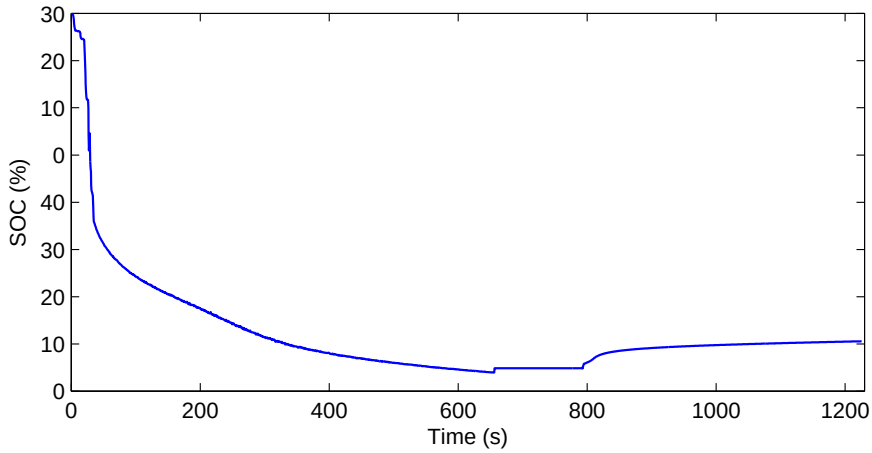

FIGURE 7.11: SOC for combined mode

In the proposed method, the adaptive EKF will detect the correct SOC using the measured dynamic voltage and current values and it is computed via the relationship among the SOC, voltage and current in the mathematical battery model. As shown in Figure 7.11, the initial SOC is not correct and the estimated SOC based on the proposed method will try to correct SOC with the dynamic battery voltage and current values. After several minutes, the estimated SOC will be very close to the real value based on its own natural characteristic which is already included in the mathematical model.

The actual initial SOC is about 0.061. It takes 280 seconds to detect the correct SOC during the discharging process of the Li-ion battery using the proposed method. A comparison between the actual SOC and the estimated SOC by the proposed method is shown in Figure 7.12. The actual SOC is based on the coulomb counting in a short time under the correct initial SOC and the preset charging or discharging efficiency is shown as the curve with star symbols in Figure 7.12. After the correct SOC is detected in a very short time, the proposed method can obtain the estimated SOC which tracks the atucal value very well.

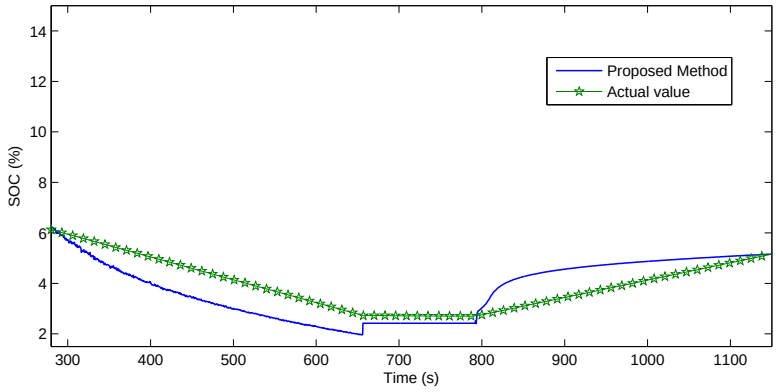

FIGURE 7.12: SOC comparison for combined mode based on proposed method

The RMS error between the estimated SOC based on the proposed method and the actual value is about 0.79%.

7.4.4 Comparison with other SOC estimation techniques

In order to check the performance of the proposed method, the results from the other SOC estimation methods are used to compare with the results in this chapter, as shown

in Table II. The EKF-Ah based SOC estimation can yield a RMS error less than 6% at room temperature [146]. The discharge current is from 2A to 6A during the test. The SOC estimation based on the adaptive EKF and nueral network can give a smaller RMS error of 1%-3% at room temperature. The discharge current is about 1A [114] [147]. The proposed battery model is also tested using the data from [33] and the RMS error is less than 0.02 [148].

TABLE 7.2: Comparison with different methods

Online SOC estimation methods		RMS	Test temperature	Test current
Battery modeling	Filtering method			
EKF-Ah Based method	EKF	less than 6%	20 - 25$^{\circ}C$	2 - 6A
Neural network method	Adaptive EKF	1% - 3%	20 - 25$^{\circ}C$	Around 1A
Proposed battery model	Adaptive EKF	0.4% - 1.96%	$-30^{\circ}C$ - 60$^{\circ}C$	1 - 4A

Compared with other SOC estimation methods, the RMS error based on the proposed method is reduced. This means that the proposed method can yield better accuracy. The proposed method is also tested under different temperature conditions and different discharge currents.

7.5 Conclusion

The online energy management system for Li-ion battery is developed in this chapter. It uses the dynamic measured online terminal voltage and current to estimate the SOC of the Li-ion battery. The proposed estimation technique combines the indirect and direct methods. The effect of polarization and change of ambient temperature of the Li-ion battery are included in the proposed mathematical model. Besides, the age issue of the battery is also addressed by the mathematical model. The adaptive EKF is performed to deal with the errors of the initial SOC and the dynamic voltage and current measurements.

Experimental results show that the estimated SOC during the discharging process or charging process is very close to the actual value and the RMS error is less than 0.02 under different operating currents and different ambient temperatures. The robustness of the online energy management system of the Li-ion battery is also verified in the combined mode. The estimated SOC can track the correct actual value in several minutes

even if the initial SOC is set incorrectly. The RMS error between the estimated SOC and the possible actual value is also less than 0.02. Compared with other SOC estimation methods, this is more accurate. This method can also be used for other types of batteries. However, the values of the parameters only work for lithium-ion batteries.

Furthermore, it is necessary to measure the current and voltage of each cell if the proposed online energy management system is implemented for a Li-ion battery bank. Otherwise, each cell inside the battery bank is assumed to operate under the same charging or discharging conditions.

Chapter 8

Conclusion and Future Works

8.1 Conclusion

In this chapter, the importance, aims and outcomes of this research are highlighted and summarized. The research is discussed in terms of what it aims for and how it could contribute to the needs of the power industry. It also explores, how the research of smart grids could be extended and improved and how this might be done.

By making optimal use of the sustainable and varied energy sources as part of the smart grid, the smart grid may be able to make a significant contribution to the distributed power generation. The key is how to orchestrate the power sources in an optimal manner. The inclusion of batteries in a smart grid system allows excess power produced to be stored, or alternatively, the excess power could be put into use in the smart grid. In this way it is expected that the smart grid could reduce pollution and deliver reliable energy in a variety of weather and load situations.

To understand the behavior of a smart grid, this thesis develops models suitable for overall analysis and design in Chapter 2. Time series and FNN are used to forecast the wind speed and solar radiation and the forecast error is considered for the wind and solar power. The final goal is to lay a groundwork which would allow efficient management of the smart grid by minimizing the operating costs and reducing emission level while meeting the load demand. More specifically, the optimal placement of the capacitor for

the renewable energy is addressed in Chapter 3 and the scheduling of energy storage in a PV/battery system is discussed in Chapter 4.

In Chapter 3, the economic optimization method for capacitor planning in the power system is tested on the IEEE 14-bus test system. The cost function of the capacitor is designed to include the one-time cost, maintenance cost, capacitor's life time and interest rate for financing the installed capacitors. Hence, they make this optimal capacitor planning method more realistic. The line loss penalty is also considered and the results show that GENCOs could get minimum loss penalty as well as obtain the minimum generation cost via the optimization. A special algorithm is proposed for the scheduling of energy storage in a PV/battery system in Chapter 4. The battery charging/discharging characteristics, current and temperature dependence are considered and the schedule algorithm is tested in the SIMPLORER environment.

SEMS is developed in Chapter 5. It is a core part for a smart grid system, which can make this system more intelligent. In SEMS, the recommended MW/MVar amounts rescheduled are sent to generators, FACTS, OLTCs and load controllers for immediate implementation via communication devices. Through constant monitoring and real-time security control, it is possible to coordinate the operation of the smart grid and upstream grid supply such that the smart grid can aid the external system during system-wide emergency by exporting its generation as much as it could without jeopardizing its own security and at times of its own shortage, the smart grid can count on the upstream grid to meet its needs.

To handle the multi-objective optimization in SEMS, the Jump and Shift method is also proposed. It aims to solve a large scale linear/nonlinear programming problem where its constraints are coupled to another large scale linear/nonlinear programming problem. The shift factor χ is used to speed the convergence of the iterative solution. The results of the 14-bus and 112-bus power systems show that the expected goals of system optimization can be achieved by SEMS through the Jump and Shift method.

ESS plays an important role in the mitigation of renewable power intermittencies, load mismatches of the MG system. The sizing issues and online management of ESS has been addressed in Chapter 6 and Chapter 7 respectively.

A complicated problem of solving the optimal BESS size can be solved by the method presented in Chapter 6. The method is tested using the forecasting data over a day in a MG. The case study adopts a cost-benefit analysis approach to estimate the economic feasibility of the ESS for the MG project. The quantitative results of the case study show that ESS for MG could decrease the cost of output power and spinning reserve for the traditional generators. As the size of ESS increases, the cost of traditional generators decreases. ESS can store the surplus renewable energy and re-dispatch it appropriately. This could reduce the power supported by traditional generators and cut down the cost. Besides, the ESS can balance the power generated by the traditional generators, which could make the generators work at a stable condition and reduce their cost.

The online energy management system for Li-ion battery is developed in Chapter 7. It can help to estimate the SOC during the charging or discharging processes. The proposed estimation technique combines the indirect and direct methods. The adaptive EKF is performed to deal with the errors of the initial SOC and the dynamic voltage and current measurements. The effectiveness and robustness of the online energy management system of Li-ion battery is verified. The estimated SOC can track the correct actual value in several minutes even if the initial SOC is set incorrectly. Compared with the traditional method, The RMS error is quite small.

8.2 Future Works

The important aspect of the research work is to obtain some actual smart grid data rather than data from individual power sources or IEEE test system. During this research work we were unable to find any actual data of the smart grid elsewhere implemented or reported in the literature. This is likely because smart grid is a relatively new idea and therefore no data is currently available. A real 125-kW MG is being constructed at NTU as part of the A$\star$STAR Intelligent Energy Distribution System (IEDS) project initiatives launched in 2007. Another 1-MW MG system is also under construction at Institute of Chemical and Engineering Sciences (ICES). We will try to implement the proposed methods of the this research work in the NTU MG. Furthermore, these methods will also implemented in the land-based energy management system (LEMS) that is capable of incorporating renewable and traditional energy resources in a 30-MVA power system for the shipyard industry.

Forecasting technology of renewable energy is involved in the system modeling of smart grid in this thesis. However, the forecasted error is quite big compared with the load forecast in the large power system without renewable energy resources in the literature. The hybrid forecast technique should be implemented to deal with the renewable energy forecasting issues. Besides, the statistical methods also need to be involved when we consider the renewable energy in the smart grid. With the statistical methods, the optimal placement of the capacitor for smart grid can be considered in a long term, which is more reasonable.

The sizing issues and online management of ESS have been discussed in this thesis. However, only the lithium-ion battery is studied. As we know, even if the lithium-ion battery can support large power in a long time, it has limited instantaneous power, which cannot support huge power to grid in a very short time. The other type of energy storage, super capacitor, can overcome this issue. Hence, a hybrid ESS should be considered for the smart grid in the future.

Another future work is to suitably incorporate the market price in the smart energy management system [149]. It plays a very important role for MGs to buy/sell electrical power from/to the upstream or neighboring grid in smart power systems. The earliest introduction of energy market concepts and privatization of electric power systems took place in Chile in the early 1980s. One of the principal purposes of the introduction of market concepts in Argentina was to privatize existing generation assets which had fallen into disrepair under the government-owned monopoly, resulting in frequent service interruptions and to attract capital needed for rehabilitation of those assets and for system expansion. During the 1990s, the World Bank was active in introducing a variety of hybrid markets in other Latin American nations, including Peru, Brazil and Colombia, but with limited success. Considering the new generation of smart grids or MGs, interfacing with the upstream market price is also a very important part for SEMS. When more and more smart grids or MGs are incorporated as part of the electricity market, the demand market will be more elastic and runs more ideal in its operation.

It is anticipated that further research and development will be carried out on the system, with the goal that MGs will be able to make a valid, greener contribution to the world's growing energy needs.

Appendix A

Interior Point Method

Consider a nonlinear problem that can be compactly described as follows [150]:

$$\begin{aligned} Min \quad & f(x) \\ s.t. \quad & g(x) = 0 \\ & h_{min} \leq h(x) \leq h_{max} \end{aligned} \tag{A.1}$$

where $h(\cdot)$ represents the vector of inequality constraints that contains the reactive power constraints. The parameters, h_{min} and h_{max}, correspond to the lower and upper limits of the vector of inequality constraints in (A.1).

Slack variables are introduced to convert inequality constraints into equality ones as follows.

$$\begin{aligned} h(x) - s_L - h_{min} = 0 \qquad s_L \geq 0 \\ h(x) + s_U - h_{max} = 0 \qquad s_U \geq 0 \end{aligned} \tag{A.2}$$

where s_L and s_U indicate the lower and the upper slack variables.

With a log barrier function, the following Lagrangian function is established.

$$\begin{aligned} L(s, s_L, s_U, \lambda, \pi_L, \pi_U, \mu) = f(x) - \lambda^T g(x) - \pi_L^T (h(x) - s_L - h_{min}) \\ -\pi_U^T (h(x) - s_U - h_{max}) \\ -\mu \left(\prod_i ln s_{Li} + \prod_i ln s_{Ui} \right) \end{aligned} \tag{A.3}$$

where the following notations are used:

λ: Vector of Lagrangian multipliers for $g(\cdot) = 0$

π_L: Vector of Lagrangian multipliers for $h(\cdot) - s_L - h_{min} = 0$

π_U: Vector of Lagrangian multipliers for $h(\cdot) - s_U - h_{max} = 0$

μ: Barrier parameter

The Karush-Kuhn-Tucker (KKT) first-order necessary optimality condition of the Lagrangian function can be derived as follows:

$$\begin{aligned}
&L_x \equiv \nabla_x f(x) - \nabla_x g(x)\lambda - \nabla_x h(x)(\pi_L + \pi_u) = 0 \\
&L_\lambda \equiv g(x) = 0 \\
&L_{\pi_L} \equiv h(x) - s_L - h_{min} = 0 \\
&L_{\pi_U} \equiv h(x) + s_U - h_{max} = 0 \\
&L_{s_L} \equiv \pi_L - S_L^{-1}\mu e = 0 \\
&L_{s_U} \equiv \pi_U + S_U^{-1}\mu e = 0
\end{aligned} \tag{A.4}$$

where S_L and S_U are diagonal matrices whose diagonal elements are the elements of s_L and s_U respectively, and e is the vector whose elements are all 1. For easy differentiation of the KKT first-order condition, the last two equations in (A.4) are changed into the following equations.

$$\begin{aligned}
&\tilde{L}_{s_L} \equiv S_L \Pi_L e - \mu e = 0 \\
&\tilde{L}_{s_U} \equiv S_U \Pi_U e + \mu e = 0
\end{aligned} \tag{A.5}$$

where Π_L and Π_U are diagonal matrices whose diagonal elements are the elements of π_L and π_U respectively. From the initial guess, the correction equations of the first-order condition using the Newton method are as follows:

$$\begin{aligned}
&H\Delta x + \nabla_x g(x)\Delta\lambda + \nabla_x h(x)(\Delta\pi_L + \Delta\pi_U) = L_x^0 \\
&H \equiv \nabla_x^2 g(x)\lambda + \nabla_x^2 h(x)(\pi_L + \pi_U) - \nabla_x^2 f(x) \\
&\nabla_x g(x)^T \Delta x = -L_\lambda^0 \\
&\nabla_x h(x)^T \Delta x - \Delta s_L = -L_{\pi_L}^0 \\
&\nabla_x h(x)^T \Delta x + \Delta s_U = -L_{\pi_U}^0 \\
&S_L \Delta\pi_L + \Pi_L \Delta s_L = -\tilde{L}_{s_L}^0 \\
&S_U \Delta\pi_U + \Pi_U \Delta s_U = -\tilde{L}_{s_U}^0
\end{aligned} \tag{A.6}$$

where the right-hand side notations represent residuals of the KKT first-order-condition, which are derived in (A.4) and (A.5).

To reduce the size of the above correction equations, the following linear system which can be easily derived from (A.6) is used:

$$\begin{aligned}
&\begin{bmatrix} \tilde{H} & \nabla_x g(x) \\ \nabla_x g(x)^T & 0 \end{bmatrix} \begin{bmatrix} \Delta x \\ \Delta\lambda \end{bmatrix} = \begin{bmatrix} R_x \\ R_\lambda \end{bmatrix} \\
&\tilde{H} \equiv H + \nabla_x h(x)(S_U^{-1}\Pi_U - S_L^{-1}\Pi_L)\nabla_x h(x)^T \\
&R_x \equiv L_x^0 + \nabla_x h(x)(S_L^{-1}\Pi_L L_{\pi_L}^0 - S_U^{-1}\Pi_U L_{\pi_U}^0 + S_L^{-1}\tilde{L}_{s_L}^0 - S_U^{-1}\tilde{L}_{s_U}^0) \\
&R_\lambda \equiv -L_\lambda^0
\end{aligned} \tag{A.7}$$

The widely used procedure in the IPM is outlined as follows.

1. Initialize the primal and dual variables.
2. Compute the complementary gap: $G_C = \pi_L^T s_L + \pi_U^T s_U$. If the gap and the residuals are less than the given tolerances, output the optimal solution and stop.
3. Compute the barrier parameter with $\mu = \sigma\frac{G_C}{2r}$ where r is the number of constraints and σ ($\sigma \in (0, 1]$) is the centering parameter.
4. Solve the correction vector Δx and $\Delta\lambda$ in (A.7). Then obtain Δs_L, Δs_U, $\Delta\pi_L$ and $\Delta\pi_U$ based on (A.6).
5. Update the primal and dual variables and go to step 2.

Appendix B

14-bus Power System

The data is modified from the IEEE test power system.

TABLE B.1: Active and reactive load ($kW/kVAr$)

	Bus 2		Bus 3		Bus 4		Bus 5		Bus 6		Bus 9		Bus 10		Bus 11		Bus 12		Bus 13		Bus 14	
Hour	P	Q	P	Q	P	Q	P	Q	P	Q	P	Q	P	Q	P	Q	P	Q	P	Q	P	Q
1	217	50	942	70	478	-39	176	16	212	75	295	80	190	58	135	18	161	16	135	58	200	50
2	210	60	912	60	462	-30	173.5	15	209	75	285	80	186	55	135	15	160	15	130	55	230	45
3	200	46	868	65	440	-35	170	13	204	75	272	75	182	50	135	16	170	13	135	50	280	48
4	190	50	825	60	418	-39	166.5	15	199	75	258	80	178	58	140	18	161	16	131	55	320	50
5	200	48	868	70	440	-40	170	16	204	75	272	85	182	58	150	20	160	17	150	58	350	50
6	210	50	912	65	462	-45	173.5	18	209	75	286	90	186	60	135	21	161	18	145	60	400	51
7	250	55	1085	60	550	-48	187.5	19	230	75	340	90	203	63	150	22	190	20	166	58	425	53
8	280	60	1215	75	616	-50	198	20	246	75	381	95	215	68	150	23	195	22	155	58	450	55
9	300	65	1302	80	660	-55	205	23	256	75	408	100	223	70	160	25	200	23	136	58	450	58
10	350	70	1519	85	770	-60	222.5	25	282	75	476	110	243	73	160	28	205	25	160	58	475	60
11	380	70	1649	85	836	-55	233	28	298	75	517	120	256	75	165	30	215	28	150	58	480	63
12	400	75	1736	90	880	-55	240	30	308	75	544	125	264	75	180	33	230	27	155	58	500	65
13	390	80	1692	90	858	-50	236.5	28	303	75	530	130	260	80	175	30	220	30	165	58	520	68
14	390	75	1692	80	858	-60	236.5	25	303	75	530	135	260	75	170	28	210	32	160	58	550	70
15	380	70	1649	85	836	-65	233	25	298	75	517	130	256	73	170	25	200	30	150	58	580	73
16	350	80	1519	80	770	-60	222.5	30	282	75	476	130	276	70	160	28	190	28	155	58	600	70
17	380	85	1649	90	836	-55	233	32	298	75	517	125	268	73	178	30	195	25	145	58	560	72
18	430	80	1866	85	946	-55	250.5	31	323	75	585	135	263	80	183	35	200	23	150	58	485	72
19	410	78	1779	80	902	-50	243.5	28	313	75	558	140	260	73	180	30	205	28	155	58	400	70
20	400	65	1736	75	880	-49	240	25	308	75	544	135	247	70	175	28	200	23	145	58	352	68
21	360	60	1562	70	792	-45	226	23	287	75	490	130	225	68	160	18	190	20	140	58	300	63
22	310	58	1085	70	682	-40	208.5	20	261	75	422	120	220	63	150	28	180	18	136	58	245	60
23	250	55	955	70	550	-39	187.5	16	230	75	340	100	215	58	155	23	170	16	135	58	240	55
24	220	50	950	70	484	-39	177	16	215	75	300	90	193	55	138	19	161	15	130	58	230	53

Bibliography

[1] E. F. C. Group, "Challenge and opportunity: Charting a new energy future," Energy Future Coalition, Tech. Rep., 2003.

[2] G. Klimstra and M. Hotakainen, *Smart Power Generation*. Avain Publishers, Helsinki, 2011.

[3] K. Geisler, "A smarter greener power grid," in *Power Syst. Conf.*, Mar. 2009, pp. 1–3.

[4] W. Jiang and B. Fahimi, "Active current sharing and source management in fuel cellcbattery hybrid power system," *IEEE Trans. Ind. Electron.*, vol. 57, no. 2, pp. 752–761, Feb. 2010.

[5] M. Cugnet, J. Sabatier, S. Laruelle, S. Grugeon, B. Sahut, A. Oustaloup, and J.-M. Tarascon, "On lead-acid-battery resistance and cranking-capability estimation," *IEEE Trans. Ind. Electron.*, vol. 57, no. 3, pp. 909–917, Mar. 2010.

[6] W. Li, G. Joos, and J. Belanger, "Real-time simulation of a wind turbine generator coupled with a battery supercapacitor energy storage system," *IEEE Trans. Ind. Electron.*, vol. 57, no. 4, pp. 1137–1145, Apr. 2010.

[7] B. Lu and M. Shahidehpour, "Short-term scheduling of battery in a grid-connected pv/battery system," *IEEE Trans. Power Syst.*, vol. 20, no. 2, pp. 1053–1061, May. 2005.

[8] X. Lemaire, "Glossary of terms in sustainable energy regulation," Renewable Energy and Efficiency Partnership, Tech. Rep., 2004.

[9] (2010) Invvest definition of sustainable energy. [Online]. Available: http://www.invvest.org/blog/invVEST-Definition-of-Sustainable-Energy/

[10] J. S. D. Network. (2008) Invvest definition of sustainable energy. [Online]. Available: http://bit.ly/rSImY7

[11] (2007) Natural forcing of the climate system. [Online]. Available: http://bit.ly/vEz2t7

[12] R. Somerville, "Historical overview of climate change science," Intergovernmental Panel on Climate Change, Tech. Rep., 2007.

[13] W. Vermass. (2007) An introduction to photosynthesis and its applications. [Online]. Available: http://photoscience.la.asu.edu/photosyn/education/photointro.html

[14] O. Morton. (2008) Solar energy: A new day dawning? [Online]. Available: http://www.nature.com/nature/journal/v443/n7107/full/443019a.html

[15] Exergy (available energy) flow charts. [Online]. Available: http://www.nature.com/nature/journal/v443/n7107/full/443019a.html

[16] Solar energy. [Online]. Available: http://www.solarenergybyzip.com/

[17] (2008) Where does the wind come from and how much is there. [Online]. Available: http://bit.ly/rwdSdb

[18] (2006) International energy outlook. [Online]. Available: http://www.eia.gov/oiaf/archive/ieo06/special_topics.html

[19] W. W. E. Association, "World wind energy report 2010," World Wind Energy Association, Tech. Rep., 2011.

[20] (2010) Wind power increase in 2008 exceeds 10-year average growth rate. [Online]. Available: http://bit.ly/ugUvQi

[21] B. Consult, "International wind energy development world market update," BTM Consult, Tech. Rep., 2009.

[22] REN21, "Renewables 2011: Global status report," REN21, Tech. Rep., 2011.

[23] G. Wand, "Fuel cells history part 1," Johnson Matthey, Tech. Rep., 2008.

[24] W. R. Grove, "On voltaic series and the combination of gases by platinum," *Philosophical Magazine and Journal of Science*, vol. XIV, pp. 127–130, Dec. 1838.

[25] ——, "On a gaseous voltaic battery," *Philosophical Magazine and Journal of Science*, vol. XXI, pp. 417–420, Mar. 1842.

[26] Fuel cell block diagram. [Online]. Available: http://en.wikipedia.org/wiki/File:Fuel_Cell_Block_Diagram.svg#filelinks

[27] K. Nice and J. Strickland. (2011) How fuel cells work: Polymer exchange membrane fuel cells. [Online]. Available: http://auto.howstuffworks.com/fuel-efficiency/alternative-fuels/fuel-cell2.htm

[28] C. Shuaixun, "Modeling of lithium-ion battery for energy storage system simulation," Master's thesis, School of Electrical and Electronic Engineering, Nanyang Technological University, 2008.

[29] C. M. Jefferson and K. Neilson, "Supercapacitor energy storage system," in *Universities Power Eng. Conf.*, vol. 1, 1994, pp. 275–277.

[30] H. Makinen, R. Mikkonen, and J.-T. Eriksson, "Availability analysis of a 100 kwh superconducting magnetic energy storage," in *International Conf. on Magnet Technology*, vol. 1, 1994.

[31] A. Friedman, N. Shaked, E. Perel, M. Sinvani, Y. Wolfus, and Y. Yeshurun, "Superconducting magnetic energy storage device operating at liquid nitrogen temperatures," *Cryogenics*, vol. 39, no. 1, pp. 53–58, 1999.

[32] J. P. Nelson and W. D. Bolin, "Basics and advances in battery systems," *IEEE Trans. Ind. Appl.*, vol. 31, no. 2, pp. 419–428, Apr. 1995.

[33] L. Gao, S. Liu, and R. Dougal, "Dynamic lithium-ion battery model for system simulation," *IEEE Trans. Compon. Packag. Technol.*, vol. 25, no. 3, pp. 495–505, Sep. 2002.

[34] (2011) Linear programming. [Online]. Available: http://en.wikipedia.org/wiki/Linear_programming

[35] R. Lasseter and P. Paigi, "Microgrid: a conceptual solution," in *IEEE 35th Annual Power Electron. Special. Conf.*, vol. 6, Jun. 2004, pp. 4285–4290.

[36] N. Hatziargyriou, "Microgrids," *IEEE Power Energy Mag.*, vol. 6, no. 3, pp. 26 –29, May-Jun. 2008.

[37] F. Mohamed and H. Koivo, "Microgrid online management and balancing using multiobjective optimization," in *2007 IEEE Lausanne, Power Tech*, Jul. 2007, pp. 639–644.

[38] T. Kato, Y. Suzuoki, T. Funabashi, L. Cipcigan, and P. Taylor, "Microgrid configuration for major network events," in *2008. IET-CIRED. CIRED Seminar, SmartGrids for Distrib.*, Jun. 2008, pp. 1–4.

[39] J. Pecas Lopes, C. Moreira, and A. Madureira, "Defining control strategies for analysing microgrids islanded operation," in *2005 IEEE Russia, Power Tech*, Jun. 2005, pp. 1–7.

[40] B. Kroposki, T. Basso, and R. DeBlasio, "Microgrid standards and technologies," in *Power & Energy Soc. General Meeting*, Jul. 2008.

[41] (2009, Jul.) Microgrid energy management framework. [Online]. Available: http://bit.ly/f98iSX

[42] B. Kroposki, C. Pink, T. Basso, and R. DeBlasio, "Microgrid standards and technology development," in *Power Eng. Soc. General Meeting*, Jun. 2007, pp. 1–4.

[43] T. Ise, Y. Hayashi, and K. Tsuji, "Definitions of power quality levels and the simplest approach for unbundled power quality services," in *Harmon. and Qualit. of Power Conf.*, vol. 2, 2000, pp. 385–390.

[44] G. Venkataramanan and C. Marnay, "A larger role for microgrids," *IEEE Power Energy Mag.*, vol. 6, no. 3, pp. 78–82, May-Jun. 2008.

[45] N. Karmarkar, "A new polynomial-time algorithm for linear programming," *Combinatorica*, vol. 4, no. 4, pp. 373–395, 1984.

[46] S. Wright, *Primal-dual interior-point methods*. Society for Industrial and Applied Mathematics, 1997.

[47] C. Sharma, "Modeling of an island grid," *IEEE Trans. Power Syst.*, vol. 13, no. 3, pp. 971–978, Aug. 1998.

[48] G. Pepermans, J. Driesen, D. Haeseldonckx, R. Belmans, and W. D'haeseleer, "Distributed generation: Definition, benefits and issues," *Energy Policy*, vol. 33, no. 6, pp. 787–798, 2005.

[49] (2000, Oct.) Fuel cell handbook. fchandbook.pdf. [Online]. Available: http://www.fuelcells.org/info/library/fchandbook.pdf

[50] R. Billinton, H. Chen, and R. Ghajar, "Time-series models for reliability evaluation of power systems including wind energy," *Microelectron. and Reliab.*, vol. 36, no. 9, pp. 1253–1261, 1996.

[51] J. Taylor, P. McSharry, and R. Buizza, "Wind power density forecasting using ensemble predictions and time series models," *IEEE Trans. Energy Convers.*, vol. 24, no. 3, pp. 775–782, Sep. 2009.

[52] T. Barbounis, J. Theocharis, M. Alexiadis, and P. Dokopoulos, "Long-term wind speed and power forecasting using local recurrent neural network models," *IEEE Trans. Energy Convers.*, vol. 21, no. 1, pp. 273–284, Mar. 2006.

[53] B. Ernst, B. Oakleaf, M. Ahlstrom, M. Lange, C. Moehrlen, B. Lange, U. Focken, and K. Rohrig, "Predicting the wind," *IEEE Power Energy Mag.*, vol. 5, no. 6, pp. 78–89, nov. 2007.

[54] R.-H. Liang and J.-H. Liao, "A fuzzy-optimization approach for generation scheduling with wind and solar energy systems," *IEEE Trans. Power Syst.*, vol. 22, no. 4, pp. 1665–1674, Nov. 2007.

[55] B. Borowy and Z. Salameh, "Optimum photovoltaic array size for a hybrid wind/pv system," *IEEE Trans. Energy Convers.*, vol. 9, no. 3, pp. 482–488, Sept. 1994.

[56] Wind power. [Online]. Available: http://www.fenglifadian.com/fenglifadianji/

[57] S. X. Chen, H. B. Gooi, and M. Q. Wang, "Sizing of energy storage for microgrids," *IEEE Trans. Smart Grid*, vol. 3, no. 1, pp. 142–151, Mar. 2012.

[58] L. Soder, "Simulation of wind speed forecast errors for operation planning of multiarea power systems," in *Probabil. Methods Applied to Power Syst.*, Sep. 2004, pp. 723–728.

[59] R. Perez, R. Seals, P. Ineichen, R. Stewart, and D. Menicucci, "A new simplified version of the perez diffuse irradiance model for tilted surfaces," *Solar Energy*, vol. 39, no. 3, pp. 221–231, 1987.

[60] S. Chiang, K. Chang, and C. Yen, "Residential photovoltaic energy storage system," *IEEE Trans. Energy Convers.*, vol. 45, no. 3, pp. 385 –394, Jun. 1998.

[61] W. Xiao, M. Lind, W. Dunford, and A. Capel, "Real-time identification of optimal operating points in photovoltaic power systems," *IEEE Trans. Ind. Electron.*, vol. 53, no. 4, pp. 1017 –1026, Jun. 2006.

[62] C. Tao, D. Shanxu, and C. Changsong, "Forecasting power output for grid-connected photovoltaic power system without using solar radiation measurement," in *Power Electron. for Distrib. Generation Syst. (PEDG), 2010 2nd IEEE International Symposium on*, Jun. 2010, pp. 773–777.

[63] A. Yona, T. Senjyu, and T. Funabashi, "Application of recurrent neural network to short-term-ahead generating power forecasting for photovoltaic system," in *Power & Energy Soc. General Meeting*, Jun. 2007, pp. 1–6.

[64] A. I. Galushkin, *Neural Networks Theory*. Dordrecht: Springer, 2007.

[65] G. H. B. Cheah Peng Huat and S. F. Lan, "Quarter-hour-ahead load forecasting for microgrid energy management system," in *IEEE PES PowerTech 2011*, Jun. 2011.

[66] R. Perez, R. Seals, P. Ineichen, R. Stewart, and D. Menicucci, "A new simplified version of the perez diffuse irradiance model for tilted surfaces," *Solar Energy*, vol. 39, no. 3, pp. 221–231, 1987.

[67] A. Iga and Y. Ishihara, "Characteristics and embodiment of the practical use method of monthly temperature coefficient of the photovoltaic generation system," *IEEJ Trans. Power and Energy*, vol. 126, no. 8, pp. 767–775, 2006.

[68] R. D. Zimmerman, "Matpower user's manual," Power Systems Engineering Research Center, Tech. Rep., 2010.

[69] T. MILLER, *Reactive Power Control in Electric System*. John Wiley & Sons Ltd, Inc, New York, 1982.

[70] M. Baran and F. Wu, "Optimal sizing of capacitors placed on a radial distribution system," *IEEE Trans. Power Delivery*, vol. 4, no. 1, pp. 735–743, Jan. 1989.

[71] ——, "Optimal capacitor placement on radial distribution systems," *IEEE Trans. Power Delivery*, vol. 4, no. 1, pp. 725–734, Jan. 1989.

[72] C. Chen, C. Hsu, and Y. Yan, "Optimal distribution feeder capacitor placement considering mutual coupling effect of conductors," *IEEE Trans. Power Delivery*, vol. 10, no. 2, pp. 987–994, Apr. 1995.

[73] N. M. Neagle and D. R. Samson, "Loss reduction from capacitors installed on primary feeders," *AIEE Trans. Power Ap. Syst.*, vol. 75, no. 3, pp. 950–959, Jan. 1956.

[74] R. F. Cook, "Optimizing the application of shunt capacitors for reactive volt-ampere control and loss reduction," *AIEE Trans. Power Ap. Syst.*, vol. 80, no. 3, pp. 430–444, Aug. 1961.

[75] J. Grainger and S. Lee, "Optimum size and location of shunt capacitors for reduction of losses on distribution feeders," *IEEE Trans. Power Ap. Syst.*, vol. PAS-100, no. 3, pp. 1105–1118, Mar. 1981.

[76] J. J. Grainger, S. H. Lee, A. M. Byrd, and K. N. Clinard, "Proper placement of capacitors for losses reduction on distribution primary feeders," in *Proceedings of the American Power Conf.*, Dec. 2006, pp. 342–347.

[77] S. Lee and J. Grainger, "Optimum placement of fixed and switched capacitors on primary distribution feeders," *IEEE Trans. Power Ap. Syst.*, vol. PAS-100, no. 1, pp. 345 –352, Jan. 1981.

[78] J. Grainger and S. Lee, "Capacity release by shunt capacitor placement on distribution feeders: A new voltage-dependent model," *IEEE Trans. Power Ap. Syst.*, vol. PAS-101, no. 5, pp. 1236–1244, May 1982.

[79] J. J. Grainger, S. H. Lee, and A. A. El-Kib, "Design of a real-time switching control scheme for capacitive compensation of distribution feeders," *IEEE Trans. Power Ap. Syst.*, vol. PAS-101, no. 8, pp. 2420–2428, Aug. 1982.

[80] J. Grainger, S. Civanlar, and S. Lee, "Optimal design and control scheme for continuous capacitive compensation of distribution feeders," *IEEE Trans. Power Ap. Syst.*, vol. PAS-102, no. 10, pp. 3271–3278, Oct. 1983.

[81] J. Grainger, S. Civanlar, K. Clinard, and L. Gale, "Discrete-tap control scheme for capacitive compensation of distribution feeders," *IEEE Trans. Power Ap. Syst.*, vol. PAS-103, no. 8, pp. 2098–2107, Aug. 1984.

[82] ——, "Optimal voltage dependent continuous-time control of reactive power on primary feeders," *IEEE Trans. Power Ap. Syst.*, vol. PAS-103, no. 9, pp. 2714–2722, Sept. 1984.

[83] J. Grainger, A. El-Kib, and S. Lee, "Optimal capacitor placement on three-phase primary feeders: Load and feeder unbalance effects," *IEEE Trans. Power Ap. Syst.*, vol. PAS-102, no. 10, pp. 3296–3305, Oct. 1983.

[84] A. El-Kib, J. Grainger, K. Clinard, and L. Gale, "Placement of fixed and/or non-simultaneously switched capacitors on unbalanced three-phase feeders involving laterals," *IEEE Trans. Power Ap. Syst.*, vol. PAS-104, no. 11, pp. 3298 –3305, Nov. 1985.

[85] H. Dura, "Optimum number, location, and size of shunt capacitors in radial distribution feeders a dynamic programming approach," *IEEE Trans. Power Ap. Syst.*, vol. PAS-87, no. 9, pp. 1769–1774, Sept. 1968.

[86] M. Baran and F. Wu, "Optimal sizing of capacitors placed on a radial distribution system," *IEEE Trans. Power Delivery*, vol. 4, no. 1, pp. 735–743, Jan. 1989.

[87] S. Heier, *Grid Integration of Wind Energy Conversion Systems.* John Wiley & Sons Ltd, 1998.

[88] R. Fourer, D. M. Gay, and B. W. Kernighan, *AMPL : a modeling language for mathematical programming.* Thomson/Brooks/Cole, 2003.

[89] M. Shahidehpour, "Investing in expansion: the many issues that cloud transmission planning," *IEEE Power Energy Mag.*, vol. 2, no. 1, pp. 14–18, Jan. 2004.

[90] M. Shahidehpour and F. Schwarts, "Don't let the sun go down on pv [photovoltaic systems]," *IEEE Power Energy Mag.*, vol. 2, no. 3, pp. 40–48, May 2004.

[91] M. Urbina and Z. Li, "A fuzzy optimization approach to pv/battery scheduling with uncertainty in pv generation," in *38th North American Power Symposium (NAPS)*, Sept. 2006, pp. 561–566.

[92] S. Basu, L. Norum, and D. Dalal, "An improved pv battery charger for low cost low power stand alone low power systems," in *IEEE Int. Conf. Sust. Energy Technol.*, Nov. 2008, pp. 1157–1160.

[93] W.-F. Su, S.-J. Huang, and C.-E. Lin, "Economic analysis for demand-side hybrid photovoltaic and battery energy storage system," *IEEE Trans. Ind. Appl.*, vol. 37, no. 1, pp. 171–177, Jan. 2001.

[94] R. Hammond, J. Turpin, G. Corey, T. Hund, and S. Harrington, "Pv batteries and charge controllers: technical issues, costs, and market trends," in *Twenty-Sixth IEEE Photovoltaic Special. Conf.*, Sept. 1997, pp. 1165–1168.

[95] M. Becherif, D. Paire, and A. Miraoui, "Energy management of solar panel and battery system with passive control," in *Int. Conf. Clean Electr. Power*, May 2007, pp. 14–19.

[96] Ansoft, "Simulation system simplorer vhdl-ams tutorial," Ansoft Corporation, Tech. Rep., 2004.

[97] S. X. Chen, K. J. Tseng, and S. S. Choi, "Modeling of lithium-ion battery for energy storage system simulation," in *Power and Energy Engineer. Conf., Asia-Pacific*, Mar. 2009, pp. 1–4.

[98] B. Y. Liu and R. C. Jordan, "The interrelationship and characteristic distribution of direct, diffuse and total solar radiation," *Solar Energy*, vol. 4, no. 3, pp. 1–19, 1960.

[99] D. Erbs, S. Klein, and J. Duffie, "Estimation of the diffuse radiation fraction for hourly, daily and monthly-average global radiation," *Solar Energy*, vol. 28, no. 4, pp. 293–302, 1982.

[100] R. Perez, R. Seals, P. Ineichen, R. Stewart, and D. Menicucci, "A new simplified version of the perez diffuse irradiance model for tilted surfaces," *Solar Energy*, vol. 39, no. 3, pp. 221–231, 1987.

[101] P. Kirawanich and R. O'Connell, "Potential harmonic iumpact of microturbines on a commercial power distribution system," in *Power Eng. Soc. General Meeting*, vol. 2, Jul. 2003.

[102] A. Fanney and B. Dougherty, "Building integrated photovoltaic test facility," *ASME Trans. Solar Eng.*, vol. 123, no. 3, pp. 194–199, 2001.

[103] R. Sioshansi, R. O'Neill, and S. Oren, "Economic consequences of alternative solution methods for centralized unit commitment in day-ahead electricity markets," *IEEE Trans. Power Syst.*, vol. 23, no. 2, pp. 344 –352, May 2008.

[104] B. Venkatesh, P. Yu, H. Gooi, and D. Choling, "Fuzzy milp unit commitment incorporating wind generators," *IEEE Trans. Power Syst.*, vol. 23, no. 4, pp. 1738–1746, Nov. 2008.

[105] Y. Fu, M. Shahidehpour, and Z. Li, "Security-constrained unit commitment with ac constraints," *IEEE Trans. Power Syst.*, vol. 20, no. 2, pp. 1001 – 1013, May 2005.

[106] H. Ma and S. Shahidehpour, "Unit commitment with transmission security and voltage constraints," *IEEE Trans. Power Syst.*, vol. 14, no. 2, pp. 757 –764, May 1999.

[107] A. M. Geoffrion, "Generalized benders decomposition," *Journal of Optimization Theory and Applications*, vol. 10, pp. 237–260, 1972.

[108] (1962) Benders decomposition. [Online]. Available: http://is.gd/e26f3

[109] N. Sahinidis and I. Grossmann, "Convergence properties of generalized benders decomposition," *Computers & Chemical Engineering*, vol. 15, no. 7, pp. 481–491, 1991.

[110] B. Borowy and Z. Salameh, "Optimum photovoltaic array size for a hybrid wind/pv system," *IEEE Trans. Energy Convers.*, vol. 9, no. 3, pp. 482–488, Sep. 1994.

[111] S. Zhang, K. J. Tseng, D. Vilathgamuwa, T. Nguyen, and X. Y. Wang, "Design of a robust grid interface system for pmsg-based wind turbine generators," *IEEE Trans. Ind. Electron.*, vol. 58, no. 1, pp. 316–328, Jan. 2011.

[112] A. Giustiniani, G. Petrone, G. Spagnuolo, and M. Vitelli, "Low-frequency current oscillations and maximum power point tracking in grid-connected fuel-cell-based systems," *IEEE Trans. Ind. Electron.*, vol. 57, no. 6, pp. 2042–2053, Jun. 2010.

[113] R. Kadri, J. Gaubert, and G. Champenois, "An improved maximum power point tracking for photovoltaic grid-connected inverter based on voltage-oriented control," *IEEE Trans. Ind. Electron.*, vol. 58, no. 1, pp. 66–75, Jan. 2011.

[114] M. Charkhgard and M. Farrokhi, "State-of-charge estimation for lithium-ion batteries using neural networks and ekf," *IEEE Trans. Ind. Electron.*, vol. 57, no. 12, pp. 4178–4187, Dec. 2010.

[115] H. Dommel and W. Tinney, "Optimal power flow solutions," *IEEE Trans. Power App. Syst.*, vol. PAS-87, no. 10, pp. 1866–1876, Oct. 1968.

[116] (2010, Mar.) Active and reactive load. [Online]. Available: http://is.gd/b6y4l

[117] H. Wei, H. Sasaki, J. Kubokawa, and R. Yokoyama, "An interior point nonlinear programming for optimal power flow problems with a novel data structure," *IEEE Trans. Power Syst.*, vol. 13, no. 3, pp. 870–877, Aug. 1998.

[118] (2010, Jun.) 112-bus power system. [Online]. Available: http://is.gd/dQdgH

[119] (2008, Dec.) Northeast power coordinating council (npcc) operating reserve criteria. A-06.pdf. [Online]. Available: http://is.gd/b6xbb

[120] H. T. Le and T. Q. Nguyen, "Sizing energy storage systems for wind power firming: An analytical approach and a cost-benefit analysis," in *Power & Energy Soc. General Meeting*, 20-24 2008.

[121] S. Chen and H. Gooi, "Scheduling of energy storage in a grid-connected pv/battery system via simplorer," in *TENCON IEEE Region 10 Conf.*, Nov. 2009, pp. 1–5.

[122] X. Wang, D. Mahinda Vilathgamuwa, and S. Choi, "Determination of battery storage capacity in energy buffer for wind farm," *IEEE Trans. Energy Convers.*, vol. 23, no. 3, pp. 868–878, Sept. 2008.

[123] C. Venu, Y. Riffonneau, S. Bacha, and Y. Baghzouz, "Battery storage system sizing in distribution feeders with distributed photovoltaic systems," in *2009 IEEE Bucharest, PowerTech*, Jul. 2009, pp. 1–5.

[124] J. Mitra, "Reliability-based sizing of backup storage," *IEEE Trans. Power Syst.*, vol. 25, no. 2, pp. 1198–1199, 2010.

[125] T.-Y. Lee and N. Chen, "Determination of optimal contract capacities and optimal sizes of battery energy storage systems for time-of-use rates industrial customers," *IEEE Trans. Energy Convers.*, vol. 10, no. 3, pp. 562–568, Sept. 1995.

[126] H. T. Le and T. Q. Nguyen, "Sizing energy storage systems for wind power firming: An analytical approach and a cost-benefit analysis," in *Power & Energy Soc. General Meeting*, Jul. 2008, pp. 1–8.

[127] J. Kaldellis, D. Zafirakis, and E. Kondili, "Optimum sizing of photovoltaic-energy storage systems for autonomous small islands," *Int. J. Electr. Power Energ. Syst.*, vol. 32, no. 1, pp. 24–36, 2010.

[128] Y. Chen, P. Luh, C. Guan, Y. Zhao, L. Michel, M. Coolbeth, P. Friedland, and S. Rourke, "Short-term load forecasting: Similar day-based wavelet neural networks," *IEEE Trans. Power Syst.*, vol. 25, no. 1, pp. 322 –330, Feb. 2010.

[129] (2010, Jul.) Battery and electric vehicle report. [Online]. Available: http://bit.ly/fGaZPB

[130] (2009, Aug.) Ubi-2590 smbus (part no. ubbl10) battery specification. [Online]. Available: http://bit.ly/gLgVY0

[131] T. E. Lipman, R. Ramos, and M. Kammen, "An assessment of battery and hydrogen energy storage systems integrated with wind energy resources in california," California Energy Commission Public Interest Energy Research (PIER) Program, Tech. Rep., 2005.

[132] S. X. Chen and H. B. Gooi, "Jump and shift method for multi-objective optimization," *IEEE Trans. Ind. Electron.*, vol. 58, no. 10, pp. 4538–4548, Oct. 2011.

[133] S. Teleke, M. Baran, S. Bhattacharya, and A. Huang, "Optimal control of battery energy storage for wind farm dispatching," *IEEE Trans. Energy Convers.*, vol. 25, no. 3, pp. 787–794, Sept. 2010.

[134] X. Tang, X. Mao, J. Lin, and B. Koch, "Li-ion battery parameter estimation for state of charge," in *American Control Conf.*, Jul. 2011, pp. 941–946.

[135] T. R. Crompton, *Battery reference book*. Oxford: Newnes, 2000.

[136] X. Tang, X. Mao, J. Lin, and B. Koch, "Li-ion battery parameter estimation for state of charge," in *American Control Conf.*, Jul. 2011, pp. 941–946.

[137] A. Anbuky and P. Pascoe, "Vrla battery state-of-charge estimation in telecommunication power systems," *IEEE Trans. Ind. Electron.*, vol. 47, no. 3, pp. 565–573, Jun. 2000.

[138] K. Kutluay, Y. Cadirci, Y. Ozkazanc, and I. Cadirci, "A new online state-of-charge estimation and monitoring system for sealed lead-acid batteries in telecommunication power supplies," *IEEE Trans. Ind. Electron.*, vol. 52, no. 5, pp. 1315–1327, Oct. 2005.

[139] G. L. Plett, "Extended kalman filtering for battery management systems of lipb-based hev battery packs: Part 2. modeling and identification," *J. Power Sources*, vol. 134, no. 2, pp. 262–276, 2004.

[140] P. S. Maybeck, *Stochastic models, estimation and control*. New York : Academic Press, 1982.

[141] K. Myers and B. Tapley, "Adaptive sequential estimation with unknown noise statistics," *IEEE Trans. Automat. Contr.*, vol. 21, no. 4, pp. 520–523, Aug. 1976.

[142] (2011, Aug.) Ni 9225 - national instruments. [Online]. Available: http://bit.ly/rd4bcv

[143] D. Andrea, "State of charge estimate with li-ion batteries," http://bit.ly/nE34wB, Oct. 2009.

[144] H. Dai, X. Wei, and Z. Sun, "Online soc estimation of high-power lithium-ion batteries used on hevs," in *ICVES 2006*, Dec. 2006, pp. 342–347.

[145] (2009, Aug.) Ubi-2590 battery charger specification. [Online]. Available: http://bit.ly/qgxzcS

[146] H. Zhiwei, G. Mingyu, and X. Jie, "Ekf-ah based state of charge online estimation for lithium-ion power battery," in *International Computational Intelligence and Security Conf.*, vol. 1, 2009, pp. 142–145.

[147] H. Hongwen, X. Rui, Z. Xiaowei, S. Fengchun, and F. JinXin, "State-of-charge estimation of the lithium-ion battery using an adaptive extended kalman filter based on an improved thevenin model," *IEEE Trans. Veh. Tech.*, vol. 60, no. 4, pp. 1461–1469, 2011.

[148] S. X. Chen, "Modeling of lithium-ion battery for energy storage system simulation," Nanyang Technological University, Tech. Rep., 2008.

[149] L. Y. C. Amarasinghe and U. D. Annakkage, "Analysis of market signals in a competitive electricity market using components of network rental," *Elect. Power Syst. Res.*, vol. 79, no. 4, pp. 635–644, 2009.

[150] H. Song, B. Lee, S.-H. Kwon, and V. Ajjarapu, "Reactive reserve-based contingency constrained optimal power flow (rccopf) for enhancement of voltage stability margins," *IEEE Trans. Power Syst.*, vol. 18, no. 4, pp. 1538 – 1546, Nov. 2003.

VITA

Chen Shuaixun was born in 1984 in P. R. China. He received his B.S. dual degree in Power Engineering and Business Administration from Wuhan University, China, in 2007 and M.Sc. degree in Power Engineering from Nanyang Technological University, Singapore, in 2008. Currently he is a Research Associate of Energy Research Institute at Nanyang Technological University (ERI@N), Singapore. His research interests are Smart Energy Management Systems, Energy Efficiency, Renewable Energy Sources and Energy Storage Systems.

This research work has led to the following publications.

i. Journal Papers

[1] **S. X. Chen** and H. B. Gooi, "Jump and Shift Method for Multi-Objective Optimization," *IEEE Transactions on Industrial Electronics*, vol.58, no.10, pp.4538-4548, Oct. 2011.

[2] **S. X. Chen**, H. B. Gooi and M. Q. Wang, "Sizing of Energy Storage for Microgrids," *IEEE Transactions on Smart Grid*, vol. 3, no.1, pp.142-151, Mar. 2012.

[3] W. Q. Wang, H. B. Gooi and **S. X. Chen**, "Optimizing Probabilistic Spinning Reserve Using an Analytical EENS," *IET Generation, Transmission & Distribution*, vol.5, no.7, pp.772-780, Jul. 2011.

[4] **S. X. Chen**, H. B. Gooi and N. Xia, "Modelling of Lithium-ion Battery for Online Energy Management Systems," Accepted by *IET Electrical Systems in Transportation*, 2012.

[5] N. Xia, H. B. Gooi and **S. X. Chen**, "Improved Equality-Constrained State Estimation with Synchrophasor Measurements," Under Review in *IET on generation transmission & distribution*, 2012.

[6] **S. X. Chen**, H. B. Gooi and M. Q. Wang, "Solar radiation forecast based on fuzzy logic and neural networks," Submitted to *IET on Renewable Power Generation*, 2012.

[7] W. Q. Wang, H. B. Gooi and **S. X. Chen**, "A Tradeoff between Unit Capacity and Production Cost in Spinning Reserve Optimization," Under Review in *IET on generation transmission & distribution*, 2012.

ii. Conference Papers

[8] **S. X. Chen**, K. J. Tseng and S. S. Choi, "Modeling of Lithium-Ion Battery for Energy Storage System Simulation," *Asia-Pacific Power and Energy Engineering Conference*, Mar. 2009.

[9] **S. X. Chen** and H. B. Gooi, "Scheduling of Energy Storage in a Grid-Connected PV/Battery System via SIMPLORER," *IEEE TENCON 2009 Conference, Singapore*, Nov. 2009.

[10] **S. X. Chen** and H. B. Gooi, "Capacitor Planning of Power Systems with Wind Generators and PV Arrays," *IEEE TENCON 2009 Conference, Singapore*, Nov. 2009.

[11] **S. X. Chen** and H. B. Gooi, "Sizing of energy storage system for microgrids," *Probabilistic Methods Applied to Power Systems (PMAPS), 2010 IEEE 11th International Conference*, Jun. 2010.

[12] X. Feng, H. B. Gooi and **S. X. Chen**, "An Improved Lithium-ion Battery Model with Temperature Prediction Considering Entropy," Accepted by *IEEE PES ISGT*, 2012.

[13] **S. X. Chen**, H. B. Gooi, T. W. Tham, T. H. Yushein, and K. Watanabe, "Investigation on Solar PV and Battery System Penetration in Singapore Distribution Power Networks," Accepted by *International Power and Energy Conference*, 2012.